

Graphene Synthesis under Si-CMOS Compatible Conditions

Von der Fakultät 1 - MINT - Mathematik, Informatik, Physik,

Elektro- und Informationstechnik

der Brandenburgischen Technischen Universität Cottbus–Senftenberg

genehmigte Dissertation

zur Erlangung des akademischen Grades eines

Dr.rer.nat.

vorgelegt von

Fatima Akhtar

geboren am 25.12.1984 in Bahawalnagar, Pakistan

Vorsitzende/r: Prof. Götz Seibold

Gutachter/in: Prof. Dr. Christian Wenger

Gutachter/in: Prof. Dr. Jan Ingo Flege

Gutachter/in: Prof. Dr. Max Lemme

Tag der mündlichen Prüfung: 25.04.2022

In the name of Allah, the most beneficent, the most merciful

ACKNOWLEDGMENTS

During the course of my PhD research study, a lot of people have helped me. Now, it is time to express my sincere feelings for their support.

Firstly, I want to thank Prof. Dr. Christian Wenger, our department head; his encouragement, guidance, and kindness will always be an honor for me.

I would like to pay my sincere gratitude to Dr. Mindaugas Lukosius, my supervisor, for providing me the opportunity to work in his group, for his stalwart supervision, continuous encouragement, and endless patience during all these years. Thanks for showing me different ways to approach a research problem and the need to be persistent in accomplishing any goal. Thanks for always being there whenever I need your help, and thanks for believing in me that made me believe in myself.

Special thanks go to Dr. Jarek Dabrowski for atomistic ab-initio calculations and sharing his scientific knowledge; to Dr. Peter Zaumseil for performing XRD experiments; to Dr. Ioan Costina for useful help in XPS measurements; to Dr. Oksana Fursenko for ellipsometry measurements and for helping me to solve any tip-related problems of AFM; to David Stolarek and Hans Michael Krause for performing SEM measurements; to Hans Thieme who helped me handling the CVD and XPS tools; to Yvonne Mausolf for assisting me with organizational issues; to Dr. Martin Albrect (IKZ, Berlin) for EBSD measurements; to Dr. Alex Jouvray for performing the graphene growth experiments on structured Ni wafers at Aixtron Ltd., England.

I am very much thankful to Dr. Gunther Lippert, Dr. Rasuole Lukose, and Dr. Viktoria Diana Schylkow for their kindness, care, support, and help.

I also gratefully acknowledge the Gauss Centre for Supercomputing e.V. (www.gauss-centre.eu) for funding part of this PhD work (graphene/Ge) by providing computing time through the John von Neumann Institute for Computing (NIC) on the GCS Supercomputer JUWELS at Jülich Supercomputing Centre (JSC).

My deepest gratitude is to my entire family for their love and support, especially my sisters Sadia, Fozia, Saira, Amna, Naila, Faiza, brother Mirza Umer, and my dear Abu Mirza Akhtar Ali, and my beloved Ami Jameela Begum (late).

Last but not least, most special thanks to my husband, Naeem Gulzar, for his support and understanding throughout my PhD research. I appreciate my beloved daughter Maryam Naeem who has provided me all the joy of life with her innocent acts and refreshing me with lovely smiles.

ABSTRACT

Due to the unique electronic band structure, graphene has opened the great potential to extend the functionality of a large variety of graphene-based devices in health and environment, energy storage, or various microelectronic applications, to mention a few. At this point, the implementation of graphene into Silicon (Si) semiconductor technology is strongly dependent on several key challenges. Among them, high-quality and wafer-scale graphene synthesis on CMOS-compatible substrates is of the highest importance. Though large-area graphene can be achieved on substrates like copper, platinum, silicon carbide, or single-crystal Ni, however, high growth temperatures, unavailability of large scale, or contamination issues are the main drawbacks of their usage. In this PhD work, 8-inch scale graphene synthesis is attempted on alternative substrates such as epitaxial Germanium on Si and polycrystalline Nickel on Si. To achieve the growth of the highest quality of graphene, this work focuses on the investigations of various nucleation and growth mechanisms, substrate–graphene interfaces, effects of different substrate orientations, and detailed microscopic and macroscopic characterization of the grown films. Finally, it should also be stressed that the experiments in this work were carried out in a standard BiCMOS pilot line, making this study unique, as its results might directly pave the way to further graphene integration and graphene-based device prototyping in mainstream Si technologies.

Durch seine einzigartige Bandstruktur hat Graphen ein großes Feld zur Erweiterung der Funktionalität graphenbasierter Bauelemente im Gesundheitswesens und der Umwelttechnologie, zur Speicherung von Energie, für neue Verbundstoffe und für mikroelektronischen Anwendungen, um nur Einige zu nennen, eröffnet.

Gerade der Einsatz von Graphen in der siliziumbasierten Halbleitertechnologie hängt stark von einigen wesentlichen Voraussetzungen ab. Darunter ist die hohe Qualität der Abscheidung von Graphen auf CMOS-kompatiblen Substraten von größter Wichtigkeit und bisher noch nicht gelöst.

Obwohl hochqualitatives Graphen auf Substraten wie Kupfer, Platin, Siliziumcarbid oder einkristallinem Nickel hergestellt werden kann, sind hohe Wachstumstemperaturen, großflächige Beschichtung oder Kontaminationen Hinderungsgründe für deren Einsatz.

In der Promotionsarbeit wird die Graphenabscheidung auf alternative 200mm Substrate, wie einkristallinem Germanium auf Silizium und polykristallines Nickel auf Silizium untersucht. Um die beste Wachstumsqualität von Graphen zu erreichen, ist der Fokus dieser Arbeit auf verschiedene Nukleations- und Wachstumsmechanismen, auf Graphen-Substrat wechselwirkungen, Effekte verschiedener Substratorientierung sowie detaillierter mikroskopischer und makroskopischer Charakterisierung der gewachsenen Schicht gerichtet. Abschließend sollte erwähnt werden, dass diese Experimente in einer Standardpilotlinie (BiCMOS) durchgeführt wurden, um mit den Ergebnissen dieser Arbeit den Weg zur Graphenintegration und zu graphenbasierten prototypischen Bauelementen in die industrielle Silizium-technologie zu ebnen.

TABLE OF CONTENTS

ACKNOWLEDGMENTS	1
ABSTRACT	3
LIST OF ABBREVIATIONS	8
CHAPTER 1	11
1. MOTIVATION AND OBJECTIVES	11
1.1. Motivation	11
1.2. Research objectives	13
1.3. Thesis Organization	14
CHAPTER 2	16
2. GRAPHENE OVERVIEW.....	16
2.1. Carbon and its allotropes	16
2.2. Atomic structure of graphene	18
2.3. Properties and potential applications of graphene.....	20
2.4. Synthesis of graphene	21
2.5. Chemical vapor deposition	22
Pressure	23
Carbon source.....	23
Substrate.....	24
2.6. Graphene growth on dielectrics	24
2.7. Graphene growth on copper	26
Graphene growth mechanism on copper.....	27
Crystal structure of copper.....	27
Problematics.....	28
2.8. Graphene growth on nickel	29
Graphene growth mechanism on nickel.....	30
Crystal structure of nickel.....	30
Problematics.....	31
2.9. Graphene growth on germanium	33
Graphene growth mechanism on germanium	34
Crystal structure of germanium.....	35
Problematics.....	38

CHAPTER 3	41
3. EXPERIMENTAL SETUP AND CHARACTERIZATION TECHNIQUES	41
3.1. Basics of chemical vapor deposition	41
3.2. Raman spectroscopy.....	44
The Raman effect.....	45
Raman spectrum of graphene	47
3.3. X-ray photoelectron spectroscopy	49
3.4. Atomic force microscopy	51
3.5. Scanning electron microscopy.....	52
3.6. X-ray diffraction.....	53
3.7. Optical microscopy	54
3.8. Electron backscattering diffraction	55
3.9. Reactive ion etching	56
3.10. Spectral ellipsometry.....	57
3.11. Time-of-flight secondary ion mass spectrometry.....	58
3.12. Electrical measurements	59
Hall effect.....	59
Current-Voltage measurements (I-V).....	61
CHAPTER 4	64
4. RESULTS & DISCUSSIONS	64
4.1. Chemical vapor deposition of graphene on polycrystalline nickel.....	65
Deposition of the Ni films for graphene growth	65
Selection of a thermally stable thickness of the Ni films	66
Surface pretreatments of 200nm Ni films.....	67
Influence of pretreatment conditions on the crystallinity and morphology of Ni films	68
Influence of pretreatment conditions on Ni surface cleaning	76
Graphene growth	77
Influence of graphene growth on grain growth in Ni film.....	79
Characterization of graphene by SEM and Raman spectroscopy	80
Summary.....	83
4.1.1. Ni-mediated growth of graphene on silicon dioxide.....	84
Preparations of Ni structures for graphene synthesis.....	84
4.1.1.1. Substrates preparations for graphene growth between Ni bars (STRUCTURES_A)..	84
Graphene synthesis	86
4.1.1.2. Growth of graphene underneath Ni (STRUCTURES_B)	89

Characterization of graphene.....	90
Summary.....	92
4.2. Growth of graphene on 200mm Ge(001)/Si(001)	94
Substrates preparations for the growth of graphene	94
Optimization of Ge thickness for graphene growth	94
Graphene growth on Ge(001)	95
Characterization of graphene.....	95
Summary.....	102
4.3. Growth of graphene on 200mm Ge(110)/Si(110)	103
Substrates preparations for the growth of graphene	103
Graphene growth on Ge(110)	103
Characterization of graphene.....	104
Summary.....	108
4.4. Oxidation behavior of graphene/Ge(001) versus graphene/Ge(110)	110
Influence of atmospheric oxygen on the properties of graphene/Ge Systems	110
Reversibility of graphene/germanium systems.....	118
Discussion	121
Summary.....	125
CHAPTER 5	128
5. CONCLUSIONS & OUTLOOK	128
5.1. Conclusions.....	128
5.2. Perspectives.....	130
SCIENTIFIC VISIBILITY	132
Publications in Peer-reviewed Journals.....	132
Presentations at conferences	132
LITERATURE.....	134

LIST OF ABBREVIATIONS

CMOS	Complementary Metal-Oxide-Semiconductor
CVD	Chemical Vapor Deposition
PECVD	Plasma Enhanced Chemical Vapor Deposition
APCVD	Atmospheric Pressure Chemical Vapor Deposition
MOCVD	Metallo Organic Chemical Vapor Deposition
DFT	Density Functional Theory
HOPG	Highly Ordered Pyrolytic Graphite
PVD	Physical Vapor Deposition
MBE	Molecular Beam Epitaxy
Ni	Nickel
Cu	Copper
Si	Silicon
Ge	Germanium
FCC	Face Centered Cubic
TEM	Transmission Electron Microscopy
EBSD	Electron Backscattering Diffraction
STM	Scanning Tunneling Microscopy
LEED	Low Energy Electron Diffraction
XPS	X-ray Photoelectron Spectroscopy
ESCA	Electron Spectroscopy for Chemical Analysis
XRD	X-ray Diffraction
SEM	Scanning Electron Microscopy

OM	Optical Microscopy
AFM	Atomic Force Microscopy
RIE	Reactive Ion Etching
ToF-SIMS	Time-of-Flight Secondary Ion Mass Spectrometry
FWHM	Full Width at Half maxima
GB	Grain Boundary
LEEM	Low Energy Electron Diffraction
ARPES	Angle-Resolved Photoemission Spectroscopy
TLM	Transmission Line Method

PART I

INTRODUCTION

CHAPTER 1

1. MOTIVATION AND OBJECTIVES

1.1. Motivation

For many years, graphene was thought to be thermodynamically unstable and unable to exist in nature [1]. Hence, it was deemed an academic material where its honeycomb structure was used as a theoretical model for describing the properties of various carbon allotropes such as fullerenes, nanotubes, and graphite. Graphene was finally transferred from an academic to an essential material when it was experimentally verified in 2004 [2] – a discovery awarded the Noble prize in 2010. This verification was remarkable for its demonstration of graphene's record-breaking conductivity [2]. In addition, graphene also exhibits high Fermi velocity and high carrier mobility. It can conduct heat and electricity better than metals, but it is transparent and flexible like plastic. Besides, graphene is chemically inert and stable. All these extraordinary characteristics have inspired influential applications in different areas, including photonics, composite materials, graphene inks, medical, and microelectronics, to name a few [3–9].

The fabrication of graphene-based composite materials or inks may need different requirements compared to graphene's integration into microelectronic applications that face a couple of challenges. Among them, one of the most fundamental challenges is the need for growth methods that can produce high-quality graphene while maintaining its outstanding properties. The term 'high-quality' means that the graphene film should contain as low as possible wrinkles, impurities, voids, holes, grain boundaries, etc. [10]. Additionally, the graphene film needs to be uniformly monolayer over large areas.

From the perspective of device fabrication, ideally, graphene should be grown on dielectrics. Up to date, the growth of large-area and high-quality graphene is not achieved on dielectrics. Therefore, graphene is typically grown on substrates like Copper (Cu), Silicon carbide (SiC), and single-crystal substrates such as Ni(111), Cu(111), Pt(111), etc. The issues related to Cu contaminations, high costs of single crystal and SiC substrates, and high graphene growth temperature make these substrates CMOS (complementary metal-oxide-semiconductor) incompatible. At this point, the growth of graphene on a CMOS-compatible substrate could be a possible way for its direct integration into Si microelectronics. Therefore, in this PhD work, polycrystalline Nickel (Ni) on Si and epitaxial Germanium (Ge) on Si were used as alternative substrates for the growth of graphene because of their (i) catalytic activity, (ii) large-scale availability on Si wafers, and (iii) CMOS compatibility. Indeed, large-area graphene can be grown on Ni; however, the inhomogeneous surface of polycrystalline Ni makes graphene growth a complicated process. Grain boundaries (GBs) in polycrystalline Ni serve as the most preferential sites for the growth of multilayer graphene, whereas the smooth surface of Ni(111) grains favors the growth of monolayer graphene. One way to control the thickness uniformity of graphene is to reduce the number of grain boundaries. Therefore, it is crucial to prepare the surface of polycrystalline Ni so that the number of grain boundaries can be reduced or the sizes of Ni(111) grains can be increased. It could be achieved by high temperature annealing of the Ni films where the size and orientations of Ni(111) are modified. Therefore, to influence the graphene growth, 200nm thin Ni films were pretreated, in this PhD work, at high temperatures under different conditions to control their surfaces by modifying Ni grain sizes, orientations, and GBs. In comparison to Ni, the growth of graphene on Ge was a new topic at the beginning of this PhD work as only a few literature reports were available. Therefore, parts of problematics

related to the graphene/Ge system were discovered during this thesis work. For the graphene/Ge system, it is crucial to understand how different crystallographic Ge orientations impact the graphene's growth and properties, and how the graphene growth process influences the surface morphology of the underlying Ge orientation. Another critical issue is related to the oxidation of the Ge underneath the grown graphene layers. The presence of oxygen can have a negative impact on graphene properties; hence, a precise understanding of the graphene/Ge interface is, therefore, of importance. The investigations of graphene/Ge systems in this PhD study were supported by DFT calculations in order to understand the possible graphene growth mechanisms, faceted and non-faceted surfaces, and oxidation of Ge underneath the grown graphene layers. Another important aspect and one of the main motivations of this work was to explore the possibility of growing graphene on 8-inch wafers. Indeed, graphene was grown on 8-inch wafers in this PhD study, which could be an important step towards further optimization of graphene/substrate systems and for graphene-based prototyping in the mainstream Si technologies.

1.2. Research objectives

The objectives of this thesis may be stated as follows:

Objective 1: To investigate and pretreat the surfaces of thin (200nm) polycrystalline Ni films under different annealing conditions at higher temperatures in order to control graphene growth by modifying Ni grain sizes, orientations, and GBs.

Objective 2: To explore the potential of the Ni-mediated synthesis method for obtaining graphene directly on the surface of silicon dioxide and determine the impacts of

different Ni structures as well as different growth parameters on graphene's growth and properties.

Objective 3: To explore the possibility of graphene growth over 8-inch sized (001) and (110) oriented Ge substrates and to explain the surface morphologies of the Ge films underneath the grown graphene supported by ab initio density functional theory (DFT) calculations.

Objective 4: To investigate and discover the mechanism behind the oxidation behavior of graphene-covered Ge(001) and Ge(110) and determine the impacts of this interfacial oxygen on graphene properties.

1.3. Thesis Organization

This thesis is organized into five chapters, as follows:

Chapter 1 describes the motivation of this thesis work. Also, it provides the objectives and outline.

Chapter 2 begins with a short introduction to carbon and its allotropes. Then, the basics of graphene, including its structure, properties, and potential application, are briefly discussed. The synthesis of graphene on various substrates is also reviewed.

Chapter 3 provides the details of the synthesis and characterization methods. To be more precise, chemical vapor deposition, Raman spectroscopy, X-ray photoelectron spectroscopy, scanning electron microscopy, atomic force microscopy, X-ray diffraction, optical microscopy, electron backscattered diffraction, spectral ellipsometry, time-of-flight

secondary ion mass spectrometry, reactive ion etching, and electrical measurements are briefly introduced.

Chapter 4 presents the main results of the thesis and is divided into four sections.

Section 4.1 discusses the Ni-assisted CVD of graphene, where the effects of different annealing conditions on the surface morphology of Ni are discussed and compared. The derived conclusions are used to address how different annealing conditions affect graphene formation. After that, the results obtained for Ni-assisted graphene growth on silicon dioxide are presented (subsection 4.1.1). In sections 4.2 and 4.3 of the chapter, the growth of graphene on (001) and (110) oriented Ge is discussed, respectively. The last part (4.4) of this chapter is focused on the investigation of the oxidation behavior of graphene/Ge(001) and (110) systems.

This thesis will be concluded in **Chapter 5** by summarizing the results and findings.

CHAPTER 2

2. GRAPHENE OVERVIEW

Despite that the extraordinary properties of graphene have been reported since its first isolation, a short introduction to graphene's band structure, properties, and potential applications is given at the beginning of this chapter, followed by the synthesis of graphene on various substrates.

2.1. Carbon and its allotropes

Carbon is the fourth most abundant element in the solar system after hydrogen, helium, and oxygen; its ratio in the earth's crust is about 180ppm [11]. Carbon exists in various allotropic forms. One type is crystalline, which includes graphite, diamond, fullerenes, and graphene, while the other is amorphous carbon. In order to know the arrangement of carbon atoms in different allotropes, the understanding of the atomic configuration of carbon is crucial. The atomic number of carbon is six in the ground state; two electrons occupy the $1s^2$ orbital, while the remaining four fill the $2s^2$, $2p_x^1$, and $2p_y^1$ as illustrated in Fig. 2.1a. As seen, carbon is divalent in the ground state; however, carbon allotropes are tetravalent. In order to justify the tetravalence of carbon, one of the electrons from the $2s$ orbital must fill an empty $2p$ orbital (Fig. 2.1b). The linear combination of s and p orbitals generates new orbitals called hybrid, and this process is known as hybridization. The hybridization of one s and three p orbitals leads to the formation of four ***sp³ hybrid orbitals*** (Fig. 2.1c). ***sp³ hybridization*** occurs in diamond and lonsdaleite.

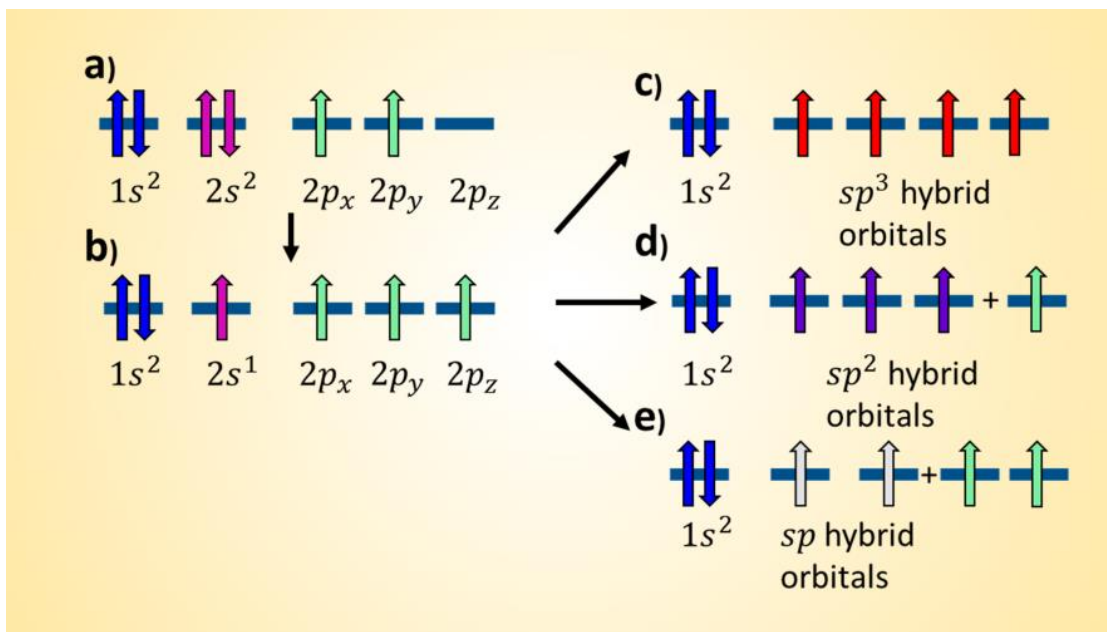


Fig. 2.1. (a–b) Schematic illustration of electronic distribution of electrons in the ground and excited state of carbon atom (c–e) sp^3 , sp^2 , and sp hybridization of carbon.

On the other hand, **sp^2 hybridization** involves the mixing of one s and two p orbitals (Fig. 2.1d). **sp^2 hybridization** leads to the formation of a graphite structure. **sp hybridization** occurs by the combination of one s and one p orbital, as shown in Fig. 2.1e. This type of hybridization occurs in Fullerenes.

Among all carbon allotropes, it is sp^2 hybridized graphene, which has attracted numerous interests because of its novel properties and unique structure. Graphene is a one-atom-thick layer of carbon atoms that are arranged in a honeycomb lattice. It is the building block of graphite, carbon nanotube, and fullerenes. Graphene exists in various forms such as graphene oxide, graphene nanoplatelets, graphene nanoribbons, reduced graphene oxide, graphene quantum dots, and a single sheet of carbon atoms. Thus, before going into further details, I would like to clarify that, in this thesis work, the term graphene is used to describe a single-layer graphene film. The atomic structure of graphene will be discussed in the next section.

2.2. Atomic structure of graphene

The unit cell of graphene contains two carbon atoms represented by A and B, as shown in

Fig. 2.2a. The two lattice unit vectors a_1 and a_2 are written as [12–14]:

$$a_1 = \frac{a}{2}(3, \sqrt{3}), \quad a_2 = \frac{a}{2}(3, -\sqrt{3}) \quad 2.1$$

where $a = 1.42\text{\AA}$ is the C–C bond distance. The corresponding reciprocal lattice vectors (b_1, b_2) can be written as:

$$b_1 = \frac{2\pi}{3a}(1, \sqrt{3}), \quad b_2 = \frac{2\pi}{3a}(1, -\sqrt{3}) \quad 2.2$$

Fig. 2.2b shows the reciprocal lattice vectors together with the first Brillouin zone. The first Brillouin zone contains several unique points: the Γ point is the center of the Brillouin zone, M is the center of the edge, while the corners of the Brillouin zone are known as Dirac points. Three of the Dirac points are labeled as K, corresponding to one triangular sub-lattice in reciprocal space. The remaining three points are labeled as K' , corresponding to the second sub-lattice. The electronic band structure of graphene in Fig. 2.3a illustrates that conduction and valance bands meet at the Dirac points but do not overlap at these points. Due to this, graphene is called a semimetal or a zero-gap semiconductor. The energy dispersion close to the Dirac point is linear with momentum and is described by [15,16]:

$$E = \pm\hbar v_F k \quad 2.3$$

where v_F and k represent the Fermi velocity and the wave vector, respectively.

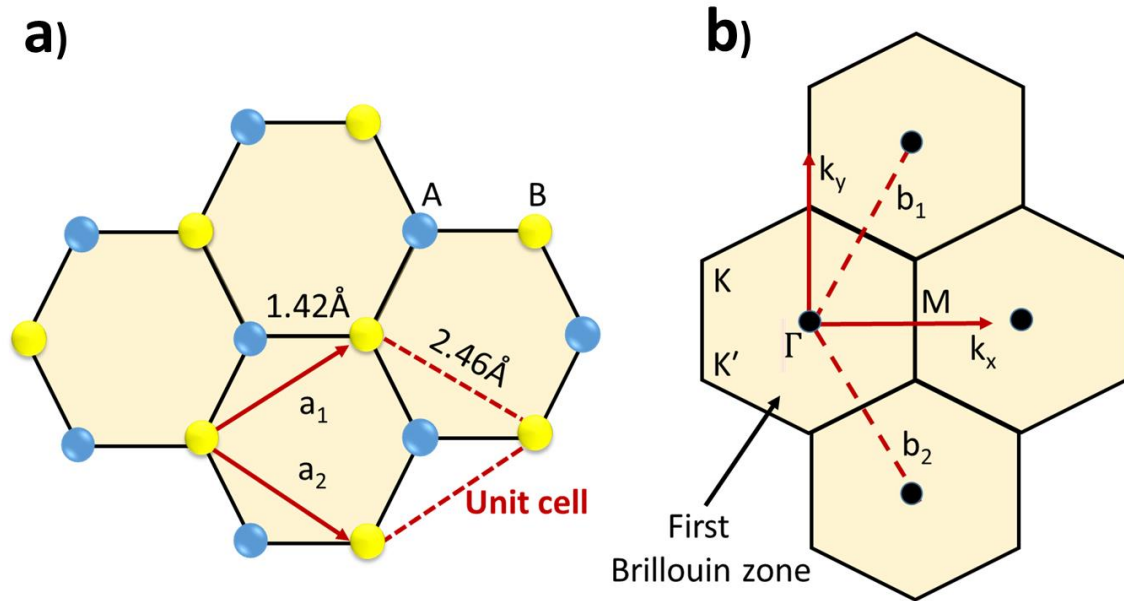


Fig. 2.2. (a) Honeycomb graphene lattice containing two atoms (A and B) per unit cell. The lattice vectors are represented by a_1 and a_2 . (b) Honeycomb lattice of graphene in the reciprocal space, b_1 and b_2 denote the reciprocal lattice vectors. The center of the Brillouin zone, the Dirac points, and the middle edge of the Brillouin zone are represented by Γ , K(K'), and M, respectively.

The charge carriers in graphene near the Dirac points behave as massless particles with a speed of $\sim 1 \times 10^6 \text{ m/s}$. These charge carriers are described by the Dirac equation and therefore are known as Dirac Fermions. Besides, the density of states at the Dirac point is zero and increases linearly with respect to energy allowing for carrier modulations (Fig. 2.3b).

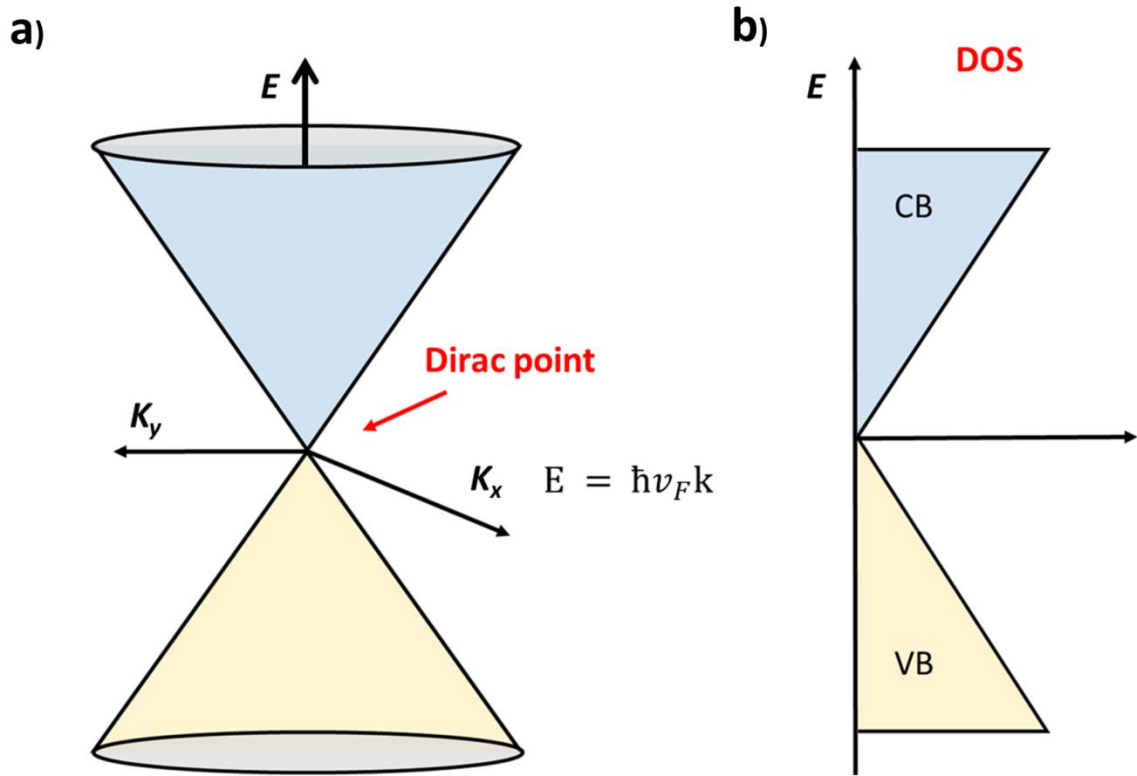


Fig. 2.3. (a) Illustration of the electronic band structure of graphene shows that valance and conduction bands meet at the Dirac points (K and K') and (b) density of states.

2.3. Properties and potential applications of graphene

The unique electronic band structure of graphene has opened up new opportunities for various future applications. For example, a high specific surface area ($2630\text{m}^2\text{g}^{-1}$), good thermal conductivity ($5000\text{Wm}^{-1}\text{K}^{-1}$), a high Young's modulus (1.0TPa) [17,18], and optical transmittance (97.7%) [19] give it the potential to have applications in photovoltaic cells, sensors, touch screen panels, flexible, foldable, and stretchable electronic devices. Besides, graphene can be incorporated into many composite materials for applications where strength and weight are limiting factors, for example, in the aerospace industry. Finally, the high electrical mobility of graphene can be used to fabricate ultra-fast electronic transistors [20]. Besides, some of the most promising applications of graphene in microelectronics are

transistors, sensors, heat spreaders, and photodetectors. The potential applications of graphene in different sectors are summarized in Fig. 2.4.

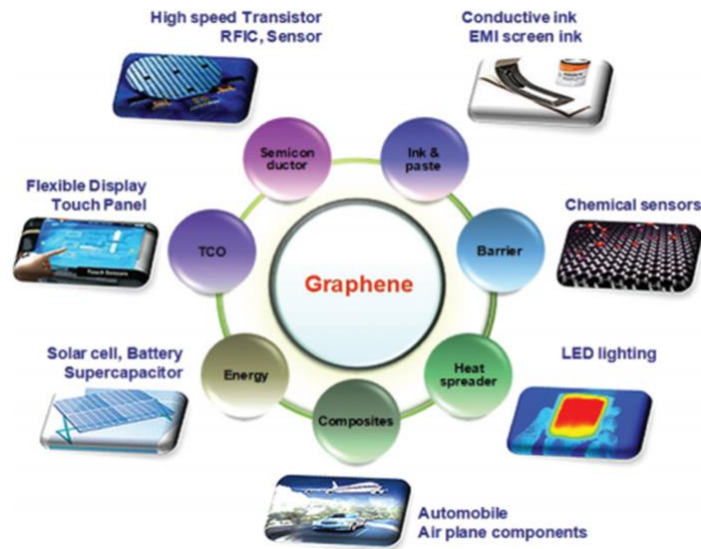


Fig. 2.4. Potential applications of graphene in different sectors [21].

Although graphene has potential for numerous applications, the availability of methods suitable for producing a large-area and high-quality graphene remains a central issue. In order to overcome this issue, different approaches are used to grow graphene, as described in the next section.

2.4. Synthesis of graphene

Generally, graphene synthesis methods can be divided into two main categories: the top-down approach and the bottom-up approach, as shown in Fig. 2.5. The top-down technique includes chemical synthesis, mechanical and chemical exfoliation methods. In the top-down method, the graphene sheet is obtained by exfoliation or separation of highly ordered pyrolytic graphite (HOPG). This approach has several challenges, such as surface defects that appear during sheet separation and the separated sheets re-agglomerating afterward. Also, top-down methods are tedious and offer a low yield. In the bottom-up approach, graphene

film is obtained by building up nanoscale material through the atomic or molecular arrangement of carbon atoms. This approach includes the unzipping of carbon nanotube, epitaxial growth, and CVD methods. Epitaxial growth produces high-quality graphene on substrates like SiC. However, the high cost of SiC crystal and high graphene growth temperature make this system incompatible with silicon mainstream technology. On the other hand, CVD is the most promising method to obtain graphene due to its CMOS compatibility, high quality, and wafer scalability. The CVD method also allows the synthesis of monolayer graphene, which is uniformly distributed over the entire wafer. This uniformity of graphene is attributed to the CVD growth mechanism, which is a self-limiting process. Below, the CVD method is discussed.

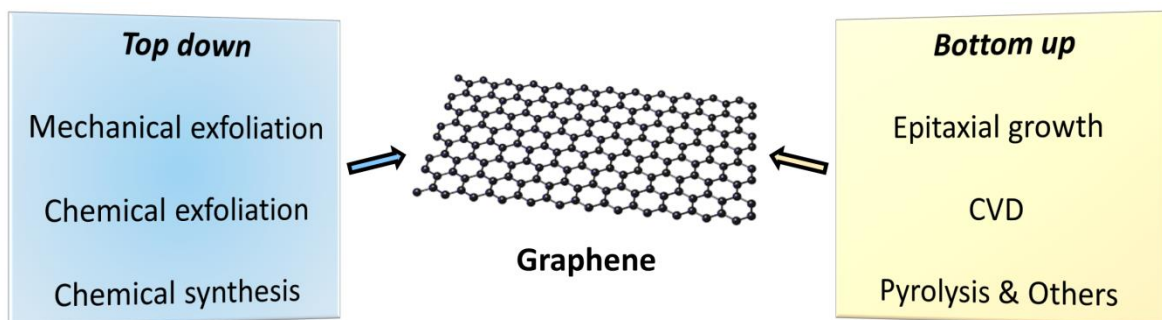


Fig. 2.5. Graphene synthesis methods.

2.5. Chemical vapor deposition

CVD is the most commonly used for obtaining graphene. In a CVD process, graphene is achieved by the thermal decomposition of hydrocarbon gas (methane, ethylene, and acetylene) in the presence of a metal catalyst. Therefore, this process is known as catalytic or thermal CVD. This method is versatile in that it enables the growth of graphene on various substrates in different forms and sizes, including thin or thick films, powder, aligned or entangled, on predefined sites of a patterned substrate, and so on. In addition to thermal

CVD, other types of CVD processes are plasma-enhanced (PECVD), cold wall, reactive, hot wall, and so on.

As the CVD process is the primary method employed in this thesis for the growth of graphene; therefore, it is deeply described in section 3.1. However, the most prominent parameters which are used in the CVD of graphene are described here.

Pressure

Pressure in the CVD chamber is considered a critical parameter as it can influence the graphene quality. Graphene is reported to be grown using different pressure ranges, such as high vacuum, low pressure, and atmospheric pressure. Ideally, the vacuum level should be minimized before graphene growth in order to get high purity layers. On the other hand, substrates like Ge can facilitate high-quality graphene growth over large areas, even at atmospheric pressure.

Carbon source

Gas, liquid, and solid precursors are used for graphene growth, being mainly hydrocarbons and polymers. The most commonly gaseous carbon precursors for the CVD of graphene are methane (CH_4), ethylene (C_2H_4), and acetylene (C_2H_2). The dehydrogenation energy of these gases is 410, 443, and 506 kJ/mol, respectively [22,23]. The C–H bond energy is the key parameter for controlling the dehydrogenation temperature and required energy. As the dehydrogenation of the precursors is an endothermic process; therefore, a higher temperature is usually needed to break the C–H bond. One way to reduce this energy could be the use of a plasma source, being another way is the use of a catalytic substrate.

Substrate

Ideally, graphene should be grown on a dielectric substrate because it can favor the fabrication of graphene-based devices. However, the limited catalytic efficiency of dielectrics is the main problem, which is described in the following section 2.6. On the other hand, metallic substrates are attractive for graphene growth due to their high catalytic efficiency. The catalytic power of transition metals and some of their compounds is well known and arises from their partially filled d-orbitals or from the formation of intermediate compounds that favors the reactivity of the precursor gases. Hence, catalysis by metals results from their ability to provide low activation energy pathways for reactions either by changing the oxidation states or forming the intermediate compounds. For graphene growth, Ni and Cu are the most commonly used metal catalysts though graphene has been obtained on other metallic substrates (e.g., Ru, Ir, Pd, etc.) [24–26]. The graphene growth mechanisms on Cu and Ni are entirely different and are dependent on their carbon solubility. The growth of graphene on Cu and Ni is discussed in the next sections (2.7 and 2.8). Besides Ni and Cu, Ge also shows good catalytic activity and therefore is another promising substrate for the growth of graphene. The growth mechanism of graphene on Ge is described in the following section 2.9.

2.6. Graphene growth on dielectrics

The growth of graphene films directly on CMOS-compatible substrates such as SiO₂, BN, MgO, Al₂O₃, Si₃N₄, and Si would be ideal because of its several advantages. First of all, it can reduce time and processing costs by avoiding a complicated transfer step, which is usually needed in the case of a metallic substrate. Secondly, the direct growth of graphene on insulating substrates can prevent processing contamination issues and defects introduced

by the transfer step. However, the inert catalytic activity of dielectrics causes the growth of nanocrystalline graphene containing many defects. Therefore, to overcome the energy barrier for the dehydrogenation on dielectric substrates, a higher growth temperature (1100–1200°C) is usually required.

Nevertheless, the growth of graphene on dielectrics can be improved with some additional measures, such as surface oxygen, plasma assistance, etc. The presence of energetic electrons, excited atoms or molecules, and free radicals generated in the plasma region can assist the decomposition of precursor gases, thus partly compensating for the weak catalytic nature of insulating substrates. For example, a literature study has reported the growth of defective nano-meter-sized graphene films on SiO₂ by employing a remote plasma-enhancement CVD system (Fig. 2.6) [27]. Using the same approach, the authors also obtained nanographene films on other dielectric substrates (Al₂O₃, Si, SiC, mica, and quartz).

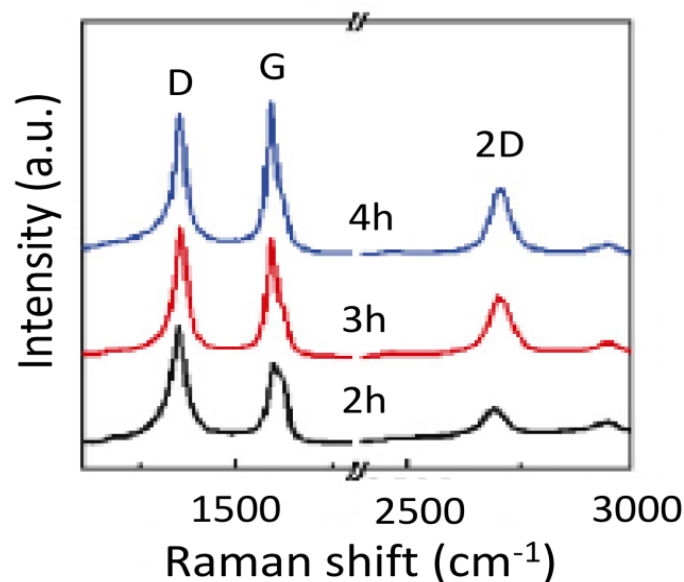


Fig. 2.6. Raman spectra of nanographene films grown on SiO₂ substrates with different growth durations [27].

Chen et al., on the other hand, used an oxygen-aided atmospheric pressure chemical vapor deposition (APCVD) process for the pyrolysis of methane and achieved two types of

graphene [28,29]. One kind of graphene was polycrystalline, with a lateral grain size of about 300nm. This growth process requires several hours to form graphene; however, the growth of secondary flakes and cracks forming in the monolayer graphene are drawbacks [29]. The other type of graphene was single-crystalline with a domain size of about 10 μ m, but it requires an extremely long processing time (72 hours) [28].

So far, no strategy has been successful in producing good-quality graphene on dielectric substrates; therefore, its growth on other substrates has also been investigated. In the next sections, the growth of graphene on different substrates is reviewed.

2.7. Graphene growth on copper

Although copper was not used for the growth of graphene in this PhD work; nevertheless, this section discusses the graphene/copper system for the sake of the readers. The growth of graphene on copper is simple and straightforward and is attributed to the low carbon solubility of Cu (0.001–0.008 weight% at \sim 1084 $^{\circ}$ C), as shown in Fig. 2.7 [30]. The graphene growth mechanism on Cu will be described below.

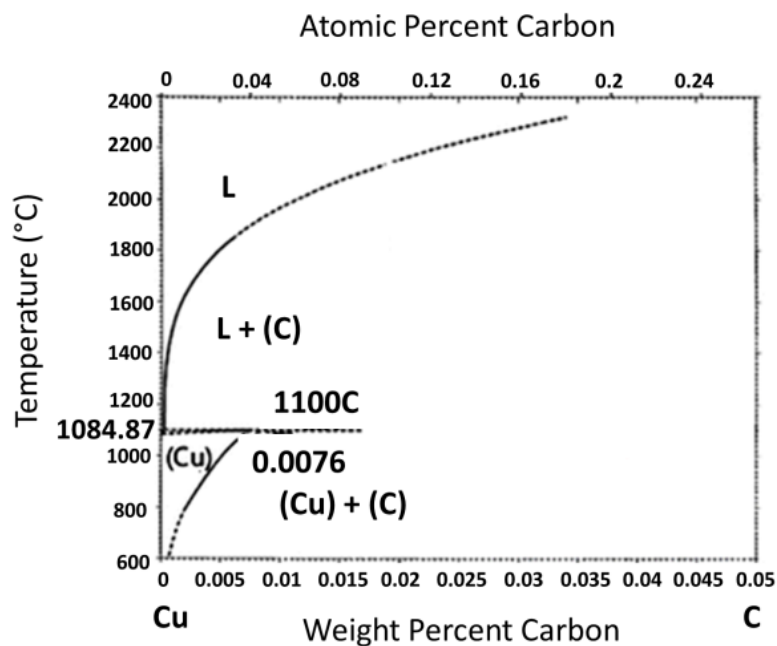


Fig. 2.7. Phase diagram of the Cu-C system [30].

Graphene growth mechanism on copper

Graphene on the surface of Cu is formed via a surface-mediated process due to its low carbon solubility, as illustrated in Fig. 2.8. In a surface-mediated process, the growth of graphene starts immediately after the dehydrogenation of the hydrocarbon. However, after forming the first layer, graphene growth stops as no more Cu surface is available for hydrocarbon dehydrogenation. Thus, the growth of graphene on Cu is a self-limiting process. This self-limiting growth mechanism of graphene on Cu has been experimentally proved with the help of the isotopic labeling technique in conjunction with Raman spectroscopic mapping [31].

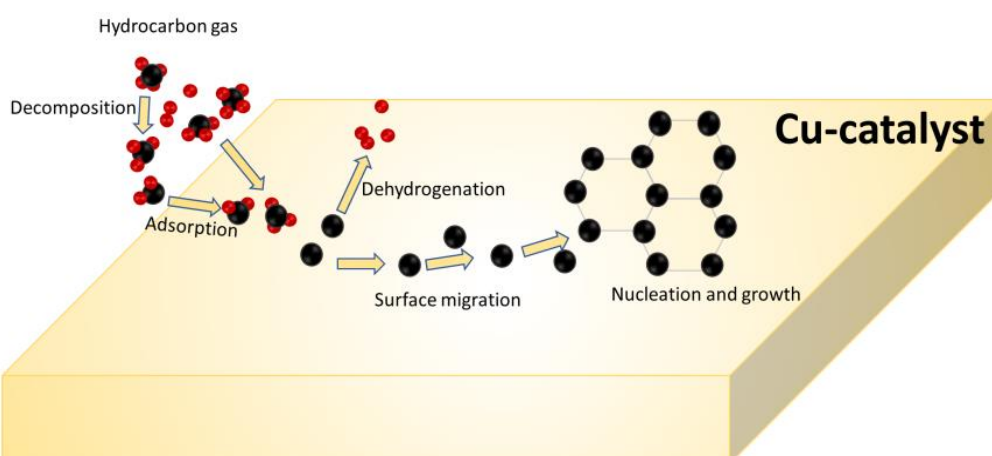


Fig. 2.8. Illustration for the Cu-catalyst-dependent growth of graphene.

Crystal structure of copper

Crystalline Cu has a face-centered cubic (fcc) structure, and its (111) surface facilitates monolayer graphene growth due to its low surface energy than other Cu orientations. Also, Cu(111) has a hexagonal shape similar to that of graphene; the lattice mismatch between graphene and Cu(111) structures is small (3.8%) as compared to other Cu orientations [32]. There are three different adsorption configurations of graphene (such as top-fcc, fcc-hcp, and top-hcp) on Cu(111), as illustrated in Fig. 2.9. Among them, fcc-hcp is the most

thermodynamically favorable adsorption site as it allows perfect matching of Cu(111) lattice and the honeycomb structure of graphene [33].

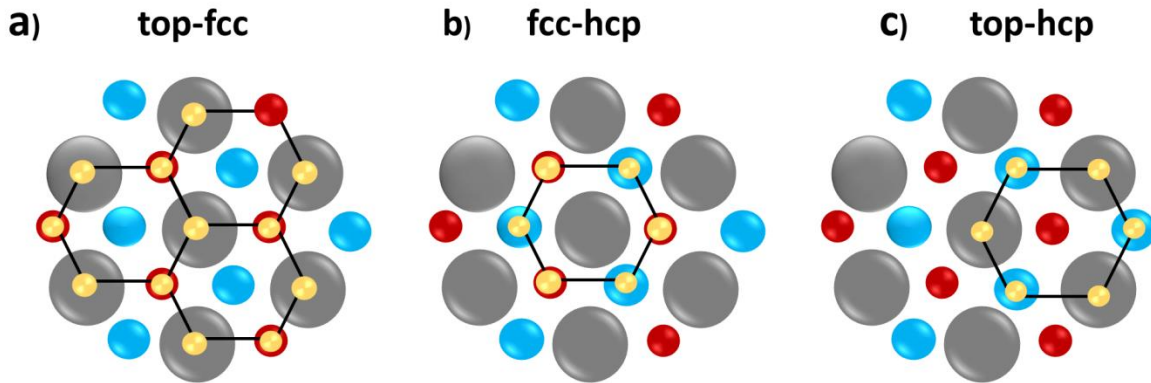


Fig. 2.9. Different adsorption configurations of graphene on Cu(111). Grey, blue, and red circles denote 1st, 2nd, and 3rd Cu layers, respectively [Recreated from Ref. 33b].

Problematics

Indeed, Cu is widely used to obtain large-area monolayer graphene films; however, this system has several drawbacks. For example, rotated graphene domains are usually formed on Cu. This is attributed to the large lattice-mismatch and weak interactions between the graphene and Cu substrate [34]. The coalescence of graphene domains results in grain boundary formation. The results obtained from aberration-corrected annular dark-field scanning transmission electron microscopy (ADF-STEM) showed the atomic structure of a typical grain boundary, which is formed due to the coalescence of two graphene domains that are rotated about 27° (Fig. 2.10a) [35]. A high magnification image in Fig. 2.10b further indicates that the grain boundary is not straight, and the defects along grain boundaries are not periodic [35]. Therefore, grain boundaries can be seen as line defects of graphene that break the in-plane lattice symmetry. The Raman mapping (Fig. 2.10c) shows that the intensity of the defect peak is higher at the grain boundary than within the grains, demonstrating the defective nature of the grain boundaries [36]. It has also been shown

that grain boundaries are responsible for the degradation of graphene's electronic properties [37,38].

Furthermore, the presence of post-transfer Cu-contaminations is another issue related to the graphene/Cu system. Because of these drawbacks, copper substrates were not selected for the growth of graphene in this PhD work.

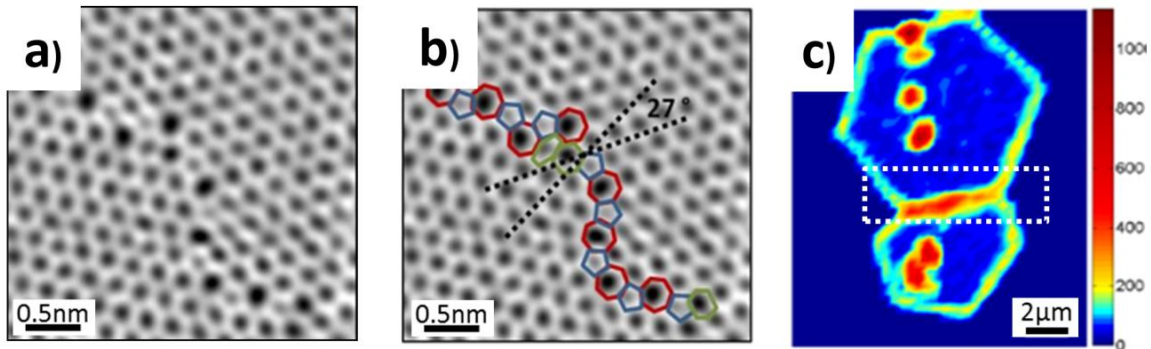


Fig. 2.10. (a–b) ADF-STEM images of the graphene transferred onto the TEM grid show the grain boundary defect formed due to two rotated graphene grains [35]. (c) Raman mapping indicates a higher intensity of defect peak at the boundary (dotted area) between two grains [36].

2.8. Graphene growth on nickel

In contrast to copper, the carbon solubility in Ni is high (0.6 weight % at ~1326°C), as shown in Fig. 2.11 [30].

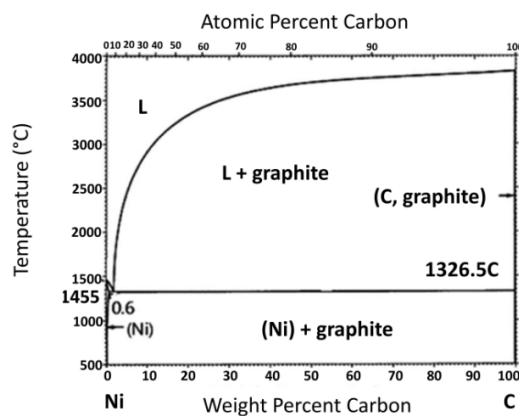


Fig. 2.11. Phase diagram of the Ni-C system [30].

Hence, the growth mechanism of graphene on Ni is different than that of Cu, as discussed below.

Graphene growth mechanism on nickel

Graphene on Ni grows by a segregation process, which is attributed to its high carbon solubility. The segregation process occurs in three steps. The first step involves the decomposition and dehydrogenation of hydrocarbons on the surface of Ni. In the second step, the carbon atoms diffuse into Ni. Lastly, graphene forms via segregation and precipitation of the carbon from the bulk to the surface of the metal upon cooling. Fig. 2.12 shows the schematic illustration of the segregation process for the graphene growth on Ni.

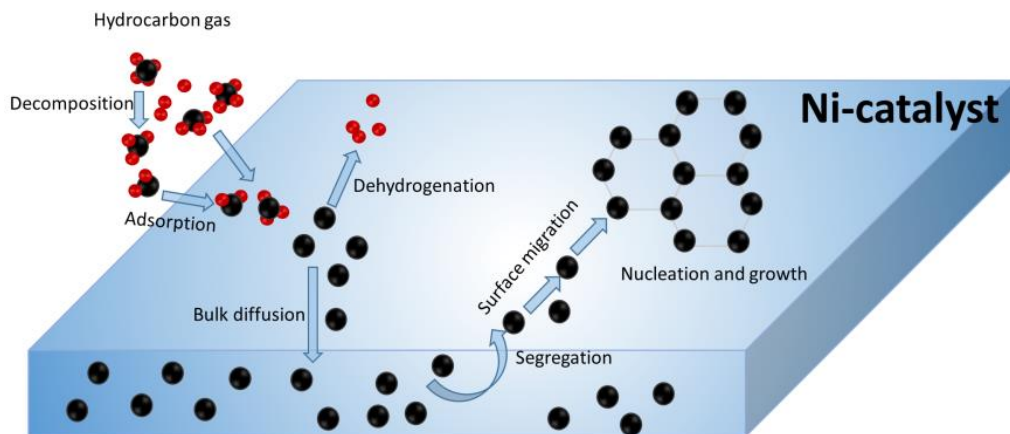


Fig. 2.12. Illustration for the Ni-catalyst-dependent growth of graphene.

Crystal structure of nickel

Ni has a close-packed fcc structure. The C–C bond length in the graphene sheet is 1.42\AA , which is very close to the characteristic distance of the Ni(111) surface ($\frac{a_{Ni}}{\sqrt{6}} = 1.44\text{\AA}$), where $a_{Ni} = 3.52\text{\AA}$ is the lattice parameter for fcc nickel lattice [39]. Besides, the in-plane lattice constant of the graphene (2.46\AA) is also very close to the lattice constant of the Ni(111) surface unit cell (2.49\AA). Due to this small lattice mismatching, graphene

exhibits only one commensurate (1×1) atomic structure on Ni(111). Among all orientations, the growth of graphene on Ni(111) orientation is therefore widely investigated. There are four different possible adsorption configurations of graphene on Ni(111), as shown in Fig. 2.13.

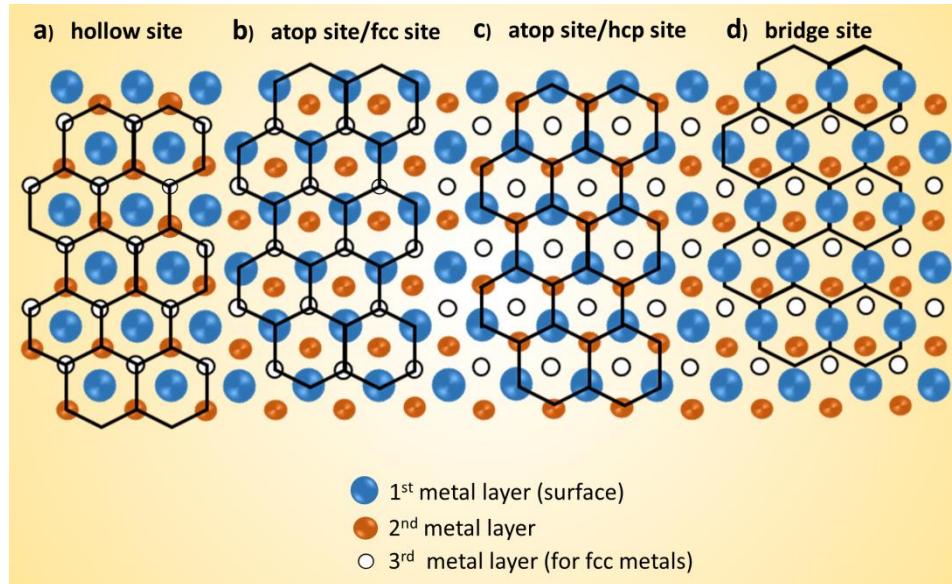


Fig. 2.13. The four different adsorption configurations of graphene on Ni(111) [Recreated from Ref. 40].

Previous works have shown that the fcc is the most stable adsorption configuration of graphene on Ni(111) because of its higher work of adhesion 0.81Jm^{-2} than 0.77Jm^{-2} and 0.38Jm^{-2} for hcp and hollow adsorption sites, respectively [41,42].

Problematics

The atomically smooth surface of Ni substrates without grain boundaries is essential for the growth of uniform monolayer graphene. In this respect, single-crystal Ni(111) substrate should be used as its smooth surface favors monolayer graphene growth (Fig. 2.14a). Though mono-bilayer graphene coverage over 90% of single-crystal substrates has been achieved [43], the high costs and limited sizes of Ni(111) are the main drawbacks. At this

point, polycrystalline Ni films are attractive for graphene growth due to their large-scale availability and compatibility with Si microelectronics. Indeed, mono-bilayer graphene up to 87% area has been reported [43,44], but the polycrystallinity of Ni makes the graphene growth a complicated process. Grain boundaries (GBs) in polycrystalline Ni are the most preferential sites for the growth of multilayer graphene, whereas Ni(111) grains favor the growth of monolayer graphene (Fig. 2.14b).

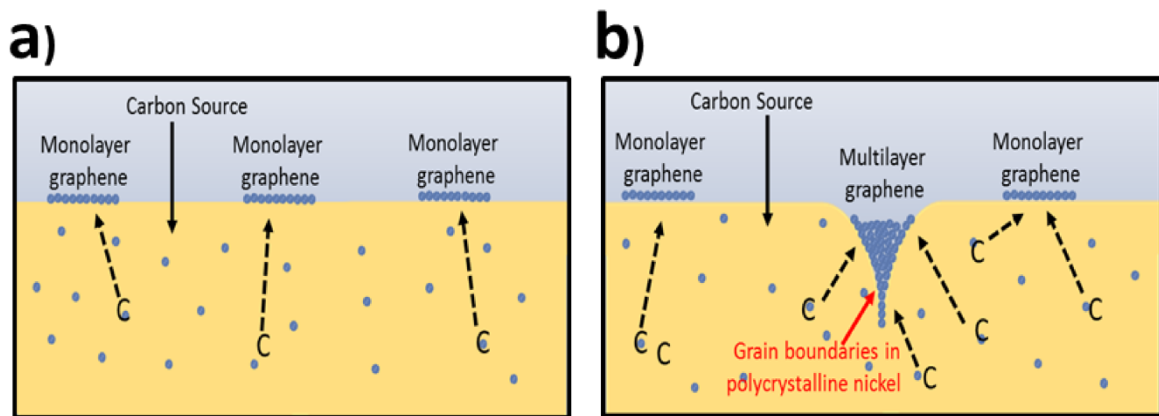


Fig. 2.14. A comparison of graphene growth on (a) single-crystal Ni(111) and (b) polycrystalline Ni [Recreated from Ref. 43].

Consequently, thicker graphene films are formed at the grain boundaries than within the grains. Also, the carbon solubility in Ni is very high and temperature-dependent; therefore, Ni film acts as a carbon reservoir, which is another issue. The maximum carbon contents dissolved in Ni depends on the thickness of the film used. For instance, more carbon atoms dissolved in thick Ni films at high temperatures as compared to thin films. As a result, few-layer graphene or graphite grow on the surface of Ni films through segregation or precipitation. Hence, it is challenging to control the number of graphene layers on the surface of polycrystalline Ni.

Nonetheless, by optimizing various parameters, the thickness of graphene can be controlled to some extent. For instance, the cooling temperature is an important parameter that

influences carbon segregation; therefore, the growth of graphene at different cooling rates has been reported [45]. Results showed that faster cooling rates result in a quenching effect due to which carbon atoms lose their mobility before they diffuse to the surface; however, thicker and defective graphene films are obtained. On the other hand, medium cooling leads to four or fewer graphene layers; slow cooling allows carbon to diffuse into bulk; therefore, graphene films are not formed (Fig. 2.15).

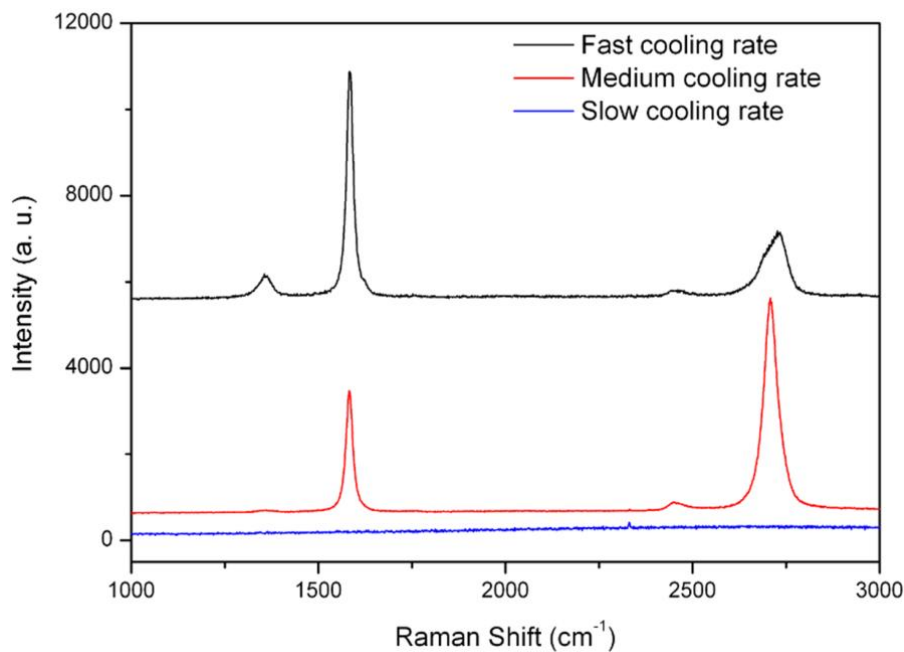


Fig. 2.15. Raman spectra of segregated carbon at Ni surface with different cooling rates [45].

In addition to the cooling rate, the concentration of precursors can also affect the layer control of graphene. Reina et al. found that the multilayer graphene nucleation can be controlled by decreasing the concentration of methane (from 0.7 to 0.5– 0.6%) and using a low cooling rate ($dT/dt < 25^{\circ}\text{C}$) [44].

2.9. Graphene growth on germanium

Compared to Cu and Ni catalysts, the growth of graphene on Ge substrates is relatively “fresh” and has not been investigated deeply. Unlike Si, Ge does not form carbides due to

its low carbon solubility and therefore has the potential to synthesize graphene (Fig. 2.16)

[46]. Other advantages of Ge are its high catalytic activity and CMOS compatibility.

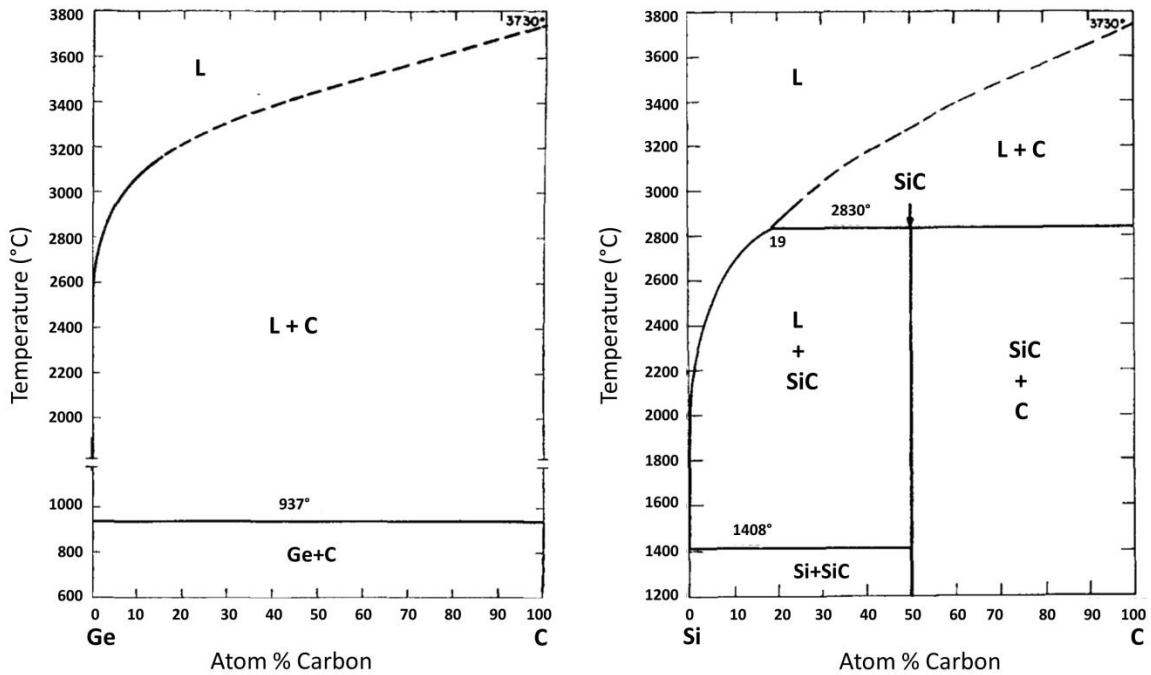


Fig. 2.16. Phase diagram of the systems Ge-C (left) and Si-C (right) [46].

Also, a small difference in the thermal expansion coefficient between graphene and Ge leads to the growth of wrinkle-free graphene films. It should also be noted that graphene transferred from the Ge layer is free from metal contaminants, making this system promising for further applications and device fabrication. Like copper, the graphene growth on Ge occurs via a surface-mediated process, as explained below.

Graphene growth mechanism on germanium

The low carbon solubility of Ge causes the growth of graphene via a surface-mediated process. In a surface-mediated process, as already discussed in section 2.7, the growth of graphene starts immediately after the dehydrogenation of the hydrocarbons. This process is also self-limiting as the first layer of graphene's growth completely covers the catalytic

surface, which stops the further growth of graphene. Fig. 2.17 depicts the growth mechanism of graphene on Ge.

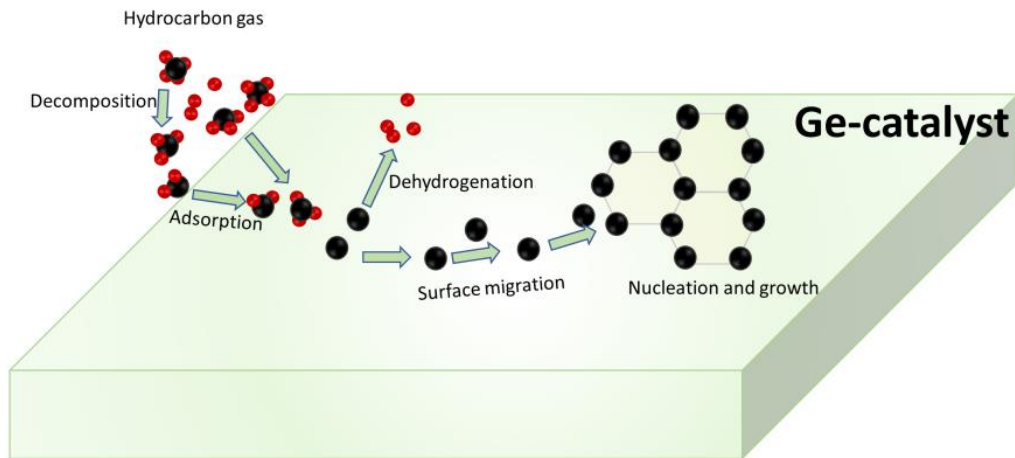


Fig. 2.17. Surface-mediated growth of graphene on Ge.

Crystal structure of germanium

Ge is referred to as a group IV element and has a diamond structure. The crystal structure of Ge consists of two interpenetrating FCC lattices displaced from each other along body diagonal by one-fourth of its length, as demonstrated in Fig. 2.18. Each Ge atom in such a structure is bonded with four others in a tetrahedral configuration. The bonding between Ge atoms is very strong and is highly directional. Nevertheless, some of the Ge bonds break off upon truncating the bulk. Such a configuration is unfavorable; therefore, the surface atoms try to rearrange themselves in order to minimize their surface energy; this process is known as surface reconstruction. Surfaces are named after the plane of the bulk crystal to which they are parallel, for instance, (001), (110), and (111). Therefore, the crystal structures of different Ge orientations are different from that of the bulk Ge (Fig. 2.18).

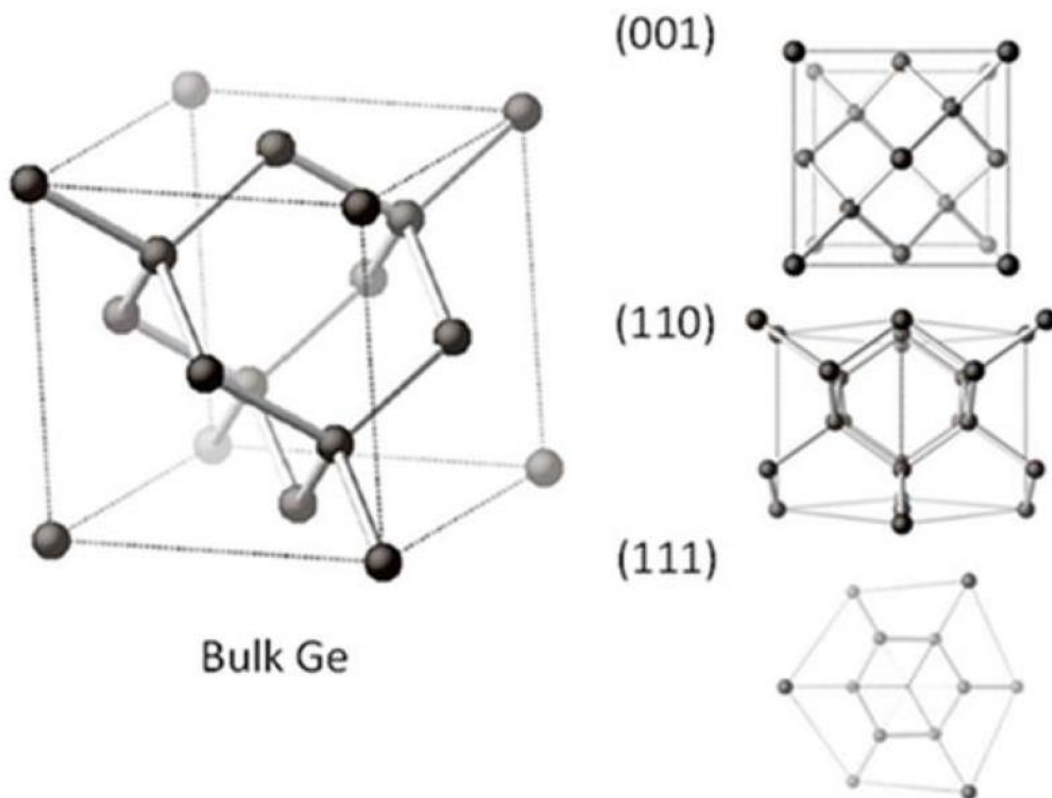


Fig. 2.18. Crystal structures of bulk Ge and different Ge orientations [47].

Different surfaces of Ge reconstruct differently in order to eliminate dangling bonds. For example, each atom in an ideal (001) surface has two dangling bonds (Fig. 2.19a). This surface reconstructs to form a Ge dimer, leading to a (2×1) structure (Fig. 2.19b). Furthermore, dimer buckling gives rise to $p(2 \times 2)$ and $c(4 \times 2)$ reconstructed surfaces when the adjacent rows are in phase and out of phase, respectively (Figs. 2.19c and d).

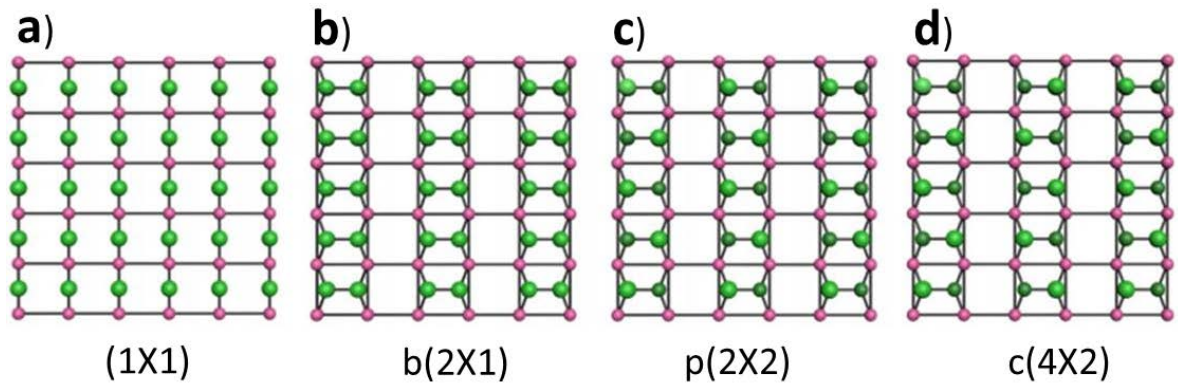


Fig. 2.19. The top view of Ge(001) surface, green, dark green, and purple balls represent Ge atoms present at the top, the lower surface, and bottom layers, respectively. (a) Unreconstructed 1×1 surface (b) $b(2 \times 1)$ (c) $p(2 \times 2)$ and (d) $c(4 \times 2)$ surface reconstructions [48].

Like Ge(001), (110) oriented Ge also exhibits two reconstructed surfaces, the $c(8 \times 10)$ and (16×2) , which are confirmed by STM and LEED experiments [49,50]. Both superstructures feature rows of the pentagonal cluster of adatoms, as demonstrated in Fig. 2.20, where each red circle denotes a pentagonal cluster. The surface reconstruction of Ge(110) is strongly dependent on the annealing temperature [50].

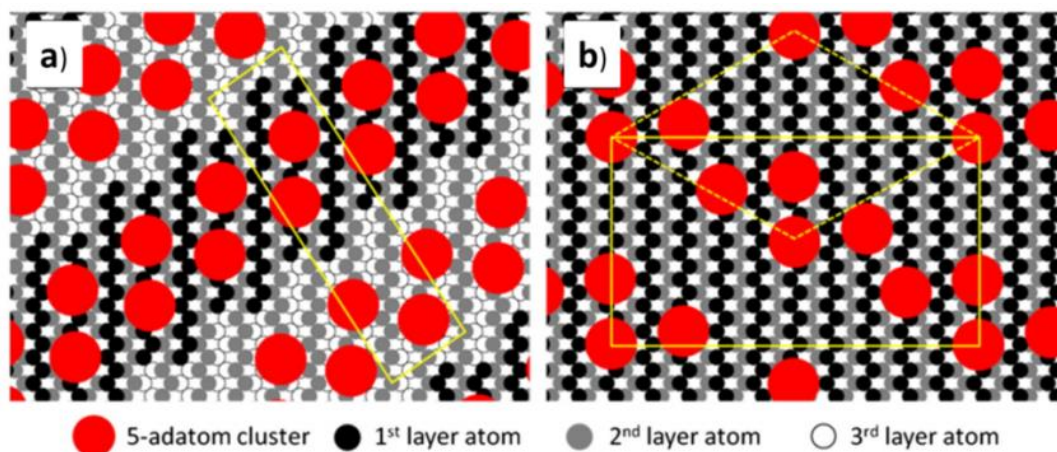


Fig. 2.20. Models of (a) (16×2) and (b) $c(8 \times 10)$ surface reconstructions of Ge(110). A single red circle represents the pentagonal five-adatoms clusters [50].

It should be noted that reconstructed surfaces of Ge (001) and Ge(110) are not ideal to confine the graphene with well-defined alignment; however, a stabilized or disordered (1 × 1) surface may play a critical role in guiding the graphene growth. This could be achieved at higher temperatures or by hydrogen termination. Indeed, large-area single-crystal graphene films are obtained on hydrogen-terminated Ge(110) substrates (Fig. 2.21) [51].

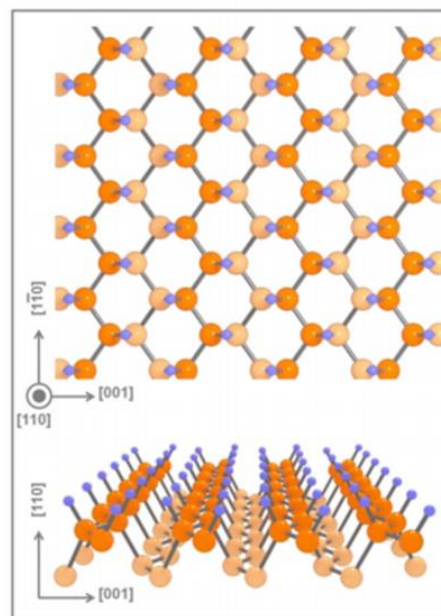


Fig. 2.21. Top (above) and side (below) views of hydrogen-terminated Ge(110) [51].

Problematics

As mentioned above, graphene growth on Ge is a new topic; hence, parts of the problematics were discovered during this PhD work, for example, surface reconstruction of Ge(001) into hills and valleys structures during the graphene growth process. It was found that the faceted morphology of Ge led to the growth of two rotational graphene domains. Indeed, the growth of two rotational graphene domains on Ge(001) has been presented (Fig. 2.22) [52]. The presence of two orientations of graphene is not desired. It can negatively impact the graphene's electrical mobility similar to that of the graphene/Cu

system, due to the grain boundary scattering. Like Si, which is highly reactive with oxygen in the air, forming its stable native oxide SiO_2 , Ge also forms an oxide layer when it interacts with atmospheric oxygen. The Ge oxide layer consists mainly of GeO_2 and suboxides (GeO_x). The presence of oxygen at the graphene/Ge interface can be another problem as it can affect the properties of graphene. Graphene/Ge-related issues will be discussed in chapter 4.

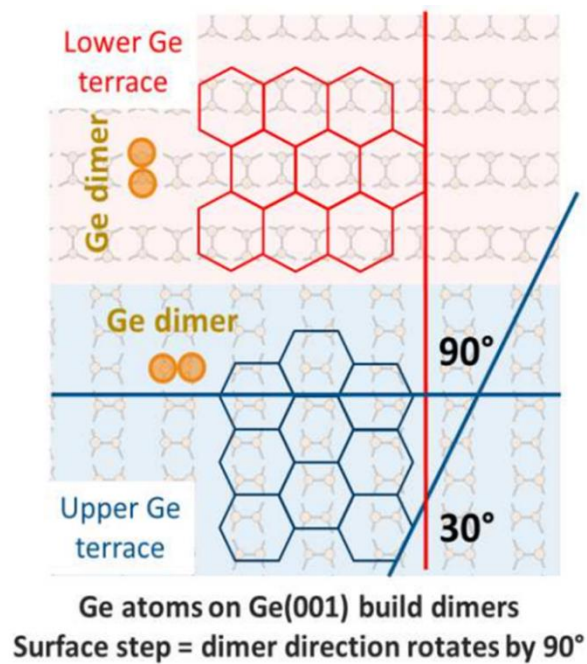


Fig. 2.22. The presence of two orientation domains of graphene on Ge(100) demonstrates that the graphene growth is correlated with the direction of Ge dimer rows [52].

PART II

EXPERIMENTAL

CHAPTER 3

3. EXPERIMENTAL SETUP AND CHARACTERIZATION TECHNIQUES

This chapter introduces the experimental protocols and characterization techniques used in this thesis. In the first section, the graphene synthesis method of chemical vapor deposition is described. Further, the main characterization techniques such as Raman spectroscopy, X-ray photoelectron spectroscopy (XPS), X-Ray diffraction (XRD), scanning electron microscopy (SEM), optical microscopy (OM), atomic force microscopy (AFM), electron backscattering diffraction (EBSD), spectral ellipsometry, reactive ion etching (RIE), time-of-flight secondary ion mass spectrometry (ToF-SIMS), and electrical transport measurements are briefly described.

3.1. Basics of chemical vapor deposition

Chemical vapor deposition is the most widely used materials-processing technology. The majority of its applications involve applying solid thin-film coatings to surfaces. But it is also used to form high-purity bulk materials and powders as well as producing composite materials via infiltration techniques. In a CVD process, chemical constituents react in the vapor phase on or near the heated surface and form a solid deposit. CVD technology combines several engineering and scientific disciplines, such as plasma physics, thermodynamics, fluid dynamics, kinetics, and chemistry. The chemical reactions used in CVD are considerable which include hydrolysis, thermal decomposition (pyrolysis), reduction, oxidation, disproportionation, nitridation, and carburization. They can be used

either singly or in combination. The most important methods to activate these reactions are as follows [53]:

- Thermal activation typically takes place at high temperatures ($>900^{\circ}\text{C}$), though the temperature can also be lowered considerably using Metallo-organic precursors (MOCVD) or aromatic hydrocarbons.
- Plasma activation takes place at much lower temperatures (from room temperature to 500°C).
- Photon activation, usually with shortwave ultraviolet radiation, can occur by the direct activation of a reactant or by the activation of an intermediate.

Until recently, most CVD operations were relatively simple and could be readily optimized experimentally by changing the activation method, the reaction chemistry, or the deposition variables until a satisfactory deposit was achieved. However, many of the CVD processes are becoming increasingly complicated, with much more exacting requirements, which would make the empirical approach too inconvenient. In most cases, a theoretical analysis is an essential step that should predict any of the following: reaction mechanism, the composition of the deposit (i.e., stoichiometry), the chemistry of the reaction (intermediate steps, by-products), and the structure of the deposit (i.e., the geometric arrangement of its atoms). Then, this analysis may provide a guideline for an experimental program and considerably reduce its scope, save time and effort [53].

A CVD reaction is governed by thermodynamics, which is a driving force that indicates the direction the reaction is going to proceed; and kinetics, which defines the transport process and determines the rate-controlling mechanism, in other words, how fast it is going. The sequence of steps that take place during a CVD reaction is shown in Fig. 3.1 and can be summarized as follows:

- (1) Introduction of the reactant gases from the gas inlet by forced flow to the reaction zone
- (2) Adsorption of reactants on the surface of the substrate
- (3) Surface diffusion to the growth sites, surface chemical reactions, and nucleation leads to the formation of the film
- (4) Desorption of the gaseous by-products from the surface
- (5) Transportation of the by-products away from the reaction zone

During the CVD process, the reactant gases not only react with the substrate material at the surface of the wafer (or very close to it) but also in the gas phase in the reactor's atmosphere. A reaction that occurs in the gas phase is known as homogeneous, while the reaction that occurs at the surface of the substrate is known as heterogeneous. The growth process of graphene is a heterogeneous catalytical chemical reaction.

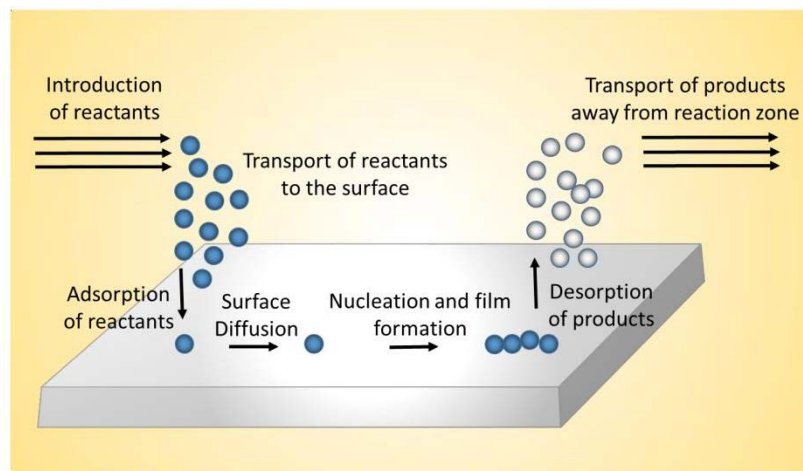


Fig. 3.1. The sequence of events takes place in a CVD reaction.

In this PhD work, graphene on Ni and Ge substrates has been grown in a thermal CVD system at IHP. A simplified scheme and picture of the CVD tool are provided in Fig. 3.2 and Fig. 3.3 (left). In this system, the sample is placed on a horizontal plate inside the CVD chamber, and a carbon source (CH_4 or ethylene) and carrier gas (hydrogen and argon) are then introduced into the chamber. Hence, graphene is obtained over 8-inch wafers.

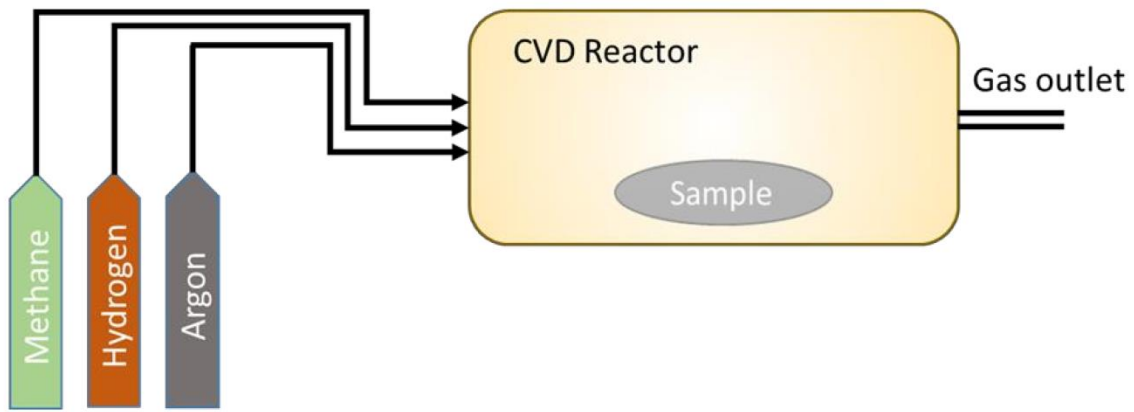


Fig. 3.2. A simplified illustration of the CVD system.

It is worth mentioning here that pre-experiments for graphene growth on Ni have been performed in a high vacuum CVD system, as shown in Fig. 3.3 (right). Ni substrates are mounted on a rotating substrate holder in this system. One of the advantages of this system is that the processed samples can be transferred in-situ to the attached XPS tool (whose base pressure is about 10^{-10} mbar) in order to investigate their surfaces.



Fig. 3.3. Pictures of the CVD systems that were used for graphene growth in this PhD work.

3.2. Raman spectroscopy

Raman spectroscopy is a non-destructive characterization tool to probe carbon-based materials, including three-dimensional graphite and amorphous carbon, two-dimensional graphene, and one-dimensional carbon nanotubes, etc.

Raman spectroscopy is used to differentiate single and bilayer graphene from bulk graphite

and to identify the stacking order of the graphene layers [54–57]. Besides, a multitude of characteristics, for instance, doping level, structural defects, edge states (armchair or zigzag), and strain in graphene, can also be determined from the Raman measurements [58–60].

In this PhD work, the quality and properties of the grown graphene films were investigated using a Renishaw inVia Raman microscope in the Raman lab at IHP (Fig. 3.4). In order to obtain Raman spectra, different excitation wavelengths (514nm and 532nm), a 100nmx objective, and a laser spot size of $\sim 1\mu\text{m}$ were used.



Fig. 3.4. Picture of the Renishaw Raman microscope from the Raman lab at IHP.

Single spot measurements were usually performed to get the Raman spectrum; however, micro Raman mappings were performed for quantitative analysis. For spectral analysis, Renishaw software was used. Raman spectroscopy was frequently used during this PhD work; therefore, it is deeply discussed in this section.

The Raman effect

When light interacts with a sample, it can be transmitted, absorbed, and scattered. Raman spectroscopy is used to study the inelastic scattering of light. The process of the inelastic

scattering of light was described by an Indian scientist Sir Chandrasekhara Venkata in 1928; therefore, it is also known as the Raman Effect.

The basic concept of the Raman Effect can be understood within the framework of the classical electromagnetic theory, which is briefly described here. An applied electric field induces polarization \vec{P} in the solid, which is given by:

$$\vec{P} = \alpha \cdot \vec{E} \quad 3.1$$

In the above equ. (3.1), \vec{P} denotes the polarization vector, which describes the displacement between positive and negative charges due to the applied electric field, and α is the polarizability tensor. \vec{E} denotes the electric field, and it can be written as:

$$\vec{E} = \vec{E}_0 \sin \omega_i t \quad 3.2$$

The presence of lattice vibrations of frequency ' ω_q ' in a crystal modulates the polarizability ' α ' of the atoms so that:

$$\alpha = \alpha_0 + \alpha_1 \sin \omega_q t \quad 3.3$$

Thus, the polarization induced in the crystal becomes:

$$\vec{P} = (\alpha_0 + \alpha_1 \sin \omega_q t) \cdot \vec{E}_0 \sin \omega_i t \quad 3.4$$

$$\vec{P} = \vec{E}_0 \left[\alpha_0 \sin \omega_i t + \frac{1}{2} \alpha_1 \cos(\omega_i - \omega_q) t - \frac{1}{2} \alpha_1 \cos(\omega_i + \omega_q) t \right] \quad 3.5$$

The above equ. (3.5) describes that light can be scattered both elastically (first term) and inelastically (second and third term) at frequencies ω_i and ω_q , respectively. The elastic scattering of light is known as Rayleigh scattering. On the other hand, inelastic scattering of light is classified into Stokes and anti-Stokes Raman scatterings. In the case of Stokes scattering, the incident photon loses energy with the creation of a phonon. However, if the scattered photon gains energy by absorbing a phonon, it is known as anti-Stokes Raman scattering. The minus plus signs in Equ. (3.5) indicate the Stokes and the anti-Stokes Raman

scattering, respectively. Anti-Stokes-Raman scattering is mostly weaker than Stokes-Raman scattering. Therefore, only Stokes scattering is mainly measured in Raman spectroscopy. A schematic illustration of the elastic and inelastic scattering of light is depicted in Fig. 3.5.

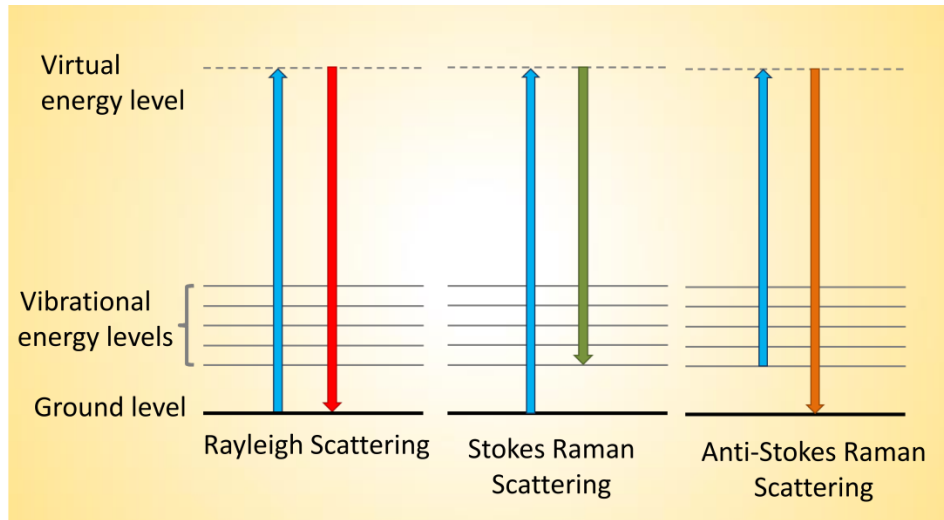


Fig. 3.5. A schematic illustration of Rayleigh scattering, Stokes, and Anti-Stokes Raman scattering.

As mentioned earlier, Raman spectroscopy is used to evaluate the quality and different properties of graphene. Below, the Raman spectrum of graphene is described.

Raman spectrum of graphene

A typical Raman spectrum of graphene is composed of G ($\sim 1580 \text{ cm}^{-1}$), D ($\sim 1350 \text{ cm}^{-1}$), and 2D ($\sim 2700 \text{ cm}^{-1}$) bands. The G peak is the only allowed first-order Raman band, which results from the C–C stretching mode. The process giving rise to the G mode begins with an incident photon that excites an electron-hole pair in graphene. The electron or the hole is scattered by either an iTO or iLO phonon at the Γ point [61]. Then, the electron-hole pair recombines by emitting a photon that is red-shifted by the amount of energy given to the phonon (Fig. 3.6a).

The second-order Raman process occurs in the 2D band due to the in-plane breathing mode of the carbon rings. The 2D band originates from the phonon at the K (or K') point in the first Brillouin zone. Fig. 3.6b represents the 2D band process in which an incident photon creates an electron-hole pair. The electron is inelastically scattered to the K' point by an iTO phonon. From the K' point, this electron is inelastically backscattered by a second iTO phonon to the K point in order to conserve momentum and energy. As two phonons are involved in the 2D Raman process, this is also known as a two-phonon Raman process.

The defect or D band is another second-order Raman process that involves an iTO phonon around the K point. However, unlike the 2D band, it requires a defect for the momentum conservation. In the case of the D band, the electron is scattered (inelastically) by an iTO phonon to the K' point and then is elastically backscattered to the K point by a defect, as can be seen in Fig. 3.6c. Since only one phonon is involved in this process; thus, this is known as one phonon process.

Due to the double resonance Raman process, both the D and 2D bands exhibit dispersive nature, meaning that their frequencies change as a function of the excitation energy of the laser used. The dispersion of the 2D and G bands is nearly 100 and 50 cm^{-1}/eV , respectively [58,61]. The double resonance process, therefore, carries information regarding the electronic structure of graphene as well as the dispersion of phonon.

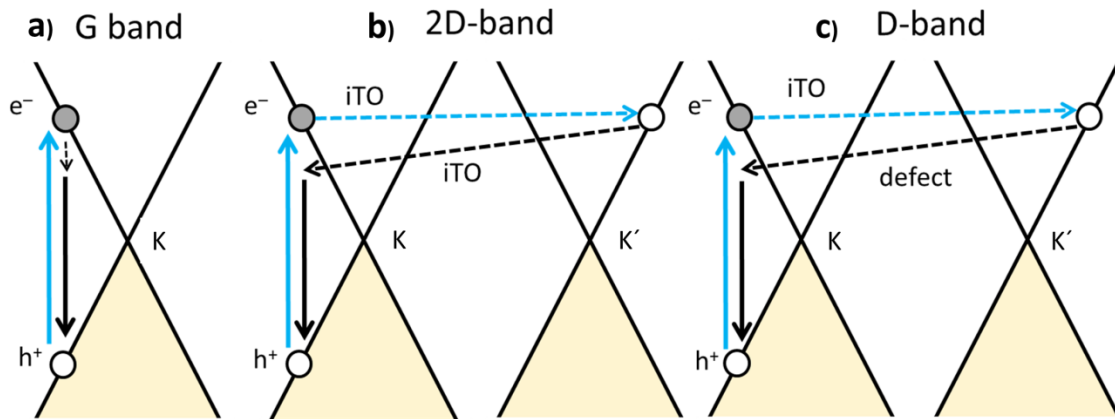


Fig. 3.6. Raman processes in graphene (a) first-order process (b–c) second-order process.

3.3. X-ray photoelectron spectroscopy

X-ray photoelectron spectroscopy (XPS) or Electron spectroscopy for chemical analysis (ESCA) is the most widely used surface analysis technique. Kai Siegbahn developed the instrumentation and the theory of XPS. He was awarded a noble prize in physics for his contributions in 1981. The most sophisticated application of the XPS method yields detailed information about the chemistry, electronic structure, organization, and morphology of the surface. Therefore, XPS is considered one of the most powerful analytical tools.

XPS was used in the present thesis for the surface analysis of the Ni, Ge, and graphene films. The XPS tool used to investigate the samples is shown in Fig. 3.7. As excitation wavelengths, $\text{MgK}\alpha$ ($E_{\text{exc}}= 1253.6\text{eV}$) and $\text{AlK}\alpha$ ($E_{\text{exc}}= 1486.6\text{eV}$) radiations were used. These radiations cause the emission of the core level electrons, which are analyzed by a concentric hemispherical analyzer at a detection angle of 45° . All the collected XPS spectra were analyzed via background subtraction and peak fitting procedures by CASA-XPS software.

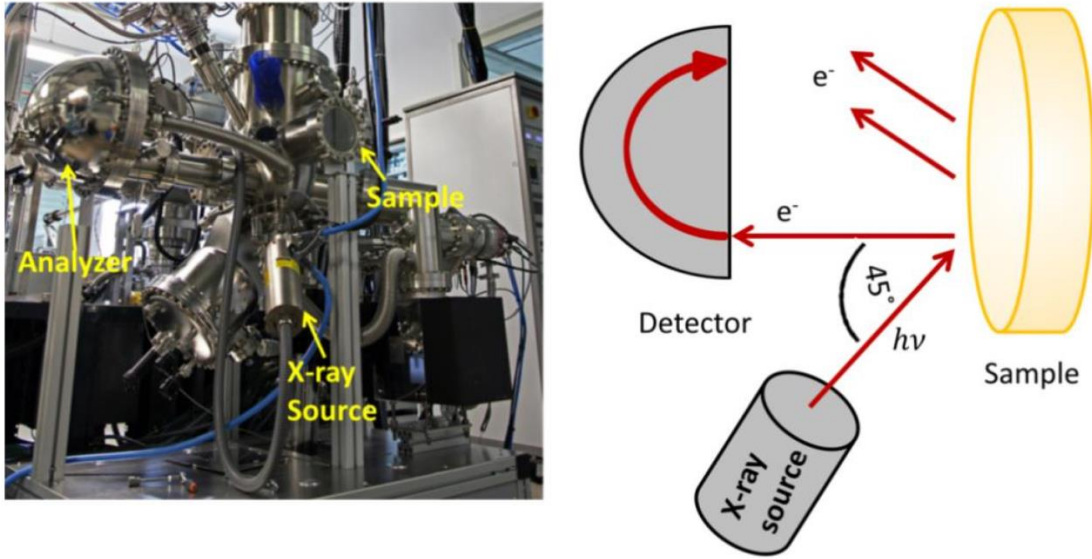


Fig. 3.7. Picture and sketch of the XPS setup mounted to the MBE cluster for in-situ measurements at IHP.

XPS technique is based on the principle of the photoelectric effect. An X-Ray photon of energy ' $h\nu$ ' will emit an electron of kinetic energy ' E_{kin} ' only if the energy of the photon ($h\nu$) is greater than the binding energy (E_B) of the electron. The emitted electron is known as a photo emitted electron; the process of electron emission is depicted in Fig. 3.8.

The kinetic energy of the photo-emitted electrons can be measured in the spectrometer and is given by [62,63]:

$$E_{kin} = h\nu - E_B - \Phi \quad 3.6$$

In the above equ. 3.6, E_B and E_{kin} denote the binding and kinetic energy of the photo emitted electrons, respectively. Φ is the spectrometer work function.

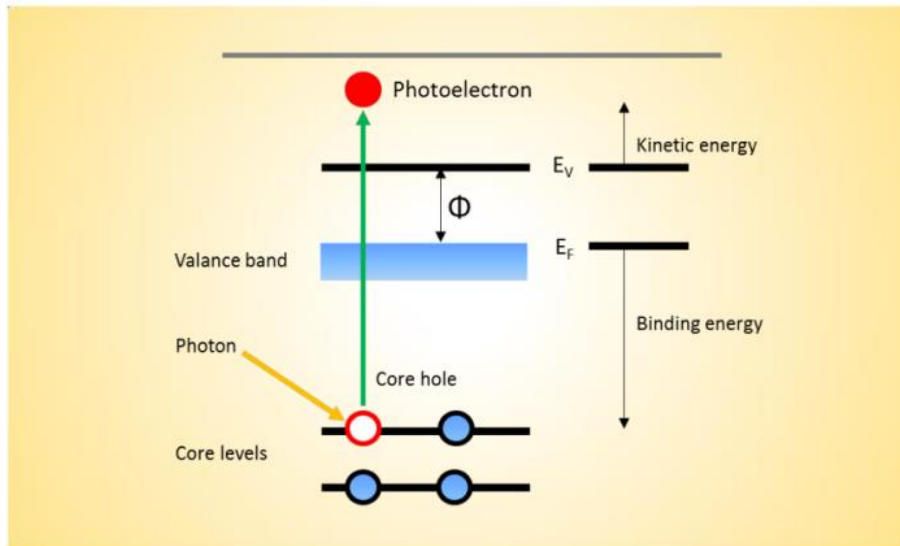


Fig. 3.8. A schematic diagram of the photoemission process.

3.4. Atomic force microscopy

Atomic force microscopy (AFM) illustrates the topography of the surface at the nanoscale. The advantages of AFM are that it (i) enables the investigation of any kind of samples, for example, conductive or semi-conductive surfaces, polymers, tissues, biological, etc., (ii) provides a high-resolution three-dimensional image of the surface, and (iii) operates in air. In this thesis work, AFM (Dimension 5000 SPM System with NanoScope IV Controller from Digital Instruments) in tapping mode was used (Fig. 3.9). The NanoScope V6.13 software was used to analyze the AFM images, and the information regarding surface morphology and roughness of the thin films were obtained.

This microscope uses a sharp tip to scan the surface of the specimen. The tip is usually made of silicon or silicon nitride and is integrated at the end of a flexible cantilever. Both the tip and the cantilever are mounted on a piezoelectric scanner, which can move precisely in three dimensions. As the tip moves across the surface, the forces between the tip and the sample deflect the cantilever according to Hook's law. This deflection is detected by a laser spot that reflects from the back of the cantilever into an array of four segmented

photodetectors. The recorded deflections of the cantilever are then used to generate a map of surface topography. As the tip can collide with the surface if it is scanned at a constant height, a feedback mechanism is therefore provided to adjust the sample-to-tip distance in order to maintain a constant force between the tip and the sample [64]. AFM can operate in three different modes such as contact, non-contact, and tapping mode, depending on the separation distance between the probe and surface. Tapping mode AFM was used in this work to determine the surface topography of the investigated samples. In tapping mode, the cantilever oscillates near its resonance frequency. During scanning, the tip slightly taps the sample's surface, thereby contacting the surface at the bottom of each oscillation, reducing the force exerted by the tip on the sample's surface. Hence, images of the surface are generated by maintaining constant oscillation amplitude.

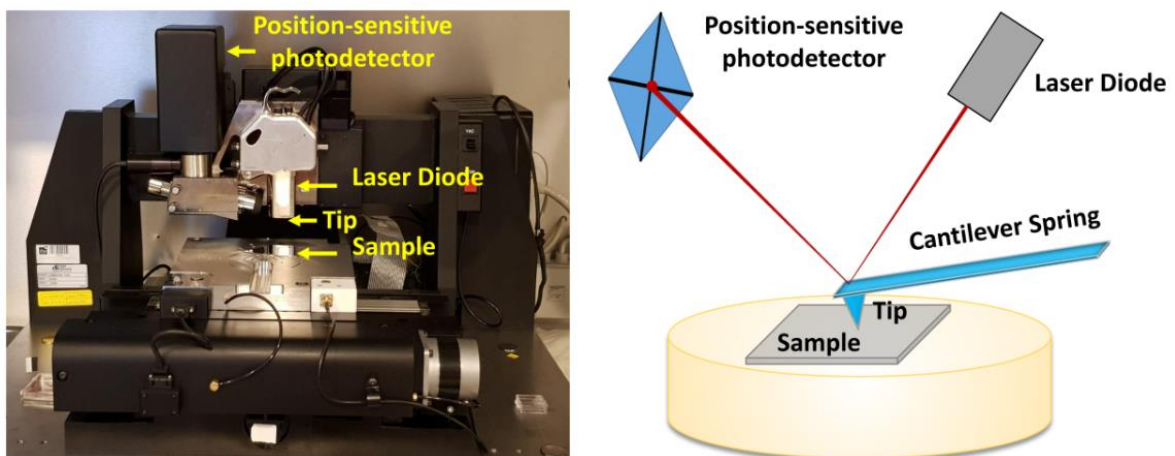


Fig. 3.9. Picture and a simplified sketch of the working principle of AFM.

3.5. Scanning electron microscopy

A ZEISS MERLIN GEMINI II SEM microscope (Fig. 3.10, left) was used in this work to investigate the surface topography of the samples. In SEM, incident electrons are focused into a fine probe that scans the surface of the specimen. The interactions between incident electrons and the sample lead to the emission of electrons and electromagnetic radiations,

including primary-back scattered electrons, secondary backscattered electrons, X-rays, etc. (Fig. 3.10, right). All these radiations can be detected using different kinds of detectors to generate an image. Among all the detection modes, the secondary electron detector is the most commonly used for imaging the surface topography [65,66].

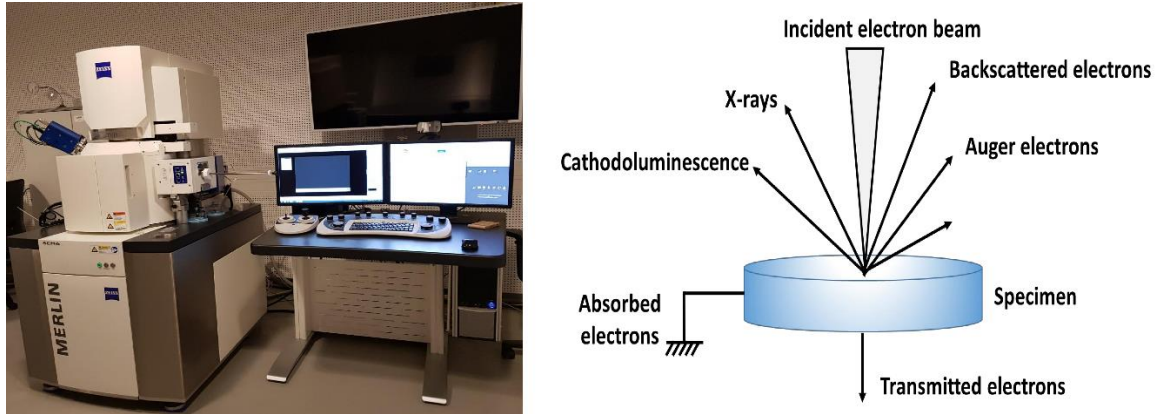


Fig. 3.10. Picture of the SEM system (left) and the generation of different signals due to interaction of incident electron beam with the specimen (right).

3.6. X-ray diffraction

X-ray Diffraction (XRD) is used to characterize the crystallographic orientations and various structural properties such as strain, grain size, epitaxy, phase composition, etc., of crystalline materials [67]. A Rigaku smart lab diffractometer with a Cu anode emitting the $K\alpha$ radiations ($\lambda = 1.54\text{\AA}$) was used in this PhD study in order to determine the different crystallographic orientations of Ni crystallites. Firstly, the samples were investigated in the so-called specular $\Theta-2\Theta$ configuration (Fig. 3.11). Then, the samples were also analyzed in rocking curve geometry in order to find the most preferred Ni orientations.

The principle behind the XRD is based on the constructive interference of monochromatic X-rays and crystalline samples. In a crystalline material, atoms are arranged in such a way that they form a series of parallel planes from one another at a distance (d), which depends on the nature of the material. When a monochromatic X-ray beam of wavelength ' λ ' hits

the specimen at an angle ' θ ', constructive interference occurs when Bragg's law is satisfied, which is mathematically expressed as:

$$n\lambda = 2d\sin\theta \quad 3.7$$

where $n = 1, 2, 3, \dots$, is the order of reflection, λ is the wavelength of the incident light, θ is the scattering angle, and d is the inter-planer spacing. Diffraction from different atomic planes generates a diffraction pattern, which provides information about the atomic arrangement within the crystal.

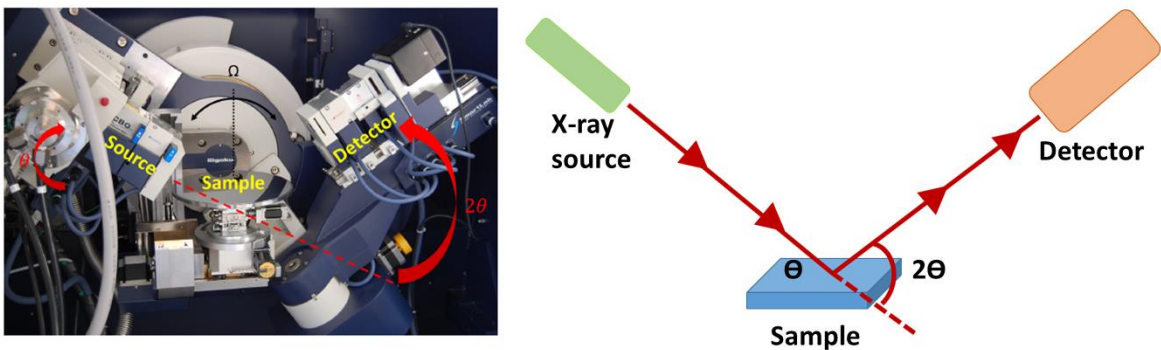


Fig. 3.11. Rigaku Smartlab diffractometer in specular configuration during θ - 2θ measurement (left) and illustration of θ - 2θ geometry (right).

3.7. Optical microscopy

With an optical microscope, the object is illuminated with white light from the condenser, and the reflected light forms a magnified view of the sample through an objective lens. Light passing through the objective lens can be diverted by a beam splitter either into an eyepiece for binocular observation or through a projection lens into a CCD camera. In this thesis work, optical microscopy was used to investigate the surfaces of the investigated samples (Fig. 3.12).

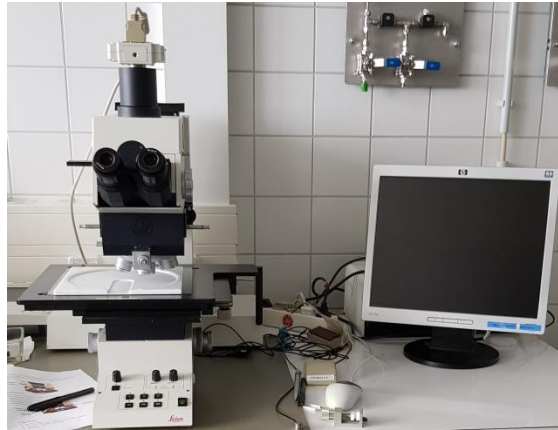


Fig. 3.12. Picture of the optical microscope.

3.8. Electron backscattering diffraction

Electron backscattering diffraction (EBSD) is a powerful tool that captures the diffraction pattern of electrons from crystalline materials. This diffraction pattern gives information regarding the (i) crystal orientations, (ii) type of grain boundaries, (iii) phase, (iv) texture, and (v) grain size distributions.

In this PhD work, the Ni grains distribution was studied by SEM (FEI Nova 600 Nanolab) equipped with an electron backscattering diffraction (EBSD) detector (Fig. 3.13). These measurements were performed at IKZ, Berlin.

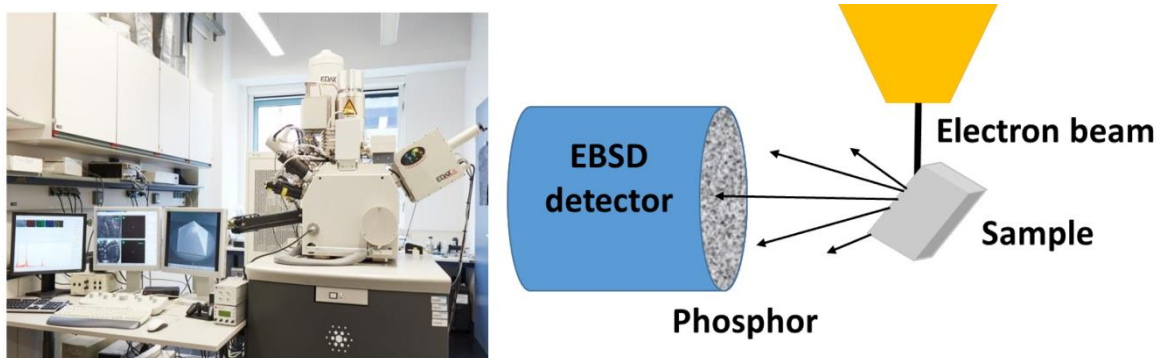


Fig. 3.13. Picture and simplified illustration of the working principle of the EBSD system.

The principle of this technique is based on the Kikuchi pattern of the diffracted electron beams. This pattern is obtained by focusing the beam of electrons on a crystalline sample.

The sample is tilted about 70° relative to the incident light, which allows more electrons to be scattered and to escape towards the detector. Electrons from the incident beam are diffracted on the crystallographic planes of the specimen. The diffracted electrons that interfere constructively generate a pattern consisting of intersecting bands known as Kikuchi bands. This diffraction pattern is obtained on a phosphor screen, which is placed in front of the EBSD camera. In the pattern, the bands represent the reflecting planes in the diffracting crystal volume. Hence, the arrangement of the bands is the function of the orientation of the diffracting crystal because (i) the pattern reflects the symmetry of the crystal (ii) the spacing of the atoms in the crystallographic planes is directly related to the width and the intensity of the bands, and (iii) the angle between crystallographic planes are directly related to the angles between the bands [68].

3.9. Reactive ion etching

Reactive ion etching (RIE) is a type of dry etching that uses chemically reactive plasma to remove materials deposited on the substrates. The plasma is generated by applying RF (radio frequency) electromagnetic field under low pressure (vacuum). High energy ions from plasma attack the substrate's surface and react with it [69]. The magnetically enhanced RIE tool (Applied Materials, P5000), which was used in this PhD work for the removal of thin graphene films deposited on Ni, is shown in Fig. 3.14 (left). The right panel of Fig. 3.14 also shows a diagram of the RIE setup. As can be seen, RIE is composed of two electrodes (1 and 4) that create an electric field (3) meant to accelerate ions (2) toward the surface of the samples (5).

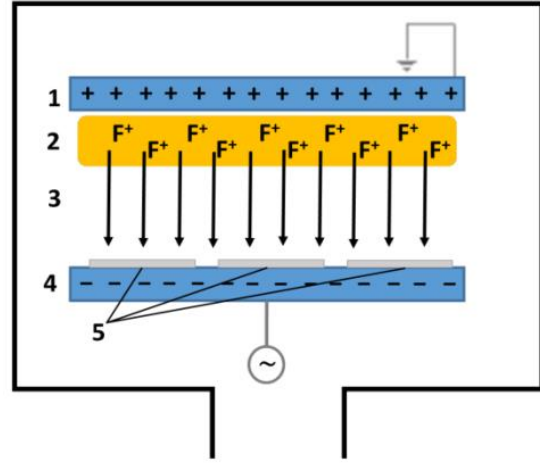


Fig. 3.14. Picture (left) and diagram of RIE set up [right, recreated from Ref. 69].

3.10. *Spectral ellipsometry*

Ellipsometry is a non-destructive technique that is used to determine the layer thickness and optical constants in addition to the crystallinity, roughness, composition, doping concentration, and other material properties. Thickness determinations ranging from a few angstroms to tens of microns are possible for single layers or complex multilayer stacks. This technique consists of measuring the change in the polarization state of a beam of light upon reflection from the specimen [70]. The exact nature of the polarization change depends on the specimen's properties (thickness and refractive index). Hence, by analyzing and detecting the changes in the polarization and the intensity of the light, optical constants and thickness of the film are determined. The ellipsometry tool (KLAfx200) used during this PhD work to determine the thickness of the graphene film over the entire Ge wafer is displayed in Fig. 3.15.

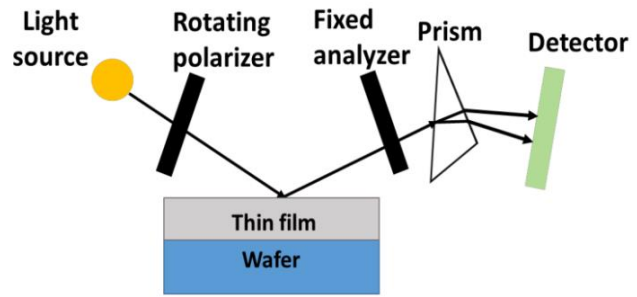


Fig. 3.15. Picture and schematic illustration of the working principle of spectral ellipsometry tool.

3.11. Time-of-flight secondary ion mass spectrometry

In this technique, a finely focused ion beam is used to excite the surface of the sample, which causes the emission of secondary ions and ion clusters from the sample's surface. The mass of the emitted ions is measured with the help of a time-of-flight analyzer. From the mass and intensity of the SIMS peaks, the identity of elements or molecular fragments can be identified. ToF-SIMS (ION-TOF-5) tool, which was used during this study for the investigation of the contamination levels in the grown, as well as transferred graphene, is shown in Fig. 3.16.

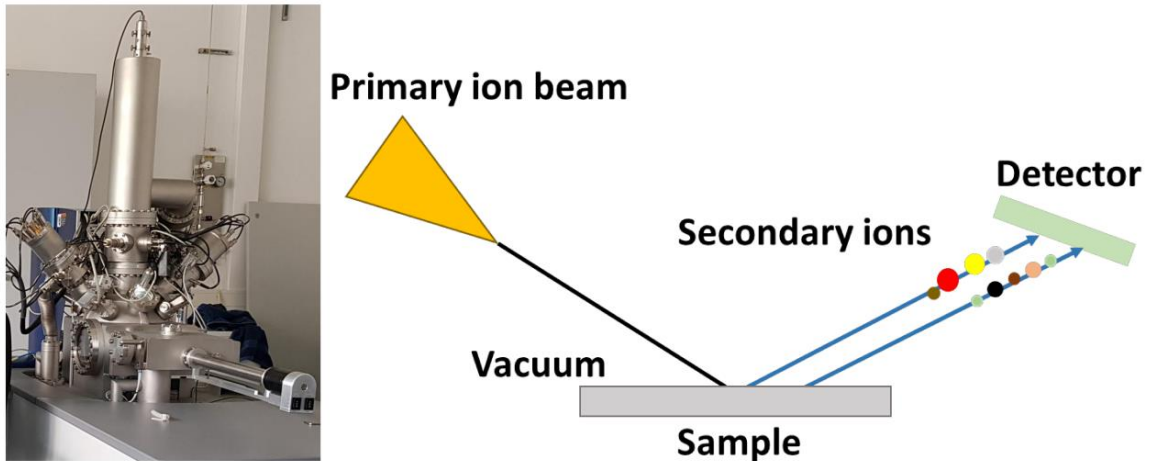


Fig. 3.16. Picture and simplified illustration of the working principle of the ToF-SIMS tool.

3.12. *Electrical measurements*

The electric behavior (especially high electric mobility and conductivity) is one of the most important features of graphene. Therefore, electrical characterization is a critical way to evaluate graphene samples.

Hall effect

Hall Effect is the production of a voltage difference across an electric conductor due to the separation of electric charges forming current perpendicular to the applied magnetic field and the induced electric field.

The Hall measurements are usually performed by Van der Pauw geometry. Van der Pauw method allows determining the resistivity, carrier concentration, and mobility of any arbitrary shaped, flat sample if the following conditions are met:

- The contacts are made on the corners of the sample
- The contacts are very small (point-like)
- The thickness of the sample is homogeneous
- The surface of the sample is simply connected, i.e., it does not contain any holes

After the sample's preparation, the Hall voltage and resistivity can be measured in different configurations. For resistivity measurements, the current is entered through contact A and leaves through contact B, while the voltage drop across the other two contacts (C and D) is measured (Fig. 3.17, right). Resistivity can be written in the following form:

$$\rho = \frac{\pi d}{\ln 2} \cdot \frac{(R_{AB,CD} + R_{BC,DA})}{2} \cdot f \quad 3.8$$

Where f is the correction factor and the value is tabulated for any value of resistance ratio $\frac{R_{AB,CD}}{R_{BC,DA}}$.

For the Hall voltage measurements, the sample is placed in magnetic field B , the current is generated through the opposite contacts (A and C), and the Hall voltage is measured across the remaining contacts (B and D). Mathematically, the Hall voltage is written as:

$$V_H = \frac{IB}{nte} \quad 3.9$$

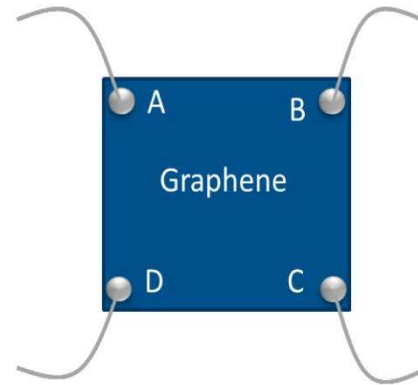


Fig. 3.17. A picture of the Lakeshore 7600 Hall system (left). A schematic illustration of Van der Pauw Hall measurement geometry (right).

Where I is the current across the conductor, B is the magnetic field, t is the thickness of the conductor, n is the charge carrier density, and e is the elementary charge.

Based on the polarity of the Hall voltage, it is possible to determine the type of material the sample is made of. For instance, if the sign of Hall voltage is negative, the material is N-type, and if it is positive, the material is P-type. The charge density and the mobility of the material can be calculated using the following formulas:

$$n = \frac{IB}{et|V_H|} \quad 3.10$$

$$\mu = \frac{|R_H|}{\rho} \quad 3.11$$

where R_H is known as the Hall coefficient and is written as:

$$R_H = \frac{V_H t}{IB} = \frac{1}{ne} \quad 3.12$$

In this thesis, the Lakeshore 7600 Hall system (Fig. 3.17, left) was used to find the electrical mobility and sheet resistance of the graphene grown on Ge.

Current-Voltage measurements (I-V)

A current-voltage characteristic (typically represented as a graph) is a relationship between the current through a device, circuit, or material and the corresponding potential difference across it. It is a fundamental electric measurement and a primary way to determine the behavior of a device in an electronic circuit. These characteristics are known as I-V curves, which are used to characterize semiconductors, solar cells, nanotubes, graphene, photovoltaic cell, etc.

In this Ph.D. work, the I-V measurements were performed to determine the graphene-induced conduction between the Ni pads. The system used to perform these measurements is shown in Fig. 3.18 (left). Also, a simplified schematic of the I-V test structure is shown in the right panel of Fig. 3.18.

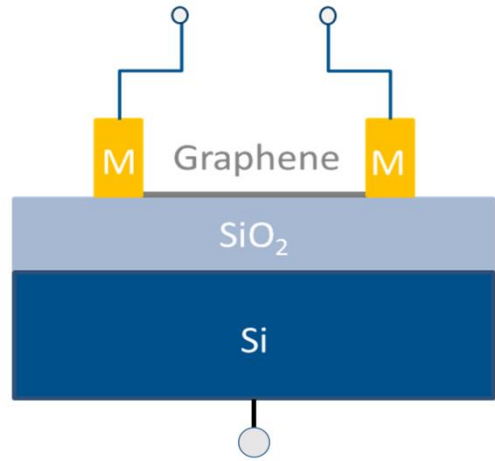


Fig. 3.18. A picture of the system used to extract the I-V characteristics of graphene at IHP (left). The simplified model of the I-V measurement circuit (right).

PART III

RESULTS AND DISCUSSIONS

CHAPTER 4

4. RESULTS & DISCUSSIONS

In this PhD work, graphene growth on polycrystalline Ni and Ge substrates was performed by the thermal CVD method. The obtained results are discussed in this chapter, which is divided into four sections. The growth of graphene on polycrystalline Ni is discussed in section 4.1. The main motivation of this work was to use thin Ni films and optimize their surface morphologies so that the grain boundaries are reduced or, in other words, Ni(111) grain sizes are increased so that the thickness uniformity of graphene can be controlled. Hence, the impact of different annealing conditions (i.e., hydrogen and vacuum) on the surface morphology of Ni and, therefore, on graphene growth were studied.

The Ni-assisted graphene synthesis method was further used to explore the possibility of graphene growth on dielectric substrates. In order to achieve this, two different routes, such as graphene growth underneath the Ni films and between the Ni bars, were explored. Results are discussed in sub-section 4.1.1.

The growth of graphene on (001) and (110) oriented Ge substrates is described in sections 4.2 and 4.3, respectively. The purpose of this PhD work was not only to grow large (8-inch) graphene films on Ge substrates but also to provide explanations on the faceted and non-faceted surface morphology of the underlying Ge orientations.

Lastly, the oxidation behaviors of graphene-covered Ge(001) and Ge(110) systems are provided (section 4.4). In order to check the oxidation of Ge films underneath graphene, both the graphene/Ge systems were kept in the open air for more than seven months, and their oxidation behaviors were investigated and compared. In addition, influences of the interfacial oxygen on the properties of graphene were also checked.

4.1. Chemical vapor deposition of graphene on polycrystalline nickel

Deposition of the Ni films for graphene growth

The first task of this work was focused on defining the suitable thickness of Ni films that can remain stable at the graphene growth temperature. For this purpose, Ni films of varying thicknesses (i.e., 50, 100, and 200nm) were deposited by a DC magnetron sputtering method on 100nm thick thermally grown SiO₂ layers deposited on Si substrates. The deposition conditions of Ni are listed in table 4.1.

Table.4.1. Deposition conditions of Ni.

Deposition temperature (°C)	Gas flow (sccm)	Carrier gas	Deposition time (sec)	Pressure (mTorr)	Power (Watt)
Room temp	55	Argon	120	4	750

Furthermore, a sketch of the final cross-sectional view of the sputtered Ni films on SiO₂/Si substrates is illustrated in Fig. 4.1.

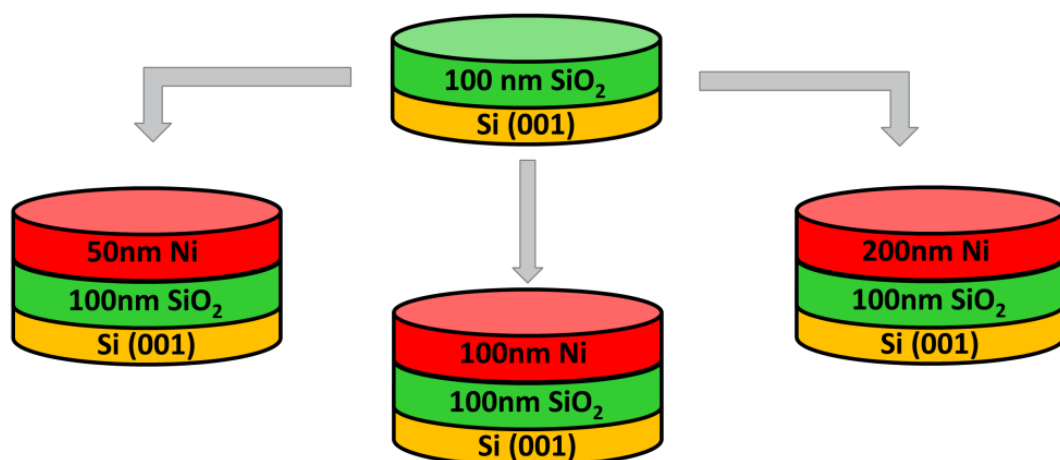


Fig. 4.1. Cross-sectional schematic view of the 50, 100, and 200nm Ni films deposited on SiO₂/Si substrates.

Selection of a thermally stable thickness of the Ni films

After the deposition of Ni, the next step was to determine a thermally stable thickness of the Ni films. Therefore, I annealed the Ni films in the temperature range of 925–1025°C. Optical images taken after the annealing treatments are depicted in Fig. 4.2. As seen, 50 and 100nm Ni samples were not stable and de-wetted at 925°C and 950°C, respectively (Figs. 4.2a and b). It is known that thermal fluctuations at high temperatures increase the surface energy of the system. As the system tries to minimize this excessive energy, continuous film decomposes into arrays of isolated islands (i.e., hillocks formation); this process is known as de-wetting.

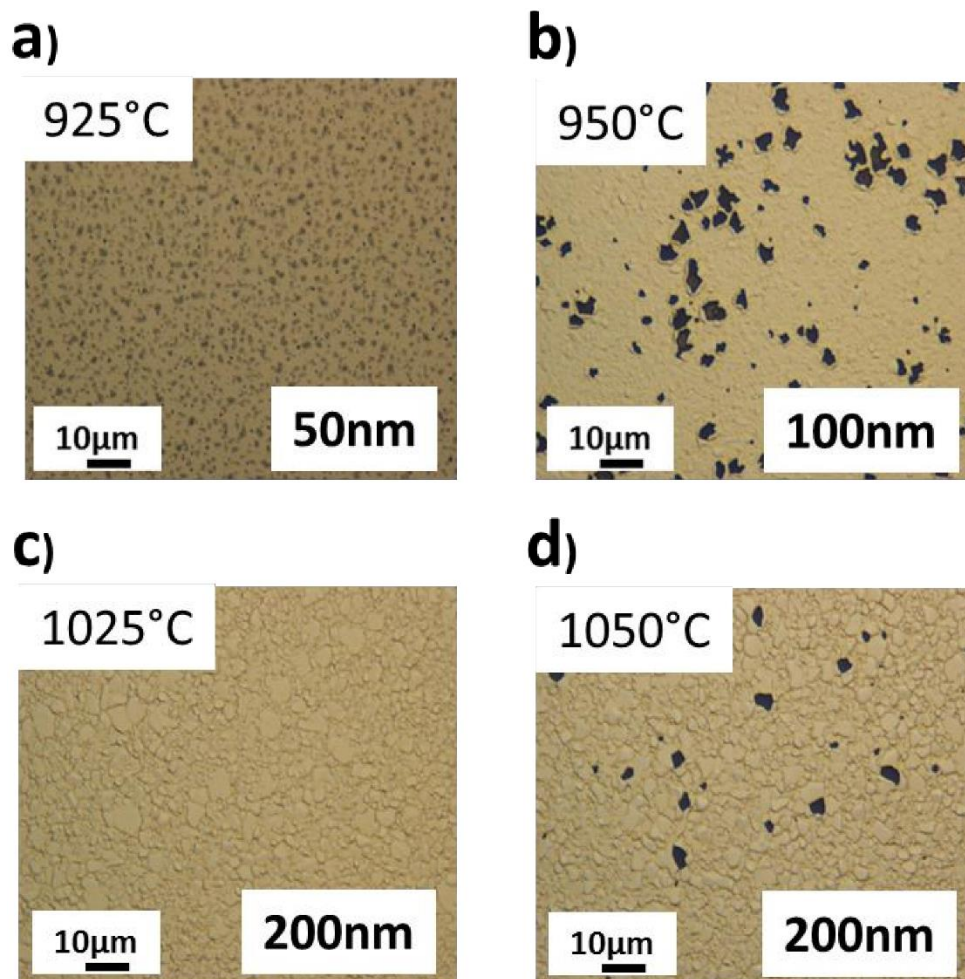


Fig. 4.2. Optical images of the (a) 50nm, (b) 100nm, and (c–d) 200nm Ni films annealed at 925°C, 950°C, 1025°C, and 1050°C, respectively.

On the contrary, 200nm Ni films remained stable up to 1025°C (Fig. 4.2c). However, they also start to de-wet when the temperature was increased to 1050°C (Fig. 4.2d). Based on these observations, I selected 200nm thick Ni films to grow graphene in this PhD work.

Surface pretreatments of 200nm Ni films

Before graphene growth, the surfaces of selected 200nm Ni films were pre-treated. The surface pre-treatments of Ni were done by annealing them in the CVD chamber. Additionally, I investigated the impacts of different annealing conditions (i.e., hydrogen and vacuum) on the surface morphology of the Ni films. Hence, two annealing series in the temperature range of 925-1025°C were performed, based on the ambient conditions. The protocols for the pretreatment experiments are listed in table 4.2.

Table.4.2. Conditions for annealing Ni films before CVD of graphene.

Ambient conditions	Annealing Temperature (°C)	Annealing time (min)
Hydrogen	925-1025	10
Vacuum	925-1025	10

Optical images taken after annealing the Ni films in hydrogen and vacuum are presented in Fig. 4.3. It can be seen that both the annealing conditions have impacted the surface morphology of the Ni films.

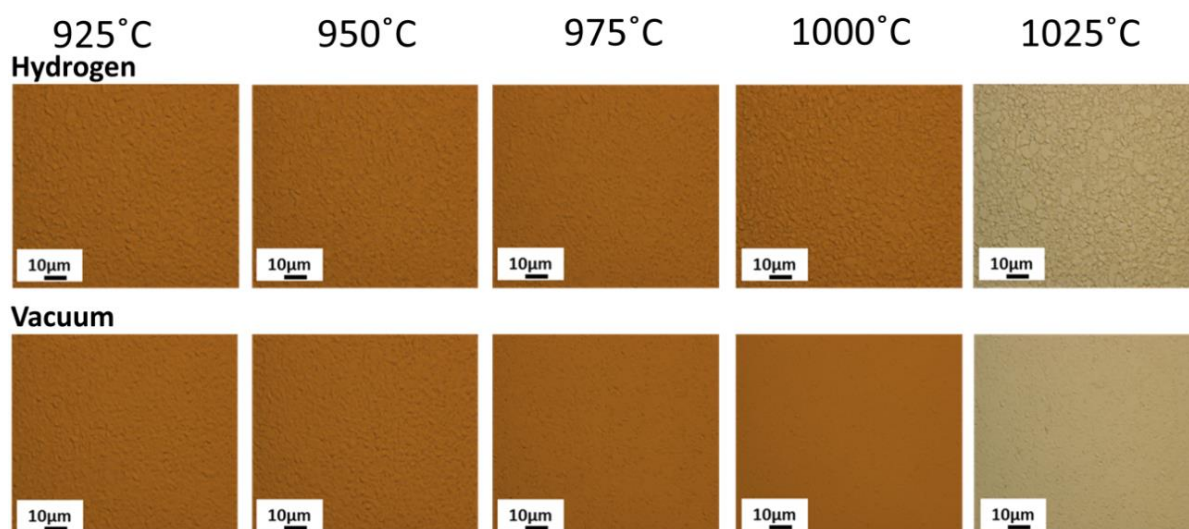


Fig. 4.3. Optical images of the Ni films annealed in hydrogen (top row) and vacuum (bottom row) in the temperature range of 925 to 1025°C [images taken after annealing at 1025°C are adopted from Ref. 71].

Influence of pretreatment conditions on the crystallinity and morphology of Ni films

The crystal structure of Ni films was examined by the XRD technique. The diffraction patterns for as-deposited and annealed Ni films (hydrogen/vacuum) were recorded by specular ω - 2θ scans in the angular range of $2\theta = 40^\circ$ – 55° . Figs. 4.4a and b show the XRD scans of as-deposited Ni (black lines). One can see a most intense reflection at 44.52° assigned to Ni(111) orientation and a weak Ni(200) peak at 51.87° , corresponding to Ni crystallites with (100) orientation, indicating poly-crystallinity of the as-deposited samples. Figs. 4.4a and b also show the XRD curves for the Ni films annealed in hydrogen and vacuum at different temperatures (925°C (dark yellow), 950°C (red), 975°C (green), 1000°C (blue), and 1025°C (magenta)).

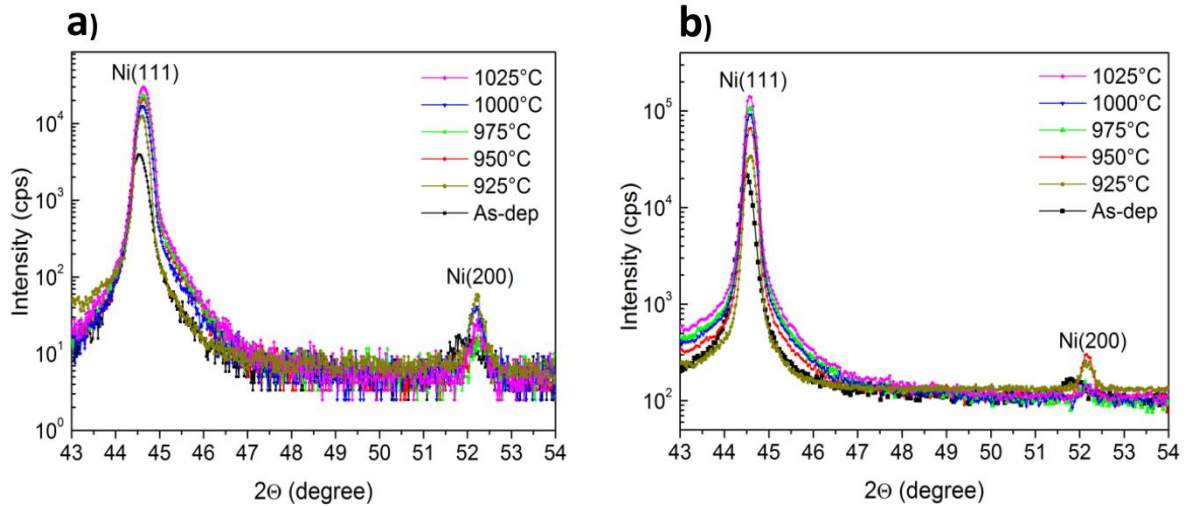


Fig. 4.4. XRD ω – 2θ scans of as-deposited (black lines) and annealed Ni films in (a) hydrogen and (b) vacuum. The dark yellow, red, green, blue, and magenta lines show the XRD scans for the films annealed at 925, 950, 975, 1000, and 1025°C, respectively.

In the XRD scans, one can notice that the polycrystalline nature of Ni is maintained even after annealing as both the Ni(111) and Ni(200) reflections are still present. However, Ni(111) and Ni(200) peaks are slightly shifted to higher angles, which could be due to the different thermal expansion coefficients of Ni ($14 \times 10^{-6} \text{ K}^{-1}$) and the underlying Si substrate ($4 \times 10^{-6} \text{ K}^{-1}$) [72]. As no significant differences were observed by XRD ω – 2θ scans for the samples annealed in hydrogen and vacuum conditions, therefore, a detailed analysis of Ni(111) peak was performed by conducting ω scans. The ω scan is used to determine the mosaic spread in the film appearing due to randomly oriented crystallites. In these experiments, the sample was tilted while the detector was fixed at the center of diffraction peak Ni(111). From the width or full width at half maxima (FWHM) of the Ni(111) peak, the mosaicity in the films was determined. The obtained values of FWHM were plotted as a function of annealing temperatures, as shown in Fig. 4.5. This plot shows that the FWHM of Ni(111) peak was 9.63° (as-deposited Ni), however, the FWHM has been reduced to 5.43° and 5.89° after annealing at 1025°C in hydrogen and vacuum, respectively. This means that

the mosaicity of Ni(111) planes was reduced in both annealing conditions. However, the FWHM was lower in the case of hydrogen annealing, indicating that the degree of order was higher.

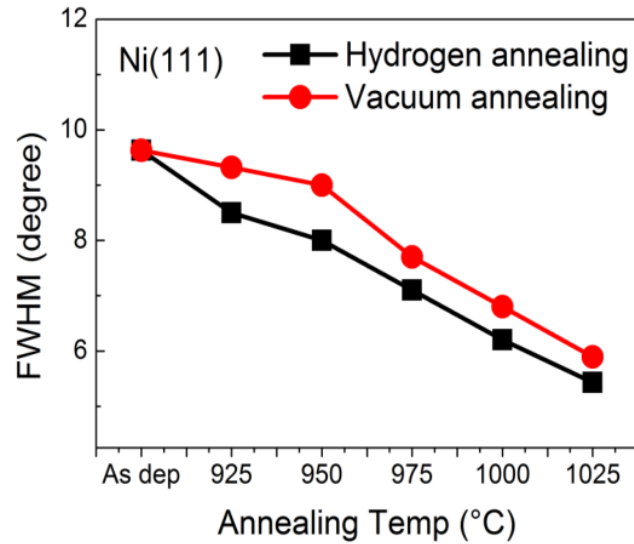


Fig. 4.5. FWHM of Ni(111) reflection obtained from omega scans as a function of annealing temperatures.

In addition to crystal quality, the surface morphology of as-deposited and annealed Ni films was also investigated by SEM. The images taken with HE-SE2 detector (high-efficiency secondary electron detector; used to examine surface topography) after annealing the Ni films in hydrogen and vacuum are provided in Figs. 4.6a–e and 4.6k–o, respectively. It can be observed that Ni grain sizes and shapes are non-uniform. This non-uniformity is attributed to the grain growth phenomenon in which the lateral grain size exceeds the film thickness. During this grain growth mechanism, faster-growing grains dominate the slower ones. This process continues until all un-favored grains shrink, leading to texture development in thin films [73,74]. In addition, it was noticed that the surface roughness of the Ni films also increased as a result of grain growth. The surface roughness (R_q) was

determined by scanning $5 \times 5 \mu\text{m}^2$ areas of the films annealed in hydrogen (Figs. 4.6f–j) and vacuum (Figs. 4.6p–t).

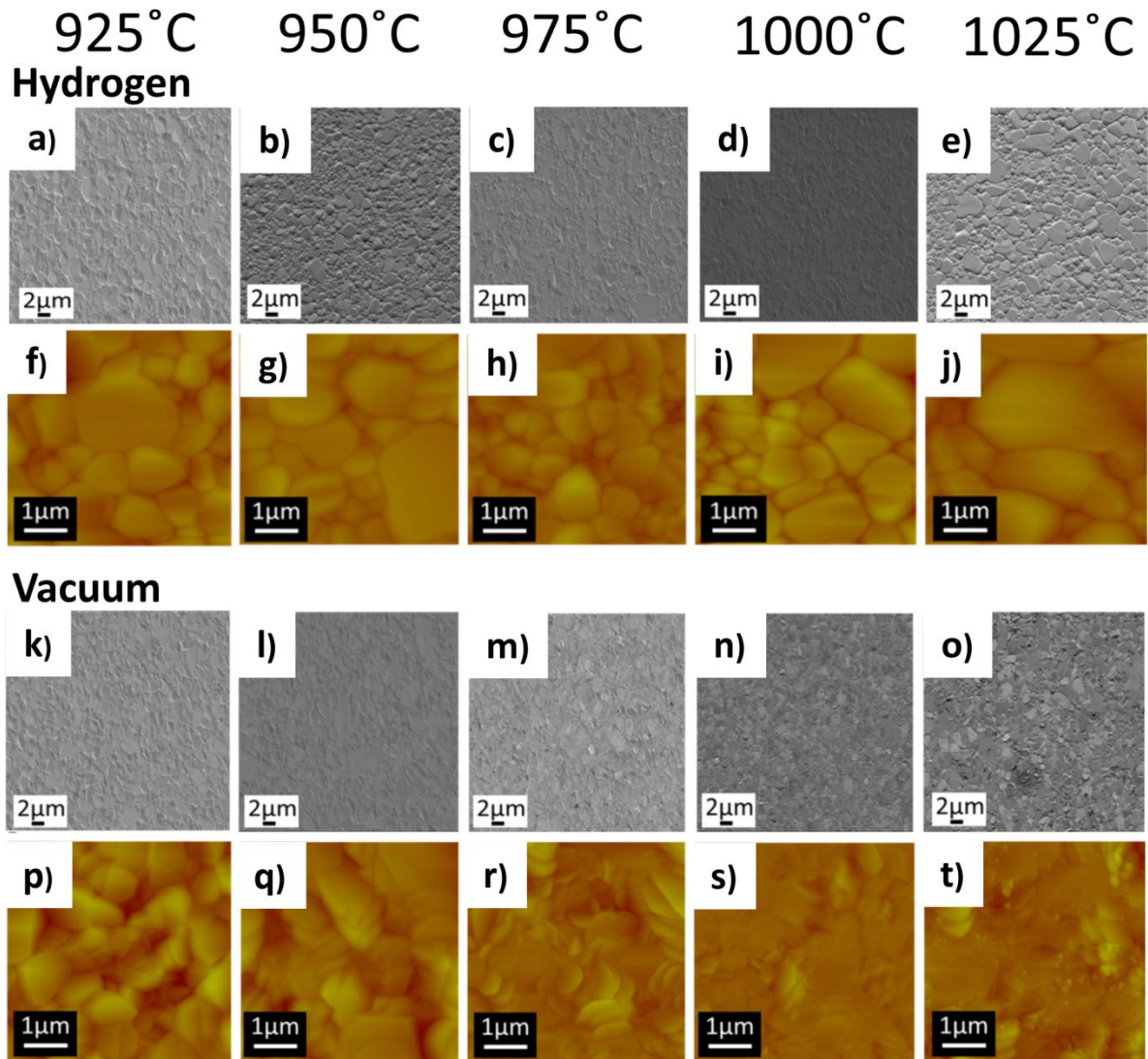


Fig. 4.6. (a–e) SEM and (f–j) AFM micrographs for the Films annealed in hydrogen in the temperature range of 925 to 1025°C. (k–o) SEM and (p–t) AFM micrographs for the Films annealed in vacuum in the temperature range of 925 to 1025°C [images taken after annealing at 1025°C are adopted from Ref. 71].

A plot of surface roughness versus annealing temperatures is shown in Fig. 4.7. As seen, the R_q values increased from 1.6nm (as-deposited Ni) to $\sim 28\text{nm}$ (after annealing in hydrogen) and $\sim 10\text{nm}$ (after annealing in vacuum). It should be noted that the surface roughness

measured in this PhD work for the Ni films annealed in hydrogen was lower than the literature report [43]. The authors measured high surface roughness (36.3nm) of 500nm thick Ni films after 15mins annealing (900°C) under 600sccm H₂ pressure [43]. It is assumed that the lower surface roughness of thin Ni films in this study could be due to their less deep GBs grooves than the thick films.

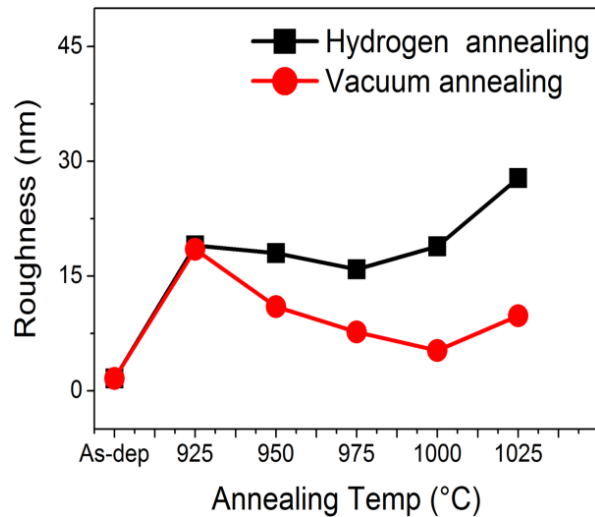


Fig. 4.7. The surface roughness of the Ni films annealed in hydrogen and vacuum as a function of annealing temperatures.

Besides, one can observe that Ni grain sizes have also increased with increasing temperatures. Larger grains were recorded at higher temperatures (1025°C) (Fig. 4.6). The Ni grain size distributions were investigated by EBSD (The EBSD measurements were performed by Dr. Martin Albrecht at IKZ, Berlin). The 30 × 80μm² EBSD orientation maps of Ni films annealed in hydrogen and vacuum are depicted in Figs. 4.8a and b, respectively. The RGB coloring scheme of the inverse pole figure is also provided in Fig. 4.8. The maximum reflections from blue color in the orientation maps showed that <111> was the dominating orientation. However, a small proportion of other orientations, such as <001> and <101>, were still present.

Moreover, the plots in Figs. 4.8c and d present a variation in the in-plane diameter of Ni grains under both conditions. The grain diameters were measured within the range of ~ 0.3 – $6\mu\text{m}$ for the films annealed in hydrogen (Fig. 4.8c). In contrast, the grain sizes were recorded from ~ 0.3 to $3\mu\text{m}$ for the films annealed in vacuum (Fig. 4.8d). As the grain sizes below $0.6\mu\text{m}$ could not be indexed appropriately, therefore, they have been removed. Indeed, the problem of unindexed or mis-indexed pixels in EBSD maps has already been reported [75a].

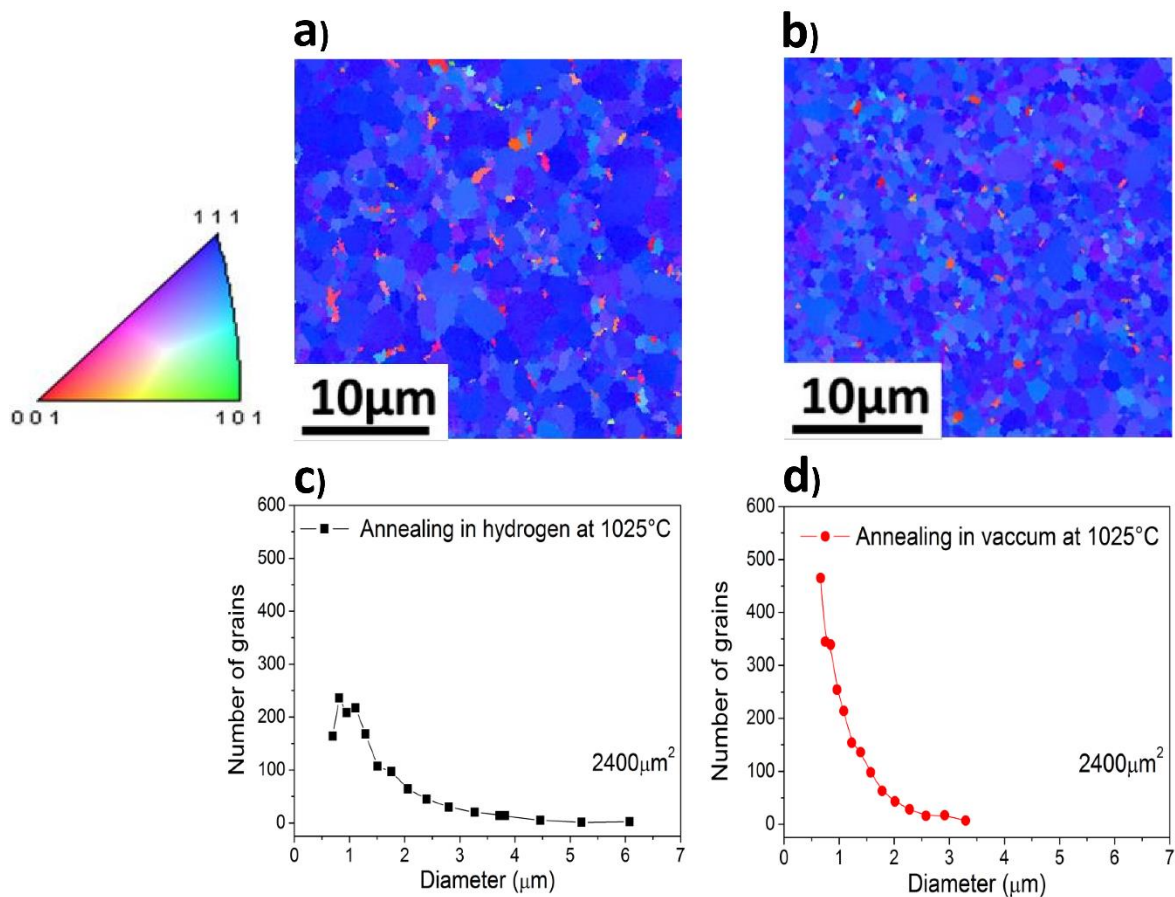


Fig. 4.8. EBSD analysis: color scheme, orientation maps, and grain distributions for films annealed in hydrogen (a and c) and vacuum (b and d) at 1025°C [adopted from Ref. 71].

The Ni grain distributions were further statistically analyzed as a function of annealing temperatures under both annealing conditions. For that reason, $20 \times 20\mu\text{m}^2$ surface areas of annealed Ni films were scanned by SEM. These SEM images were analyzed using ImageJ

software [75b], “3D variance” followed by watershed was used to analyze them; artifacts in the images were removed manually. The Ni grain diameters (d) were calculated by converting the obtained areas from every image by using the formula ($d^2 = 4A/\pi$). After taking the logarithms of the diameters, histograms were generated (Figs. 4.9a and b). The histograms were fitted with a log-normal distribution function:

$$f(d) = \frac{1}{\sigma d \sqrt{2\pi}} \exp \left[- \left(\frac{\ln d - \ln d_0}{\sqrt{2}\sigma} \right)^2 \right] \quad 4.1$$

Where d_0 and σ represent the average grain diameter and lognormal standard deviation, respectively.

It can be seen in Figs. 4.9c and d that the average grain sizes and FWHM of grain distributions increased with increasing temperatures. At maximum temperature (1025°C), the average grain diameters were $\sim 0.86\mu\text{m}$ (hydrogen ambient) and $\sim 0.76\mu\text{m}$ (vacuum ambient). Similarly, FWHM of grain distributions obtained different values for hydrogen ($\sim 0.52\mu\text{m}$) and vacuum ($\sim 0.53\mu\text{m}$) annealed samples. According to EBSD and SEM results, larger grains were recorded for the films annealed in hydrogen in comparison to the films annealed in vacuum.

The difference in Ni grain sizes as a function of different annealing ambient could be attributed to hydrogen dissolution in Ni. It is well known that hydrogen occupies the host metal’s interstitial sites during annealing and generates stresses in the film [72b,76–78]. The dissolved hydrogen displaces the metal atoms from their original positions; consequently, the grain size increases. Therefore, it is assumed that stress induced by interstitial hydrogen could be the cause of larger Ni grains ($\sim 6\mu\text{m}$) for the films annealed in hydrogen. This assumption is in agreement with the literature study where authors obtained wide and flat Ni(111) nanostructures because of the dissolution of hydrogen [77]. In another literature report, it is stated that the presence of interstitial hydrogen induces additional stresses in

the Ni films, which could lead to the volume expansion of the Ni grains [72b]. As Ni films annealed in vacuum were not under the influence of hydrogen, grain growth was affected by the abnormal grain growth mechanism only, and grain sizes increased up to $3\mu\text{m}$.

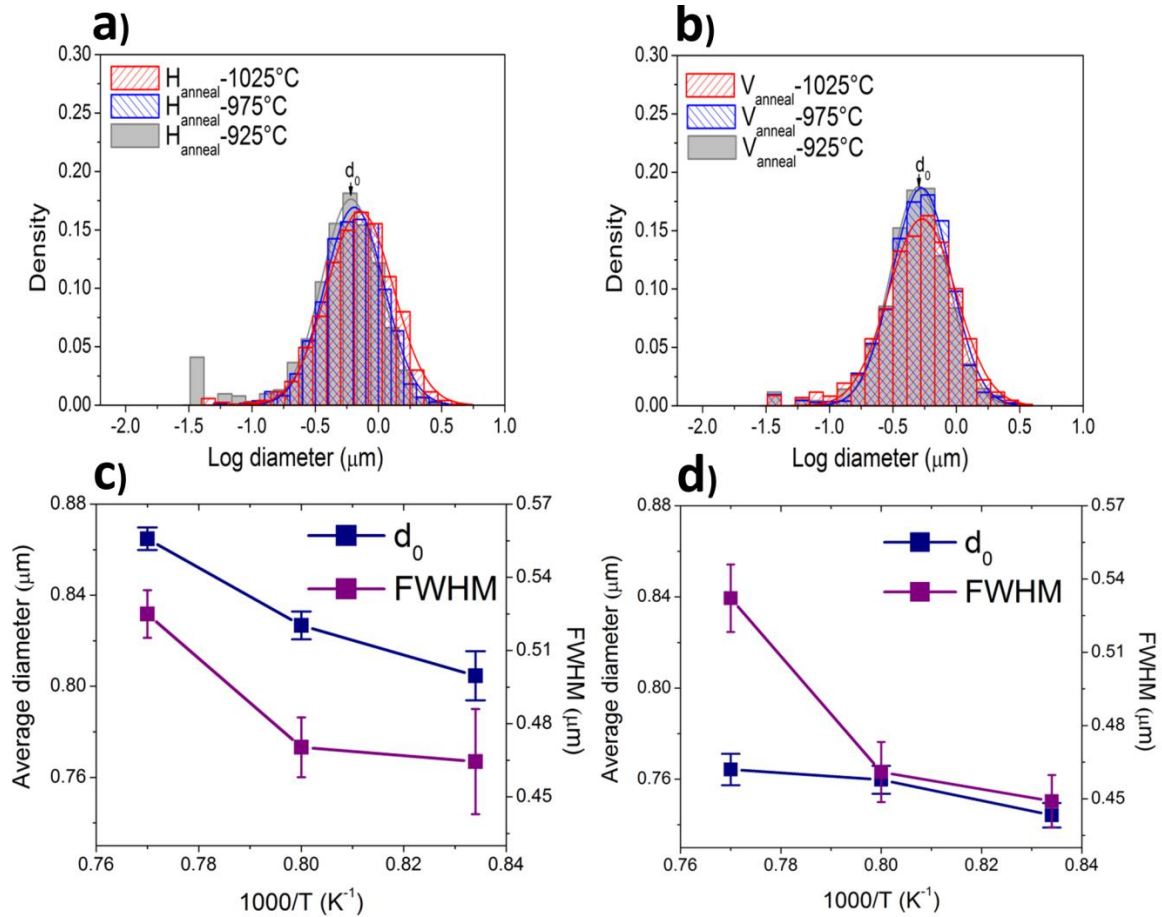


Fig. 4.9. SEM analysis of grain size distribution for Ni films annealed in (a) hydrogen and (b) vacuum. (c–d) Average grain diameter and average FWHM of grain size distribution in hydrogen and vacuum, respectively.

In comparison with the reports in the literature, different sizes of Ni grains were achieved for Ni films of different thicknesses. For instance, the grain sizes were recorded within the range of 1 to $20\mu\text{m}$ for thick Ni films (500 to 550nm) [44,72a,79]. In the case of Ni foils ($25\mu\text{m}$), on the other hand, larger grains ($\geq 50\mu\text{m}$) were reported [80]. Though larger grains can be obtained using thick Ni, much deeper GBs grooves and, therefore, higher surface

roughness are the disadvantages of thick Ni. Compared to thick Ni, the grain sizes were much smaller for thinner Ni films; for example, grain sizes from 1 to 4 μm were reported for 300nm thin Ni film [81–84]. A few literature reports are available on grain sizes for thin $\leq 200\text{nm}$ Ni films (as used in this PhD work) [85–87]. In these reports, the authors observed smaller Ni grains (from 150nm to 1 μm) and attributed them to the simultaneous growth of Ni grains and carbon diffusion during the annealing step [86,87]. These smaller grains caused the thickness non-uniformity of graphene, which shows the importance of pre-annealed Ni films. In this PhD study, the annealing of Ni films under different conditions before graphene synthesis led to larger grains (up to 6 microns).

Influence of pretreatment conditions on Ni surface cleaning

Prior to graphene growth, the elemental composition of Ni films was investigated by XPS. The XPS results are summarized in Fig. 4.10. The C1s spectrum (black line) of the as-deposited Ni is comprised of three peaks corresponding to C–H ($\sim 285.0\text{eV}$), C–O ($\sim 286.5\text{eV}$), and C=O ($\sim 288.9\text{eV}$), as demonstrated in Fig. 4.10a. The Ni2p spectrum of as-deposited Ni (black line) is presented in Fig. 4.10b. The deconvolution of the spectrum reveals three different oxidation states of Ni .i.e. Ni 0 ($\sim 852.6\text{eV}$), Ni $^{+2}$ ($\sim 854.1\text{eV}$), and Ni $^{+3}$ ($\sim 856.1\text{eV}$) corresponding to metallic Nickel, NiO, and Ni $_2\text{O}_3$, respectively [88]. In addition, some satellite (shakeup) features at a few eV above the main peak can also be seen in the spectrum. Shake-up satellites appear when the outgoing electron interacts with the valence electron and excites it to a higher energy level. As a result, the energy of the photo-emitted electron is reduced, and a satellite peak appears a few eV above the main peak in the binding energy scale [62]. The O1s spectrum of the as-deposited Ni is also shown in panel c in Fig. 4.10 (black line). The spectrum is fitted to two main components at binding energies of $\sim 529.6\text{eV}$ and $\sim 531.7\text{eV}$. These peaks are assigned to NiO and Ni $_2\text{O}_3$, respectively [88,89].

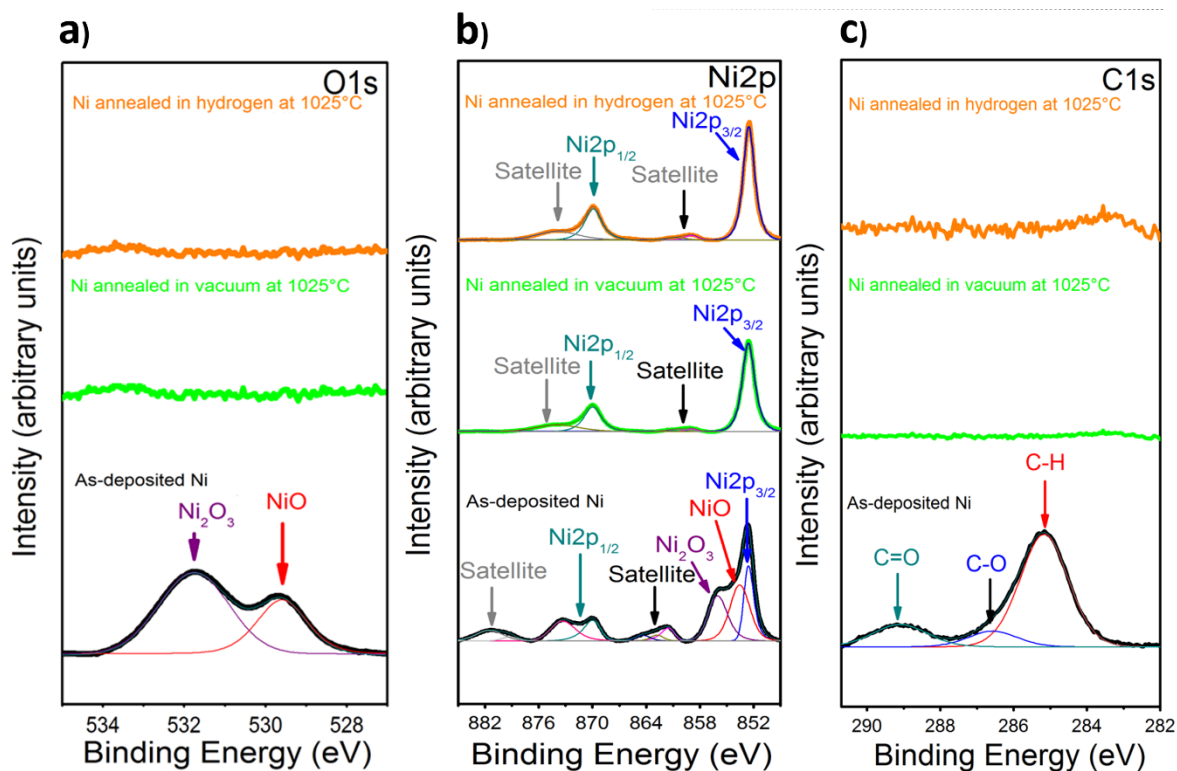


Fig. 4.10. XPS analysis: (a) C1s, (b) Ni2p, and (c) O1s spectra of Ni films. As-deposited Ni films, Ni films annealed in vacuum and hydrogen are represented by black, green, and orange lines, respectively.

These XPS results showed that the as-deposited Ni films became contaminated when exposed to air; however, these contaminants have been removed after annealing the Ni films in both ambient conditions (Fig. 4.10a–c, green and orange lines).

At this stage, all the Ni films contained larger grains and have clean surfaces; therefore, they were ready for graphene growth.

Graphene growth

In order to grow graphene, the Ni films annealed in hydrogen and vacuum were exposed to ethylene and hydrogen. The graphene growth conditions are listed in table 4.3. Besides, the growth process of graphene on polycrystalline Ni is also illustrated in Fig. 4.11.

Table.4.3. Conditions for graphene deposition.

Growth temperature (°C)	carbon source	Carrier gas	Deposition time (min)
925	ethylene	hydrogen	5

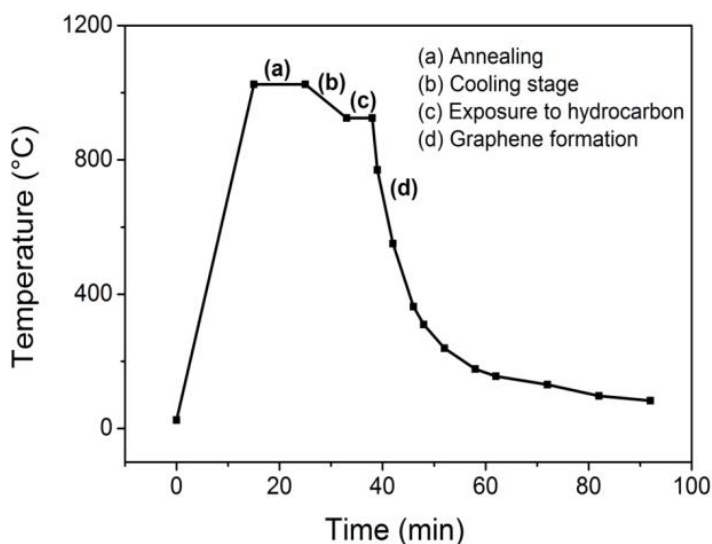


Fig. 4.11. Illustration of the temperature-time profile of the graphene growth process by CVD [adopted from Ref. 71].

After graphene growth, the XPS study was repeated (Fig. 4.12). In the C1s core level spectrum, the presence of the sp^2 bonded carbon peak at $\sim 284.6\text{eV}$ confirmed the growth of graphene (Fig 4.12a). The binding energy of graphene is comparable to the values reported in the literature [79c,83,90,91]. The authors deduced that the binding energy of graphene on polycrystalline Ni lies within the range of 284.3 to 284.5eV. On the other hand, the range of binding energy of graphene on single-crystal Ni(111) was reported from 284.8 to 285.0eV [92]. This high binding energy could be due to the strong interaction between graphene and single-crystal Ni(111) than the graphene/polycrystalline Ni system [92b]. Besides, no oxide signals were recorded after graphene growth (Figs. 4.12b and c).

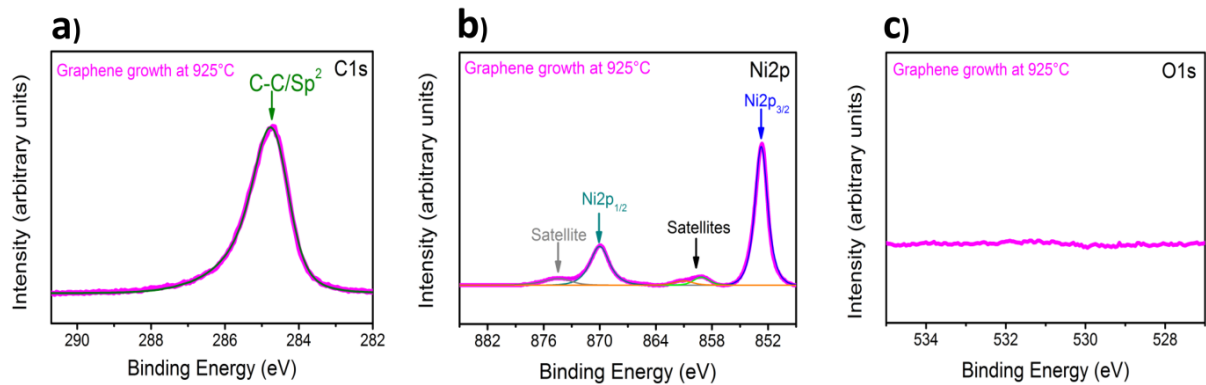


Fig. 4.12. XPS analysis: (a) C1s, (b) Ni2p, and (c) O1s spectra taken after the growth of graphene at 925°C.

Influence of graphene growth on grain growth in Ni film

The EBSD experiments were also performed again in order to investigate the Ni grain size distributions; results are provided in Fig. 4.13. One can observe that the orientation maps and the Ni grain size distributions remained the same before (Fig. 4.8) and after the graphene growth (Fig. 4.13). This indicates that graphene growth did not impact the grain growth in the Ni films. In other words, the annealing step carried out at higher temperatures than the temperature used for graphene growth forced the surface morphology of Ni films to a structural state which remained stable during the graphene growth.

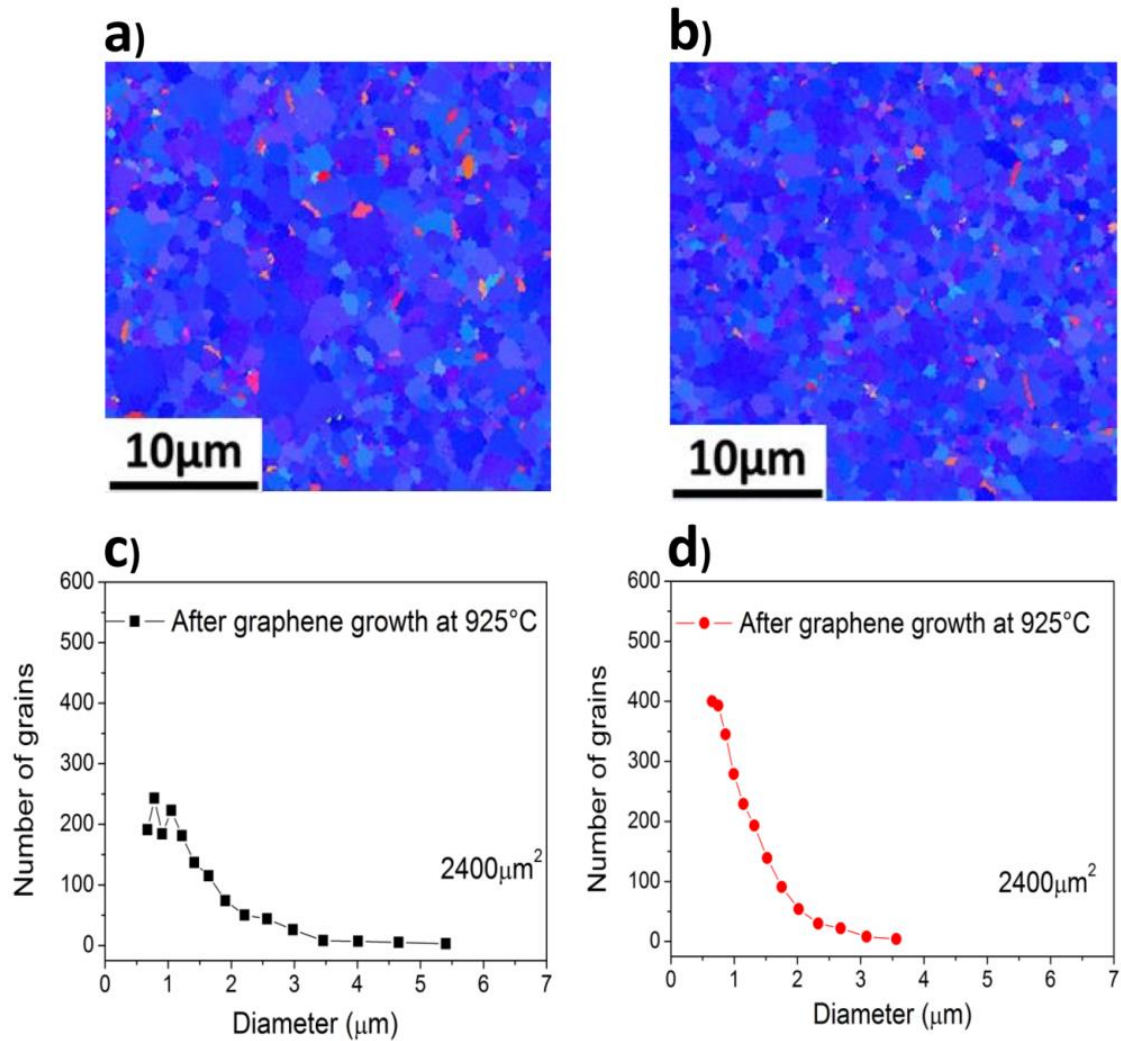


Fig. 4.13. EBSD analysis: (a–b) Orientation maps (c–d) grain distribution collected after the growth of graphene at 925°C [adopted from Ref. 71].

Characterization of graphene by SEM and Raman spectroscopy

In the next step, SEM was used to identify the layer thickness of graphene. Fig. 4.14 presents the images taken with the in-lens detector. The in-lens detector was used because it generates different color contrasts of a surface based on the work function. In SEM images, one can see the thickness non-uniformity of graphene. Based on the color, the surfaces of the scanned areas are divided into three distinct regions. In Fig. 4.14, the light grey or

brighter areas represent the thinner graphene (label 1), whereas labels 2 and 3 indicate thicker graphene [83,93,94].

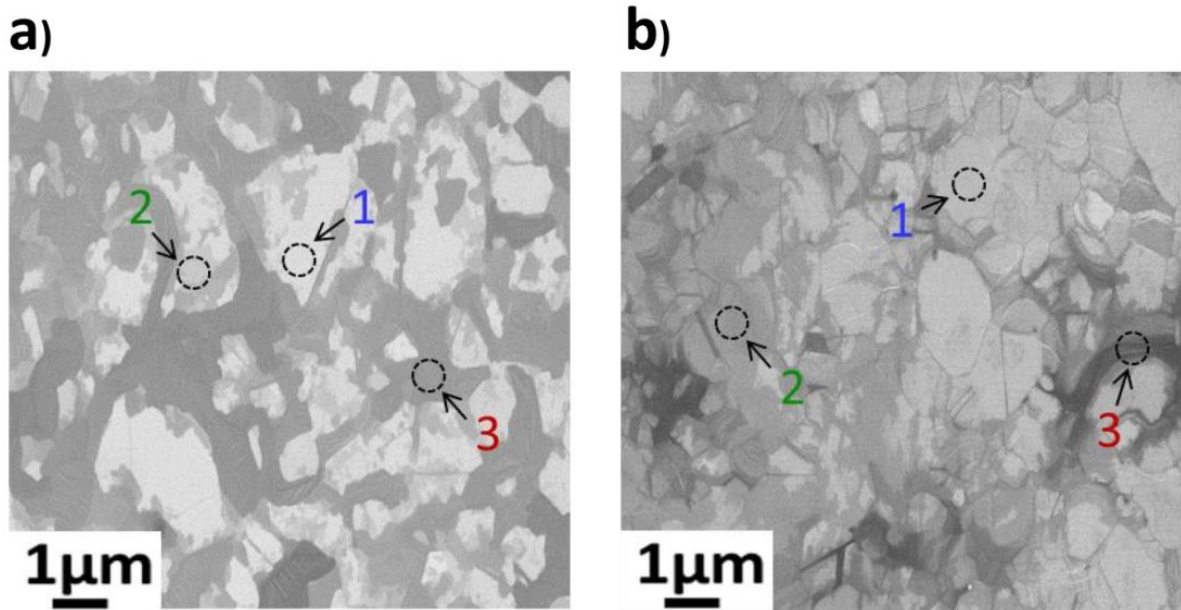


Fig. 4.14. SEM images of graphene grown on Ni films annealed in (a) hydrogen and (b) vacuum [adopted from Ref. 71].

In the last step, the quality of the obtained graphene was examined by Raman spectroscopy. A typical Raman spectrum of graphene is comprised of three Raman peaks, such as G peak ($\sim 1580\text{cm}^{-1}$), D peak ($\sim 1350\text{cm}^{-1}$), and 2D peak ($\sim 2700\text{cm}^{-1}$) [56,58]. The G peak results from in-plane C-C stretching mode, whereas the D peak or defect mode arises due to a double resonance process. The activation of the D peak requires one iTO phonon and a defect. The 2D peak results from a second-order two-phonon Raman process involving two iTO phonons near the K point [55,56,58]. The peak height and FWHM of the 2D band are used to distinguish the number of graphene layers. For monolayer graphene, the 2D band peak is higher than that of the G peak. The 2D band peak height reduces with the increased number of graphene layers while its width increases [56]. Raman spectra were recorded at three different regions depending on the layer thickness of graphene, as shown in Figs. 4.15a and b. The small defect peaks in Figs. 4.15a and b indicate that good-quality graphene films could

be grown in both conditions. In addition, the FWHM of the 2D band was determined by performing Raman mappings over $10 \times 10 \mu\text{m}^2$ areas of both the samples. Results are presented in Figs. 4.15c and d.

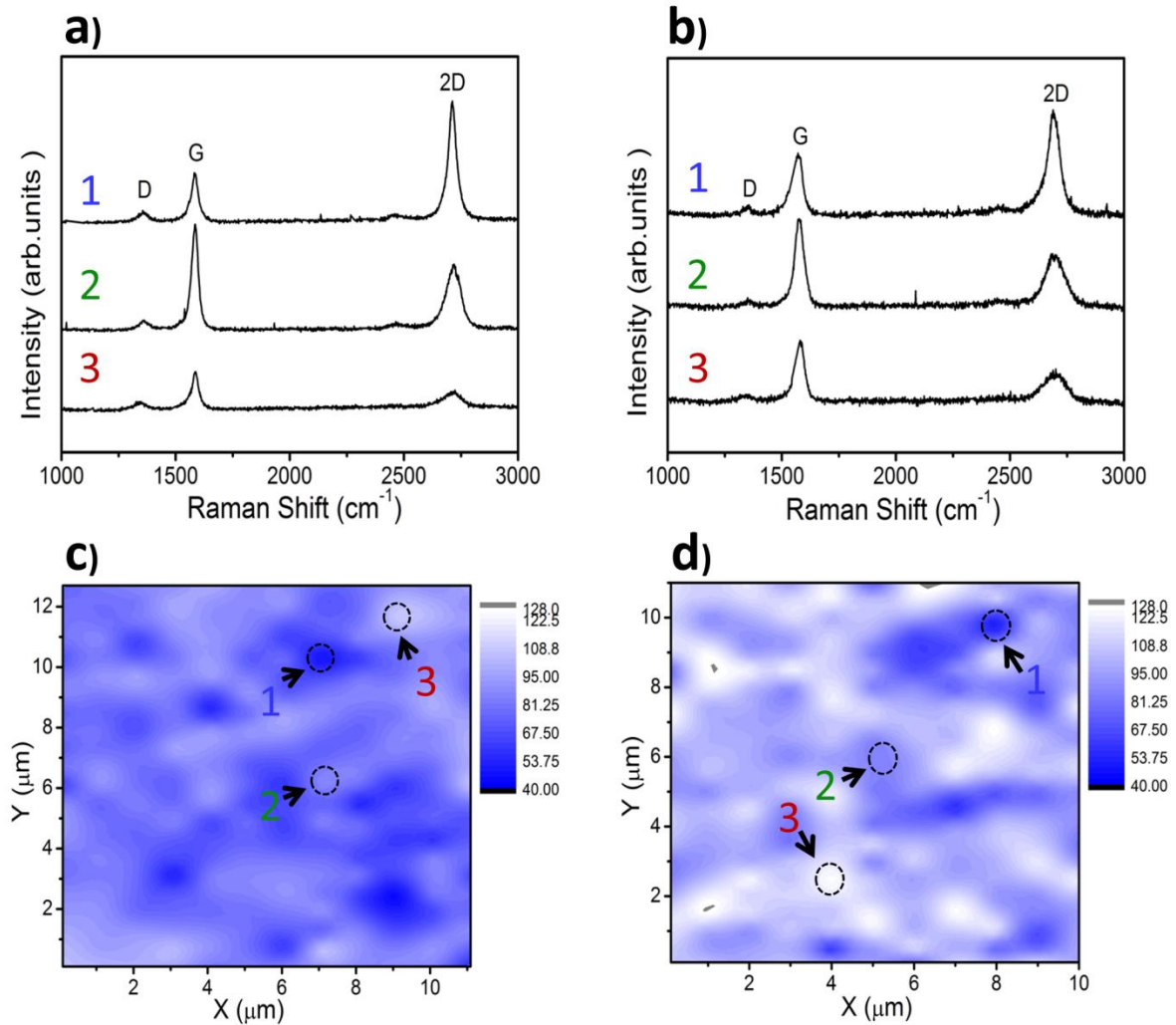


Fig. 4.15. Raman spectra of graphene grown on Ni films annealed in (a) hydrogen and (b) vacuum; different colors are corresponding to spectra taken from different areas. Raman maps (2D-FWHM) of graphene grown on Ni films annealed in (c) hydrogen and (d) vacuum [adopted from Ref. 71].

As seen, 2D-FWHM was within the range of 42 to 106cm^{-1} for hydrogen annealed Ni films. For the films annealed in vacuum, the range of 2D-FWHM was $51\text{--}128\text{cm}^{-1}$. The lower values of FWHM showed the growth of thinner graphene on the Ni films annealed in hydrogen

[43,89,95]. Besides, the intensity ratio of 2D to G peaks (~ 2.4) indicated mono-bilayer graphene growth, as shown in Fig. 4.15c (label 1) [83,89]. The I2D/IG intensity ratio dropped to ~ 0.6 (label 2) and ~ 0.5 (label 3) for few (3–5) and multilayer graphene, respectively (Fig. 4.15c) [83,89]. On the other hand, the I2D/IG intensity ratio (~ 1.7 (label 1), ~ 0.5 (label 2), and ~ 0.4 (label 3)) revealed the growth of thicker graphene on the films annealed in vacuum (Fig. 4.15d). To summarize, Raman analysis provided a direct correlation between Ni grain sizes and the thickness of graphene. For instance, larger grains and reduced grain boundaries facilitated the growth of thinner graphene on the films annealed in hydrogen. On the contrary, smaller Ni grains and therefore increased GBs caused the growth of thicker graphene on the films annealed in vacuum.

Summary

In this PhD study, the impacts of different annealing conditions (hydrogen and vacuum) on the morphology of 200nm thick polycrystalline nickel films deposited on 8-inch 100nm SiO₂/Si(001) substrates were investigated. Both annealing conditions favored the crystallization of Ni along (111) orientation. However, omega scans showed that the mosaicity of the Ni grains was reduced in hydrogen annealed Ni films. Ni films annealed in hydrogen contained larger grains, as determined by EBSD. These larger Ni grains could be due to the incorporation of hydrogen into the interstitial sites of Ni films. According to Raman analysis, the growth of thinner graphene on the films annealed in hydrogen is attributed to the larger Ni grains and reduced GBs. However, the surface of Ni films annealed in hydrogen was rougher (Rq ~ 28 nm). Although the surface roughness of Ni films annealed in vacuum was low (Rq ~ 10 nm), thicker graphene was grown on these films because of the smaller Ni grains and increased GBs.

4.1.1. Ni-mediated growth of graphene on silicon dioxide

Preparations of Ni structures for graphene synthesis

The knowledge obtained from the previous study of graphene growth on blanket Ni wafers was further implemented in this PhD work for obtaining graphene on silicon dioxide. For this purpose, two different types of structured Ni wafers have been prepared. These wafers were designed so that graphene growth could be achieved on the surface of silicon dioxide between the Ni bars and underneath the Ni films.

4.1.1.1. Substrates preparations for graphene growth between Ni bars (STRUCTURES A)

Two different thicknesses (100 and 200nm) of Ni layers were tested in order to grow graphene between Ni bars. These Ni layers were grown by PVD technique on 200mm Si(001) wafers covered with 100nm thermally grown SiO₂ layers. Different Ni structures were then formed after wet chemical etching of Ni with a piranha solution. The layout of the mask was designed in order to have a large number of Ni structures for the evaluation of the growth and extraction of the electrical properties of graphene. These structures were named *STRUCTURES_A* that were of different types, such as transmission line method (TLM), Kelvin, Hall, Resistance, etc. The layout of the *STRUCTURES_A* is shown in Fig. 4.16.

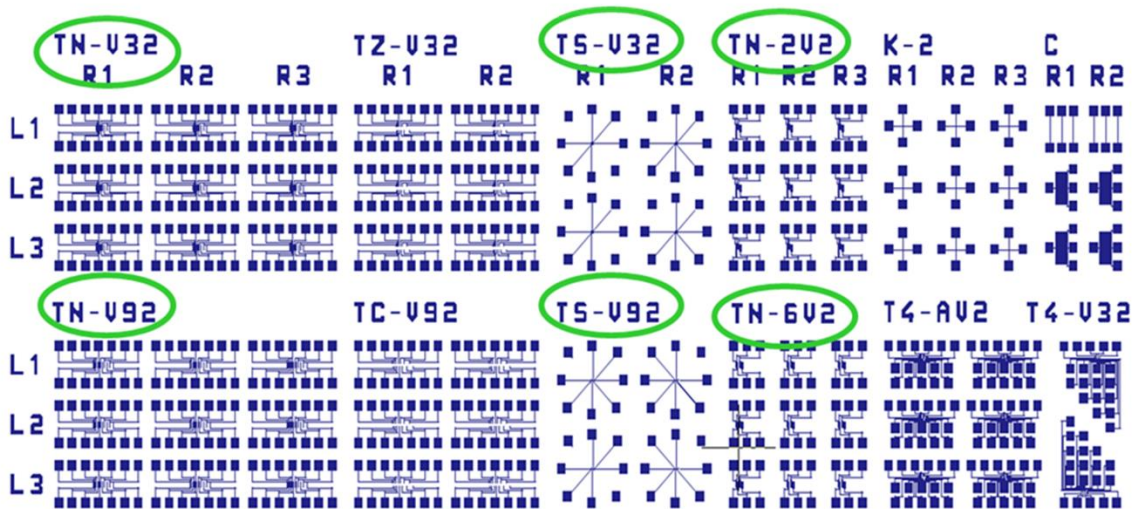


Fig. 4.16. The layout of the structured Ni wafer.

As the width of Ni and the distances between Ni bars can influence graphene growth, they were kept different. For example, the widths of Ni bars and the distance between them have been varied from 2 to 9 microns and 0.5 to 32 microns, respectively. As an example, an optical image of a TS-3 structure is shown in Fig. 4.17.

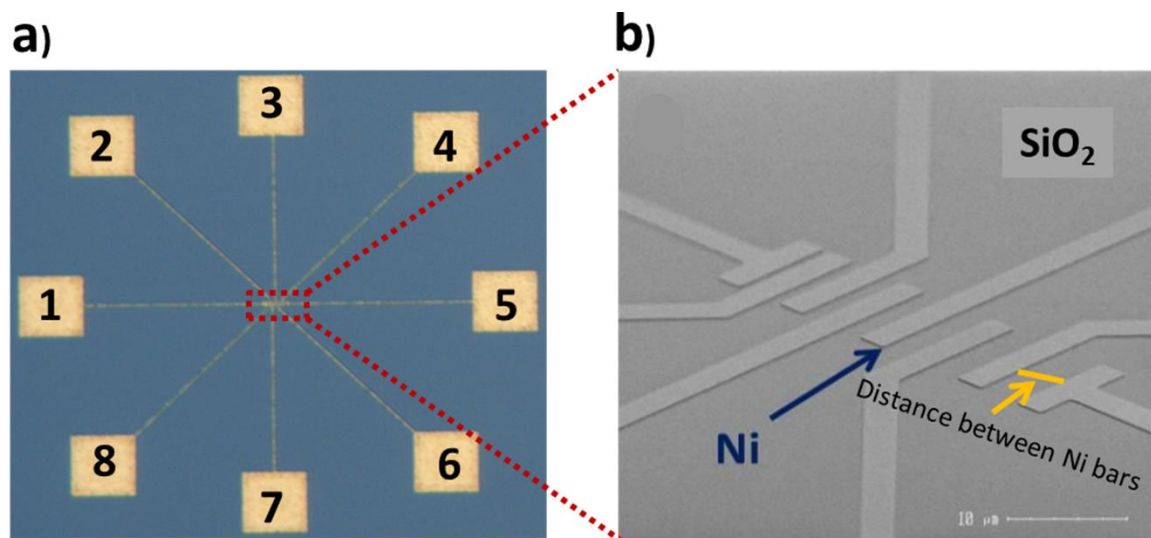


Fig. 4.17. (a) Optical image of a TS-3 structure with numbered Ni contact pads and (b) SEM image of the area marked by the red dashed line in panel a.

Graphene synthesis

From previous experiments (section 4.1), it was found that 100nm thin Ni films can de-wet at much lower temperatures. Therefore, the first step was to optimize graphene growth temperature in order to obtain good quality graphene, at the same time preventing the delamination of thin Ni. For this purpose, graphene growth was performed in the temperature range of 875-950°C. It was noted that higher temperatures caused the dewetting of Ni.

Hence, a different approach was explored in this thesis work in order to grow graphene between Ni bars. This alternative growth mode involves the use of lower temperatures (600-700°C). The result of the lower growth temperature process showed significant improvements in the physical aspects of the Ni structure in comparison to the high temperature process. This is shown in Fig. 4.18.

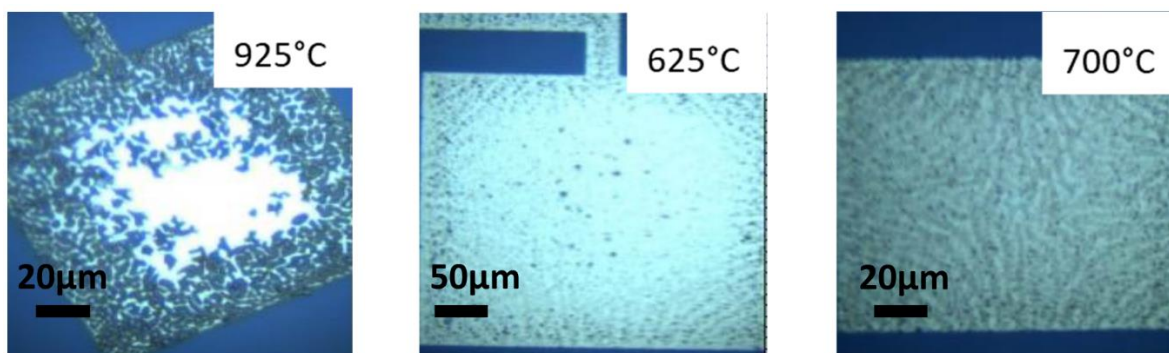


Fig. 4.18. Optical images are showing the quality of Ni at higher (left) and lower (middle and right) temperatures.

In addition to lower growth temperature, different recipes based on higher pressure (720mbar) and various carbon precursors (methane and acetylene) were also used to obtain graphene between Ni bars. It is worth mentioning here that Dr. Alex Jouvray performed

some of the growth experiments at Aixtron Ltd., England within the framework of “Graphica” project.

The results of the sample grown under 720mbar at 600°C using methane (carbon precursor) and hydrogen (carrier gas) are provided in Fig. 4.19. It can be seen that Ni remains intact during the graphene growth process. The Raman spectra indicated that graphene-like films are not only grown on Ni bars but have also been extended a few microns away from them (Fig. 4.19b). Also, the grown layers showed conductivity, but only for the smallest distances, such as 1–2 (Fig. 4.19c).

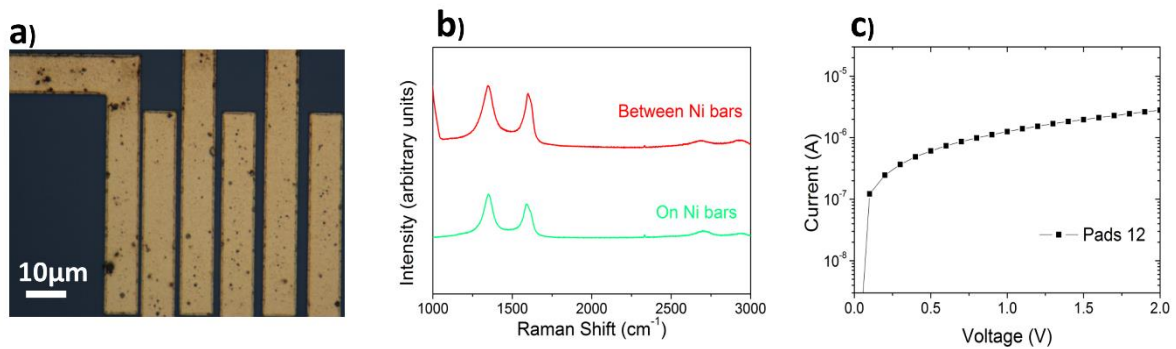


Fig. 4.19. Graphene growth on Ni structures with 100nm thickness (a) optical image of a selected structure, (b) Raman spectra collected on and between Ni bars are indicated by green and red lines, respectively, and (c) electrical measurements of as-grown graphene sample.

Then, the same growth conditions were used to grow graphene on wafers with 200nm thickness of Ni. Like 100nm Ni structures, graphene-like features were also observed on and between Ni bars, as shown in Fig. 4.20. Moreover, it was found that the conducting states also existed between Ni pads, even for the largest distances (pads 3–4).

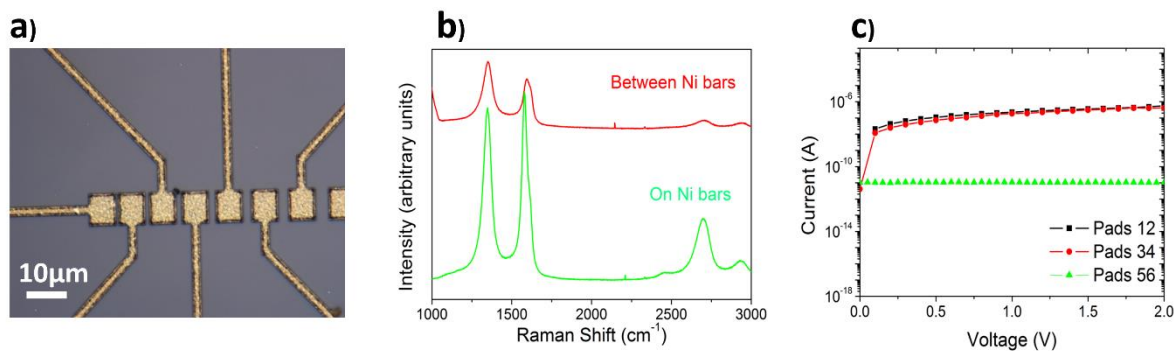


Fig. 4.20. Graphene growth on Ni structures with 200nm thickness (a) optical image of a selected structure, (b) Raman spectra collected on and between Ni bars are indicated by green and red lines, respectively, and (c) electrical measurements of as-grown graphene sample.

On the other hand, all other higher temperatures (greater than 600°C) and acetylene-based recipes caused the complete removal or de-wetting of Ni structures (Fig. 4.21). These results indicate that although the developed method can synthesize graphene directly on silicon dioxide, the process should be optimized further to deal with the issues related to the limited lateral extension of graphene and the de-wetting of Ni.

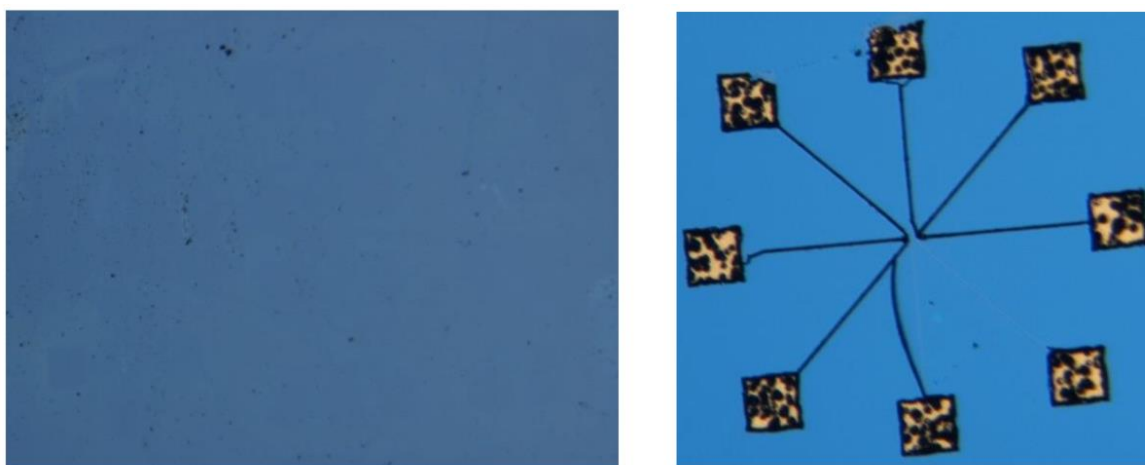


Fig. 4.21. Optical image of Ni structure taken after graphene growth using higher temperature (left) and acetylene based recipes (right).

4.1.1.2. Growth of graphene underneath Ni (STRUCTURES B)

The test structures (*STRUCTURES_B*) used for graphene growth underneath Ni are provided in Fig. 4.22. In this configuration, a two-mask set layout was realized, where, firstly, 80nm TiN layers were grown by PVD and structured in the same configuration as Ni was structured in *STRUCTURES_A*. Additionally, a 100nm thin Ni layer was grown over TiN and structured in stripes with various lengths and widths. Similar to *STRUCTURES_A*, the layout of the mask was designed in order to have a large number of different structures for the evaluation of the growth and extraction of the electrical properties of graphene.

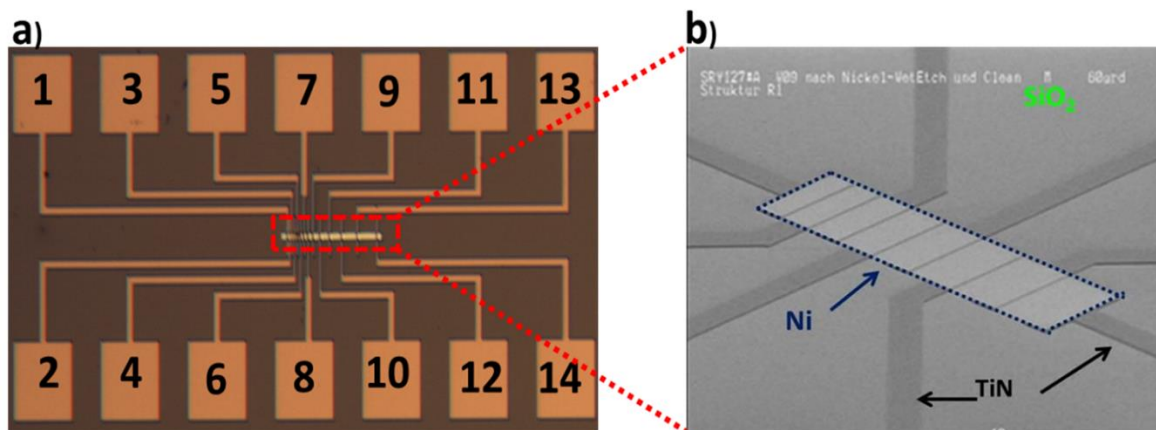


Fig. 4.22. (a) Optical image of a Ni structure with numbered Ni contact pads and (b) SEM image of the area marked by the red dashed line in panel a.

After the preparations of Ni structure, graphene growth experiments have been performed under optimized growth conditions, as given in table 4.4.

Table.4.4. Conditions for graphene deposition.

Growth temperature (°C)	Carbon source	Carrier gas	Pressure (mbar)
700	Methane	hydrogen	720

Characterization of graphene

Firstly, the quality and electrical behavior of as-grown graphene were investigated. The optical image shown in Fig. 4.23a indicates that Ni remained intact during the graphene growth process; therefore, the growth is expected over the entire surface of the Ni bars. The Raman results demonstrated the presence of graphene-like films over the whole Ni bars. As similar spectra are recorded from different points, a typical Raman spectrum is given in Fig. 4.23b. One can see that the conduction paths existed between TiN pads for all distances (Fig. 4.23c).

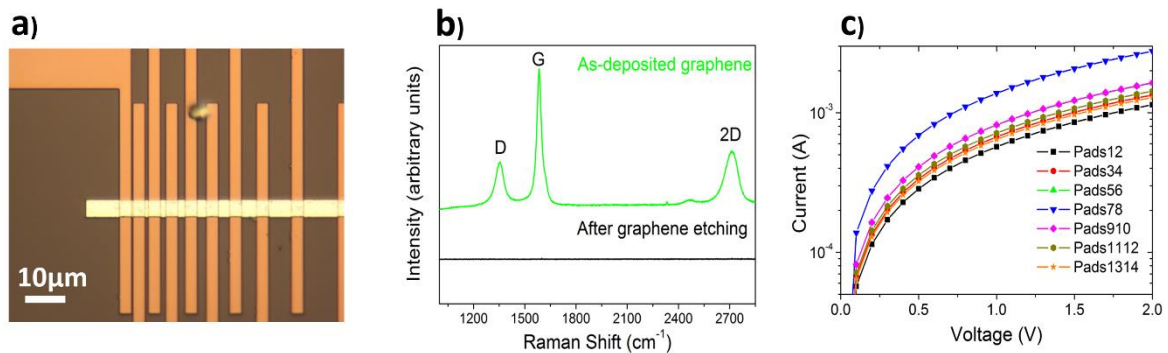


Fig. 4.23. Graphene growth on *STRUCTURES_B* (a) optical image of a selected structure, (b) Raman spectra on Ni bar is represented by a green line, whereas the black line shows the spectrum collected after graphene etching, and (c) electrical measurements of as-grown graphene sample.

As the purpose of this work is to grow graphene underneath the Ni films; therefore, the next step was to remove graphene from the surface of the Ni using oxygen plasma etching. After 8mins of plasma etching, the Raman spectrum was collected again. Results showed the removal of graphene as indicated by the black line in Fig. 4.23b). Then, the samples were immersed for 10 minutes in the ammonium persulfate solution to remove Ni layers so that graphene on the surface of silicon oxide could be detected. One can notice that Ni structures

have also been removed from the samples, as shown in Fig. 4.24a. Also, the auger spectra collected on silicon dioxide and TiN bar (as marked by red and blue spots in Fig. 4.24a) indicated the absence of Ni and hence confirmed the removal of Ni (Fig. 4.25).

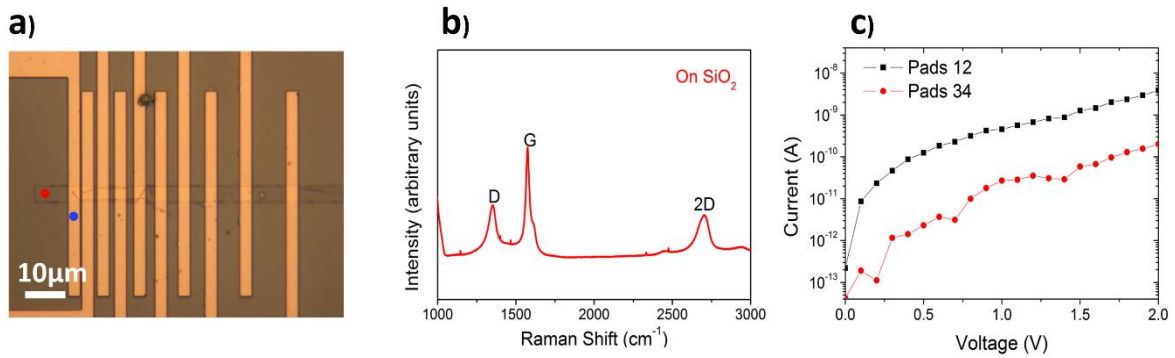


Fig. 4.24. After Ni etching, (a) optical image of a selected structure, (b) Raman spectra collected Silicon dioxide, and (c) I-V characteristics.

Further investigations of the etched areas were performed by Raman spectroscopy and electrical measurements. The experiments revealed that carbon diffused through the nickel layer, and graphene is formed on the insulating SiO₂ layers (red line in Fig. 4.24b). In addition, electrical measurements showed the presence of electrical paths between the TiN bars (Fig. 4.24c).

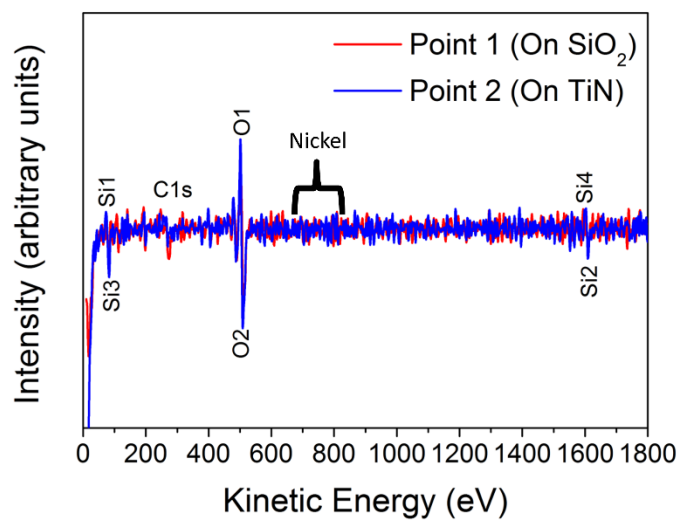


Fig. 4.25. Auger spectra were collected on SiO₂ (red) and TiN bar (blue) after etching away Ni.

In order to determine that the electrical response of the sample is due to the presence of the grown films, the films were etched away in oxygen plasma for 9 minutes (Fig. 4.26a). Raman spectra collected on SiO₂ demonstrated the removal of the layers, as displayed in Fig. 4.26b. No electrical response was observed between the TiN pads after etching away graphene. Hence, the conduction between the Ni bars could be attributed to the grown graphene-like films (Fig. 4.26c).

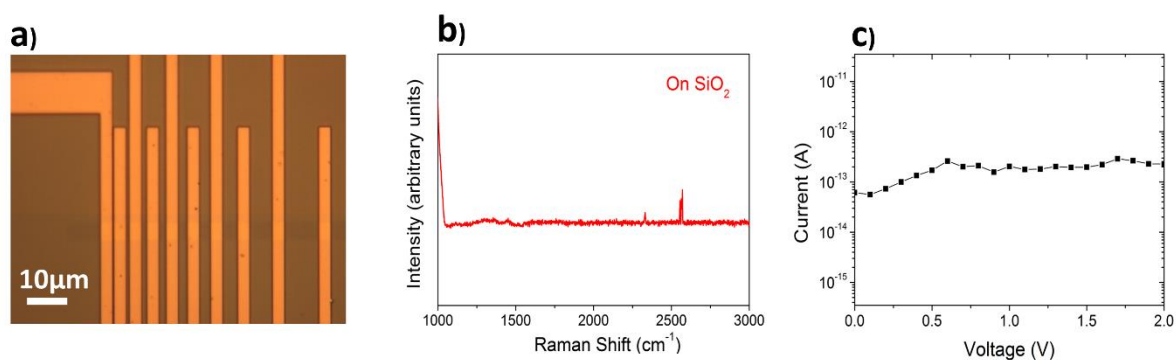


Fig. 4.26. After graphene etching, (a) optical image of a selected TLM structure, (b) Raman spectra on silicon dioxide, and (c) I-V characteristics.

Summary

Two different routes for the Ni-assisted CVD growth of graphene on insulating substrates were investigated. Different thicknesses of Ni (100 and 200nm) were used to prepare the structured wafers in order to obtain graphene between Ni bars. In addition, growth experiments were performed based on different recipes. It was found that graphene-like features could be grown on and between Ni bars on both Ni structures only when the lower temperature (600°C) and methane were used. Furthermore, electrical measurements showed that conduction paths existed between Ni pads, but only for the smallest distances (1–2 and 3–4).

Similar to the graphene growth between the Ni bars, graphene-like films were obtained underneath the Ni layers. Thus, results obtained during this PhD study indicate that the Ni-

assisted graphene growth approach can grow graphene on dielectrics. However, the growth of graphene-like films, the limited lateral extension of graphene, and the de-wetting of Ni structures are the main issues. Hence, this approach needs to be optimized further.

4.2. Growth of graphene on 200mm Ge(001)/Si(001)

Substrates preparations for the growth of graphene

The substrates for the growth of graphene were prepared by depositing epitaxial, 2 μm thick Ge(001) films on 8-inch Si(001) wafers by CVD. These Ge films were deposited under the same conditions used in Ref [96].

Optimization of Ge thickness for graphene growth

It is well known that silicon diffuses into Ge at higher temperatures [96,97]. This effect is undesirable as it results in the formation of silicon carbide that can prevent the growth of high-quality graphene [98]. Therefore, the first step of this study was to optimize the layer thickness of the Ge. Fig. 4.27 shows a typical example of the TEM/EDX profile of 3 μm thick Ge layer (annealed at 885 $^{\circ}\text{C}$). As illustrated in Fig. 4.27, Si diffuses into 1.2 μm of Ge. Therefore, to prevent any silicon diffusion onto the Ge surface, the Ge layer thickness of 2 μm was selected for this PhD work.

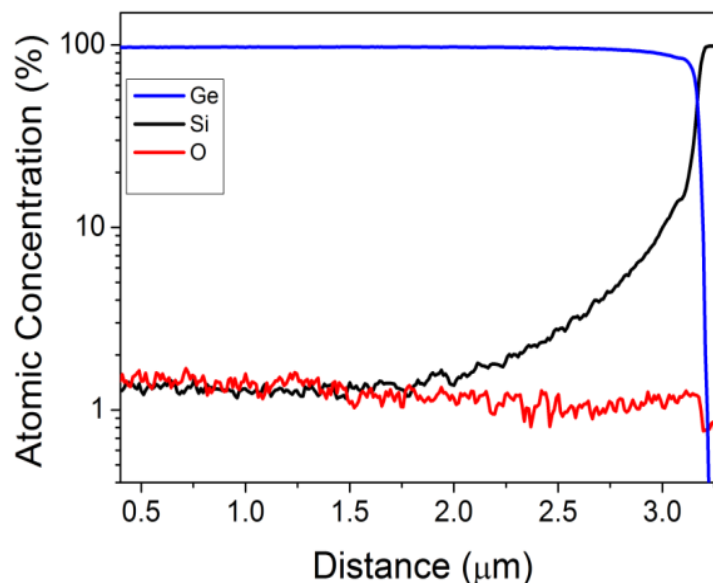


Fig. 4.27. Line scan of the TEM/EDX depth profile of the 3 μm Ge(001) on Si(001) substrate [adopted from Ref. 99].

Graphene growth on Ge(001)

After defining the layer thickness of Ge, graphene growth experiments have been performed in a CVD tool. The conditions for graphene deposition are listed in table 4.5. In addition, the process flow for the deposition of graphene on Ge(001) is illustrated in Fig. 4.28.

Table.4.5. Conditions for graphene deposition.

Growth Temperature (°C)	Carbon source	Carrier gas	Deposition time (min)
885	Methane	Hydrogen/argon	60

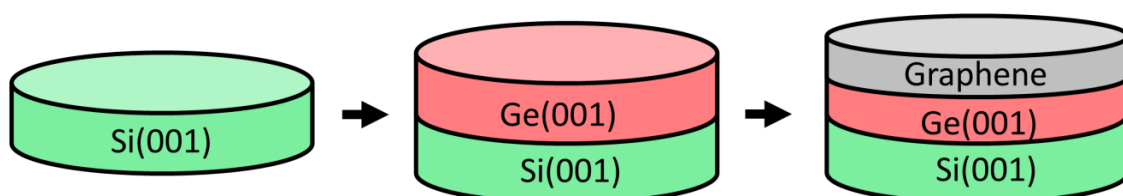


Fig. 4.28. Illustration of the process flow for graphene deposition on (001) oriented Ge substrates.

Characterization of graphene

The as-deposited graphene/Ge(001) samples were firstly investigated by XPS. The presence of an asymmetric peak at the binding energy of $\sim 284.4\text{eV}$ in the C1s spectrum confirmed the growth of graphene, as shown in Fig. 4.29a. This is in agreement with the literature work [100]. In addition to graphene peak, some additional features corresponding to adventitious contaminations, such as C-H (285eV), C-O ($\sim 286\text{eV}$), C=O ($\sim 287\text{eV}$), O-C=O ($\sim 289\text{eV}$), were also detected. Then, the quality of the obtained graphene layers was checked by Raman spectroscopy. Raman line spectra (~ 100 points) were collected across the entire wafer as indicated by the yellow dotted line in Fig. 4.29b. Results showed that very similar spectra

could be obtained on the full wafer, indicating that graphene can be uniformly grown over large areas. As an example, Raman spectra collected from three distinct regions (marked as 1, 2, and 3) are depicted in Fig. 4.29c. The uniformity of the grown graphene was further investigated using spectroscopic ellipsometry. According to ellipsometry measurements, the average thickness of graphene over the entire wafer was $\sim 0.27\text{nm}$ with a standard deviation of 4%. This indicates that graphene is uniformly distributed on the large-sized wafer, which is in agreement with the Raman study.

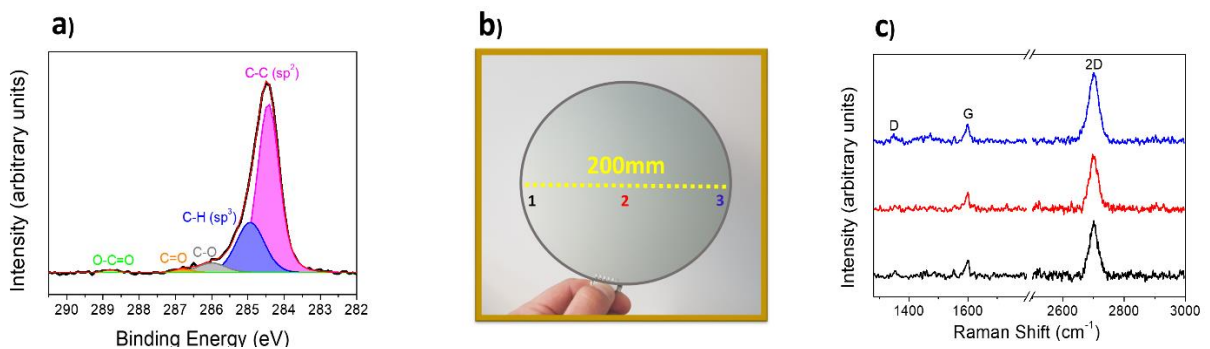


Fig. 4.29. (a) C1s spectrum, (b) Graphene grown on 200mm Ge/Si wafer, and (c) Raman spectra at the indicated places.

A micro Raman mapping over $10 \times 10\mu\text{m}$ area was performed in order to evaluate the properties of graphene on the microscopic level. A Raman map of the 2D-FWHM is presented in Fig. 4.30a. As seen, the FWHM of the 2D band lies within the range of 36 to 42cm^{-1} . The range of 2D-FWHM obtained in this study is similar to those reported in the literature [100]. The average value of FWHM of the 2D band was about 39cm^{-1} (Fig. 4.30b), which is higher as compared to the FWHM of perfect monolayer graphene. The high value of 2D-FWHM might, in principle, show the presence of bilayer graphene. However, no significant concentration of such bilayer domains was observed in SEM images taken after transferring graphene onto SiO₂ (Fig. 4.32a).

Additionally, it has been recently reported that the broadening of the 2D band is also strongly related to the nanometer-scale strain variations (i.e., over distances smaller than the Raman laser's spot size) in graphene [101].

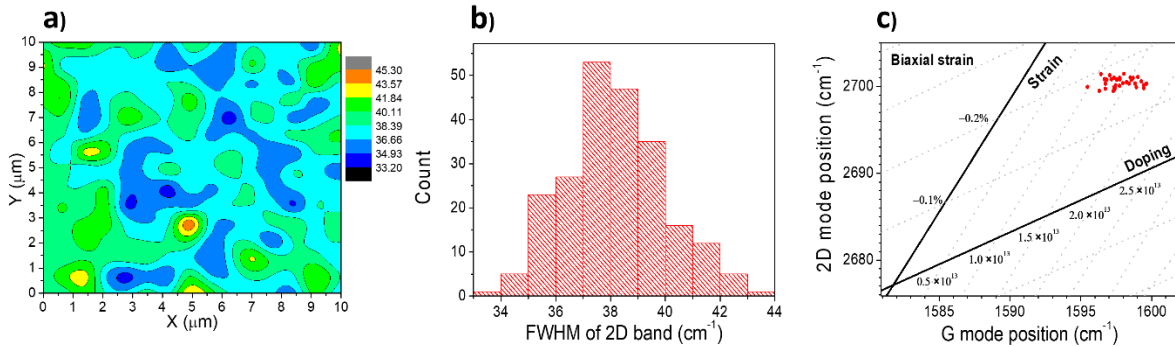


Fig. 4.30. Raman analysis: (a) FWHM map of 2D mode, (b) the histogram of the 2D-FWHM, and (c) plot of the 2D vs. the G band position.

The strain and doping levels in graphene were therefore evaluated by plotting the position of the 2D band vs. the position of the G band [102]. According to 2D/G plots, the strain in graphene is compressive (Figs. 4.30c). The estimated value of strain (biaxial) is -0.15% , while the doping level in graphene is $(2 \times 10^{13} \text{cm}^{-2})$. The values of strain and doping level of graphene measured in this PhD work were comparable to those derived from a 2D-G plot for MBE grown graphene on Ge(001) (-0.3% biaxial and 10^{13}cm^{-2}) [103]. However, this is significantly different from the graphene grown on Ge(001) by UHV-CVD from C_2H_4 ($+0.4\%$ biaxial, no indication of an interfacial layer). This difference could be attributable to different nucleation and growth mechanisms during both CVD processes.

Another quantity measured in this PhD work is the surface roughness. First of all, the surface roughness of as-deposited Ge and then temperature treated samples were investigated by optical profilometry (on $1 \times 1 \text{nm}$ scale). The surfaces of as-deposited Ge were very smooth (typical $R_a \approx 0.5 \text{nm}$). However, the roughness was slightly increased ($R_a \approx 0.7 \text{nm}$) after exposing the Ge substrates to the graphene deposition temperature. This means that no

significant roughening of the surface occurred. A more detailed analysis of surface morphology was performed by SEM and AFM. Fig. 4.31a depicts the SEM images of a graphene/Ge(001) system obtained after optimizing the growth process. Ge faceted surface, which is attributable to graphene growth, is visible and agrees with the literature reports [100,104], where graphene deposition was performed on Ge(001) by the CVD method under similar growth conditions used in this thesis work. A literature study has shown that the Ge(001) surface reconstructs into hills and valleys structures (two families of (107) facets oriented 90° to each other) during the graphene growth, which is associated with the formation of two rotational graphene domains on Ge(001) [100]. Also, the Ge faceted surface can be seen in the AFM image (Fig. 4.31b). The typical facets height is from 2 to 5nm, while the surface roughness (R_a) is measured within the range of 0.7–1.1nm.

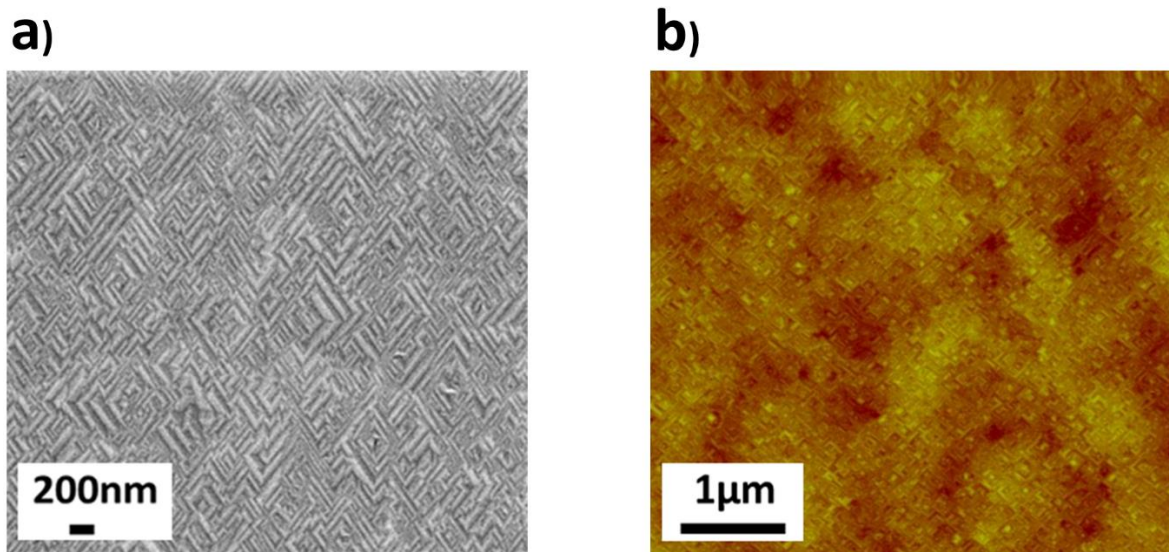


Fig. 4.31. (a) SEM and (b) AFM images of the graphene/Ge(001) system.

On the other hand, the faceted surface of Ge was not observed after growing graphene on Ge(001) by atomic carbon molecular beam, where H background was not present [105]. Further, the Ge(107) facets were also absent when graphene was grown using UHV-CVD, where the coverage of the Ge surface with H was estimated to be very low [103]. This

represents that the Ge surface faceting might be attributed to the adsorbed hydrogen. In this PhD work, the possible mechanisms (based on the DFT calculations done by Dr. Jaroslaw Dabrowski) for the surface faceting of Ge underneath the graphene are provided and are briefly described below.

The orientation of graphene nucleated along $\langle 010 \rangle$ directions of the substrate is rotated by about 4° in order to minimize the lattice mismatch to the substrate. This is consistent with the literature report [106]. The $\langle 010 \rangle$ family is the family of directions in which the $\{107\}$ facet ridges will be formed. The mechanism of faceting formation can be explained as follows: the surface of Ge(001) contains dimer vacancies. The sublimation of Ge atoms by hydrogen increases the number of these vacancies. These vacancies diffuse on the surface and contribute to surface step motion. In addition, they accumulate into new terraces. The surface faceting of Ge initiates when a chain of hydrocarbon polymer present in the system attaches to a surface step. Then, instead of annihilating at this step edge, the surface vacancies accumulate at a certain distance from it. In other words, it can be said that a graphene chain may pin the motion of the surface step at which it nucleates. As these vacancies cannot cross a pinned step, therefore, the flat surface of Ge(001) reconstructs into $\{107\}$ facets.

The next step was to transfer graphene from the Ge/Si substrates onto the 100nm SiO_2/Si substrates to evaluate its electrical properties. Therefore, the 200mm wafer was cut into pieces of $2 \times 2\text{cm}$ in size. Graphene was then transferred onto SiO_2 by the electrochemical delamination method. It can be seen in Fig. 4.32a that the transferred graphene does not contain any types of cracks, holes, wrinkles, etc.

Nonetheless, the presence of a Raman D mode caused by the transfer in Fig. 4.32b indicates that the transfer step requires further optimization. Besides, the dark spots can be seen in

SEM images taken after graphene was transferred from Ge (Fig. 4.32a), which can be attributed to bilayer graphene. For the graphene/Ge system, the estimated fraction of bilayer is below 1% (approximately $0.6\% \pm 0.1\%$).

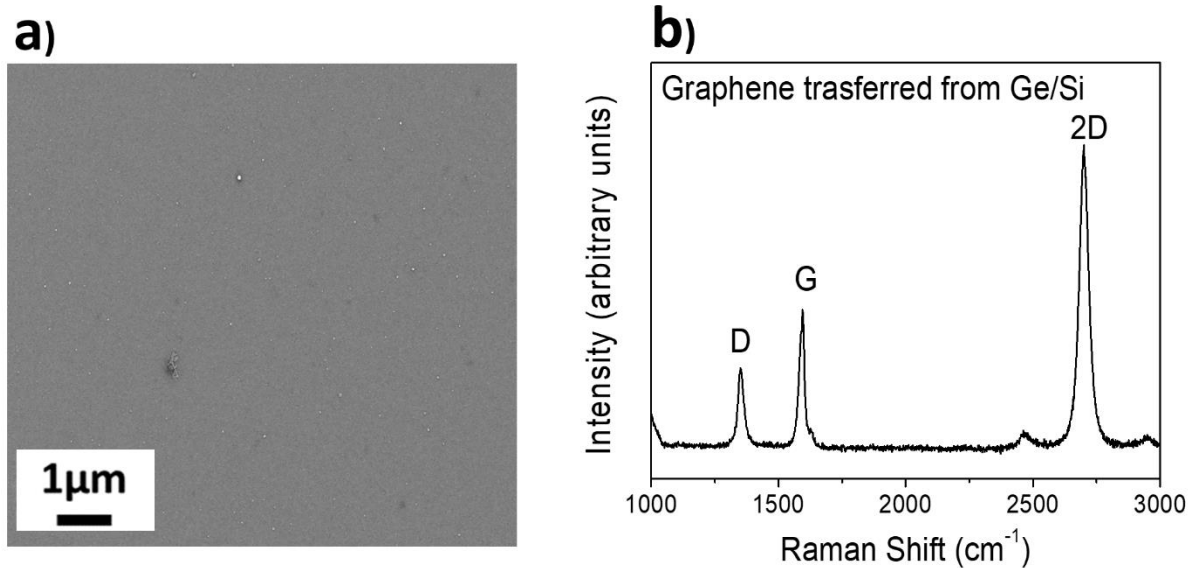


Fig. 4.32. SEM image of the graphene transferred onto SiO₂/Si substrates from (a) Ge/Si and (b) Raman spectrum of the transferred graphene from Ge/Si.

Hall measurements were typically performed on 10 pieces (obtained by cutting the full 200mm wafer) so that the electrical properties of the transferred graphene can be determined. The electrodes were kept at the separation distance of 1cm. Electron mobility of $\mu \approx 300 \pm 20 \text{ cm}^2/\text{Vs}$ and sheet resistance of $R_s \approx 2000 \pm 100 \Omega/\text{sq}$ were extracted. These values are lower in comparison to the ones reported in the literature [100,107]. These differences are basically attributed to the residual transfer damage and/or the polymer contamination, as shown in Fig. 4.32b. Also, the surface quality of Ge before the synthesis of graphene could contribute to the inferior R_s and μ . Unhealed surface damage and residual oxide might lead to the formation of defects that degrade the electrical quality of graphene. At the same time, such defects could be the possible pathways for oxygen to reach the graphene-covered Ge surface and oxidize it.

The oxygen contents in the samples were investigated by EDX and X-ray photoelectron spectroscopy. The EDX measurements were performed after covering the graphene sheet with a thin, thermally evaporated Al layer. For XPS experiments, graphene was not capped though the samples were annealed at 500°C for 1hour in UHV conditions before these experiments. The EDX measurements showed the presence of an oxygen-rich interfacial layer between graphene and Ge substrate (4.33a). XPS analysis also demonstrated the presence of O bonded to Ge (Fig. 4.33a, inset).

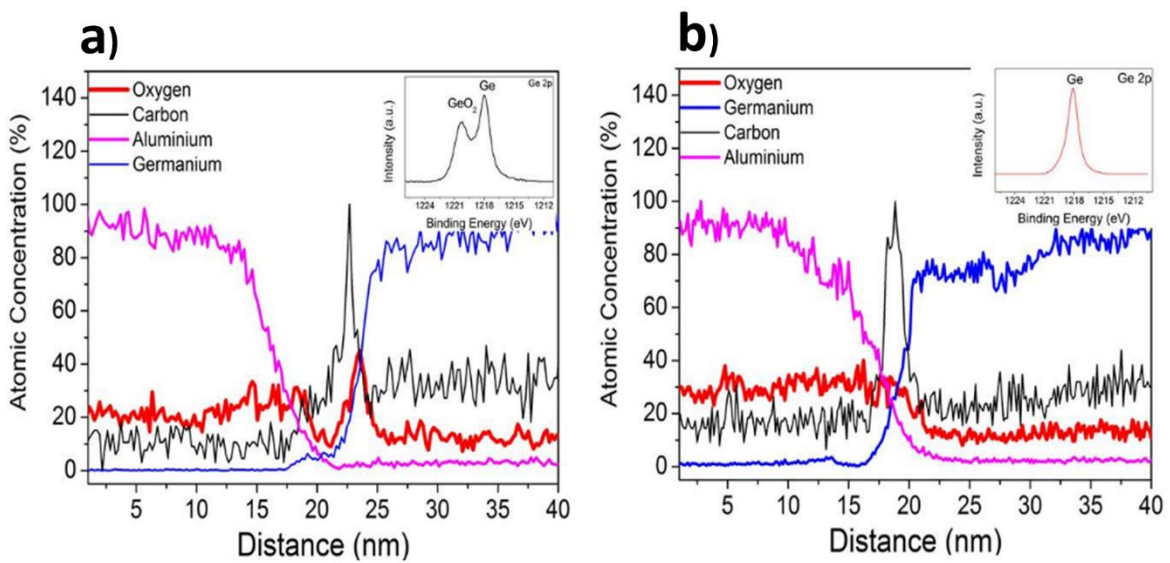


Fig. 4.33. EDX analysis of (a) initial and (b) optimized graphene on Ge. The XPS spectra were measured after annealing the samples at 500°C in UHV for 1hour. The XPS Ge2p spectra are given in the insets.

In order to improve the quality of the starting Ge surface, H₂ bake time before the deposition of graphene was increased, while the cooling rate after depositing graphene was decreased. In Fig. 4.33b, the results of the optimized growth process are illustrated. No oxygen contents were observed at the interface between graphene and Ge by EDX. In order to confirm this observation, XPS analysis was repeated. As seen in the inset of Fig. 4.33b, only elemental Ge peak is present at the binding energy of 1218eV. The electrical properties of these optimized

samples have then improved to $\mu \approx 500 \pm 20 \text{cm}^2/\text{Vs}$ and $R_s \approx 1500 \pm 100 \Omega/\text{sq}$. As the mobility values are still lower than those reported in the literature, further optimizations of growth and transfer steps are required.

Summary

In this PhD work, large-area graphene was synthesized on 200mm Ge/Si(001) substrates by the CVD method. The Raman study showed that uniform and high-quality graphene layers could be grown on Ge. The uniformity of grown graphene on a large-scale area was confirmed by spectroscopic ellipsometry. After transferring graphene on SiO₂ substrates, its electrical properties were extracted from Hall measurements. The extracted values of sheet resistance and mobility were $R_s \approx 1500 \pm 100 \Omega/\text{sq}$ and $\mu \approx 500 \pm 20 \text{cm}^2/\text{Vs}$, respectively. The high quality of the CVD graphene is attributable to the higher hydrogen coverage of Ge surface. This is because higher hydrogen coverage suppresses the graphene nucleation on Ge(001) dimer vacancies and reduces nucleation probability on a flat surface. During graphene growth, the Ge(001) surface reconstructs into (107) facets, which may also be responsible for the lower mobility values. The surface faceting of Ge(001) could be the result of the step pinning by graphene. This study also showed that both the as-grown and transferred graphene were free from any metallic contaminations.

4.3. Growth of graphene on 200mm Ge(110)/Si(110)

Substrates preparations for the growth of graphene

The substrates for the growth of graphene were prepared by depositing epitaxial, 2 μ m thick Ge(110) films on 8-inch Si(110) wafers by CVD. These Ge films were deposited under the same conditions used in Ref [96].

Graphene growth on Ge(110)

Although graphene can be grown on 8-inch Ge(001)/Si(001) substrates, however, its lower electrical mobility is the main drawback (as discussed in section 4.2). On the other hand, the growth of graphene grown on (110) oriented Ge substrates with superior electrical mobility ($\sim 10,620\text{cm}^2/\text{Vs}$) has been reported [51]. Hence, in order to obtain higher electrical mobility of graphene, its growth on Ge(110) substrates was tested in this PhD study. The graphene growth on Ge(110) was performed in a CVD tool. The conditions for graphene deposition are listed in table 4.6, while Fig. 4.34 illustrates the process flow for graphene deposition on Ge(110).

Table.4.6. Conditions for graphene deposition.

Growth Temperature (°C)	Carbon source	Carrier gas	Deposition time (min)
885	Methane	Hydrogen/argon	60

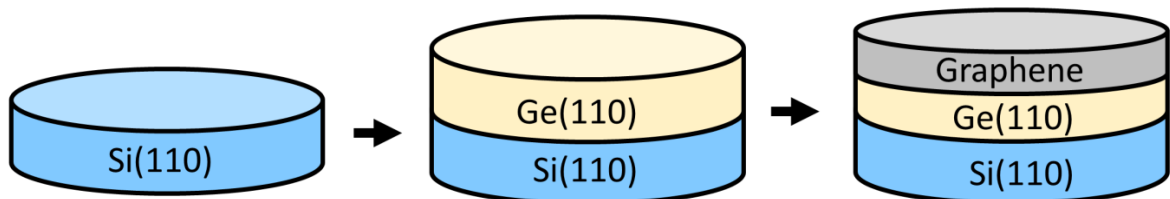


Fig. 4.34. Illustration of the process flow for graphene deposition on Ge(110)/Si(110) substrates.

Characterization of graphene

In the first step, the graphene growth on Ge(110) was characterized by XPS; the high-resolution C1s spectrum is displayed in Fig. 4.35a. As seen, the spectrum exhibits a typical C1s asymmetric line-shaped graphene peak at $\sim 284.5\text{eV}$, which confirms the growth of graphene. The binding energy of the graphene peak is in agreement with previous reports [100,106,108]. In addition, the absence of a C1s peak at lower binding energy indicates the lack of Ge-C bonding. However, some peaks at higher bonding energies $\sim 285.0\text{eV}$ (C–H), $\sim 286.0\text{eV}$ (C–O), $\sim 287.0\text{eV}$ (C=O) and $\sim 289.0\text{eV}$ (O–C=O) due to adventitious contaminations can also be observed. Besides, the quality of the as-deposited graphene layers was also checked by Raman spectroscopy. A typical Raman spectrum of graphene comprises three- D, G, and 2D Raman bands, as shown in Fig. 4.35b. One can notice that the D peak that appears due to intervalley scattering induced by a defect exhibits negligible intensity ($I_D/I_G \sim 0.05$) and thereby demonstrating the growth of high-quality graphene.

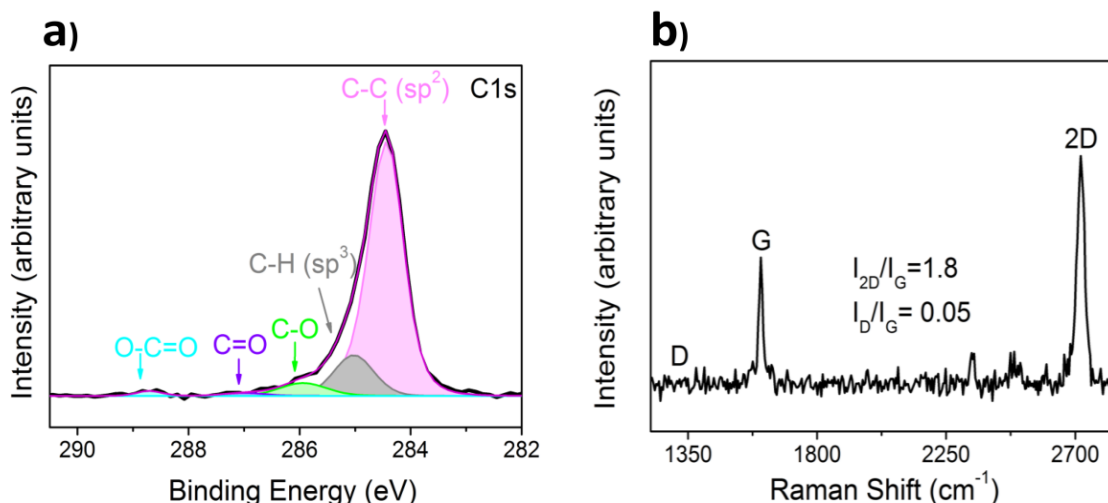


Fig. 4.35. (a) XPS C1s and (b) Raman spectra of as-deposited graphene on Ge(110).

In order to further evaluate the density of defects in graphene, a micro Raman mapping over the area of $10 \times 10\mu\text{m}$ has been performed. The histogram in Fig. 4.36a indicates that the

average value of the D/G intensity ratio is about 0.06. This is in agreement with the previous works where graphene grown on Ge(110) exhibited a lower density of defect (ID/IG= ~0.03) [51,109]. In contrast, graphene grown on Ge(001) exhibits a higher D to G ratio (from 0.1 to 0.7) that is responsible for the polycrystalline nature of graphene [108,110,111]. Hence, the lower density of defects in the graphene films obtained in this work could be an indication of single-crystal graphene growth.

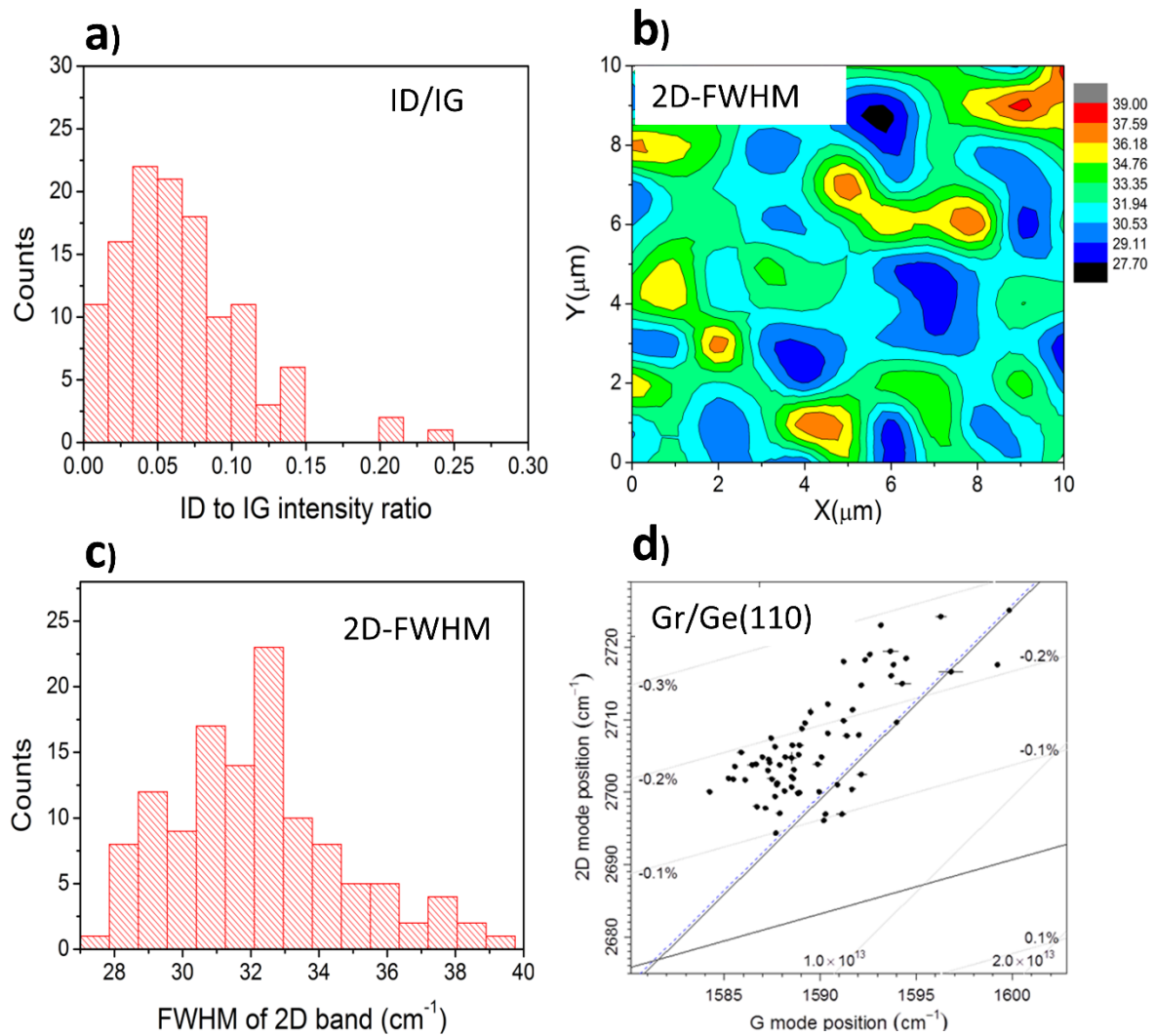


Fig. 4.36. Raman analysis: (a) histogram of the ID/IG intensity ratio, (b) micro-Raman mapping of the 2D-FWHM, (c) histogram of the 2D-FWHM, and (d) 2D versus G peaks position.

In addition to the ID/IG ratio, the thickness of the graphene film was also determined based on the FWHM of the 2D band. A micro Raman mapping of the FWHM of the 2D is provided in Fig. 4.36b. It was observed that the width of the 2D band lied within the range of 28 to 39 cm^{-1} . The histogram in Fig. 4.36c demonstrates that the average value of the 2D-FWHM was about 32 cm^{-1} , indicating the growth of monolayer graphene. On the other hand, the higher range of 2D-FWHM (30–50 cm^{-1}) and hence the growth of thicker graphene is reported on Ge(001) [108,110,111].

Furthermore, the strain and doping levels in graphene were estimated from the position of the 2D and the G bands. Fig. 4.36d depicts the distribution of the 2D versus the G modes positions. Results indicated that the charge doping in graphene is almost negligible (0.1 ± 0.1) 10^{13}cm^{-2} . Also, a redshift in the 2D band position was observed, indicating the presence of compressive strain in graphene. Assuming that the strain is biaxial, it can be estimated to approximately $\sim -0.19\%$. It is worth mentioning here that the obtained values of strain and doping levels in graphene grown in this thesis work are lower than that of graphene grown on Ge(001), where strain and doping levels were found to be $\sim -0.3\%$ and $\sim 2 \times 10^{13}\text{cm}^{-2}$, respectively [100,103,111].

In the next step, the morphological properties of graphene/Ge(110) were investigated with the help of SEM and AFM. In Fig. 4.37a, the SEM micrograph demonstrates the uniform distribution of graphene on Ge(110). Interestingly, the Ge(110) surface morphology underneath the graphene layer did not reconstruct into nano-facets, as evident in the AFM topography (Fig. 4.37b). This is opposite to the morphological behavior of (001) orientated Ge that reconstructs into (107) facets during the graphene growth process [104,111].

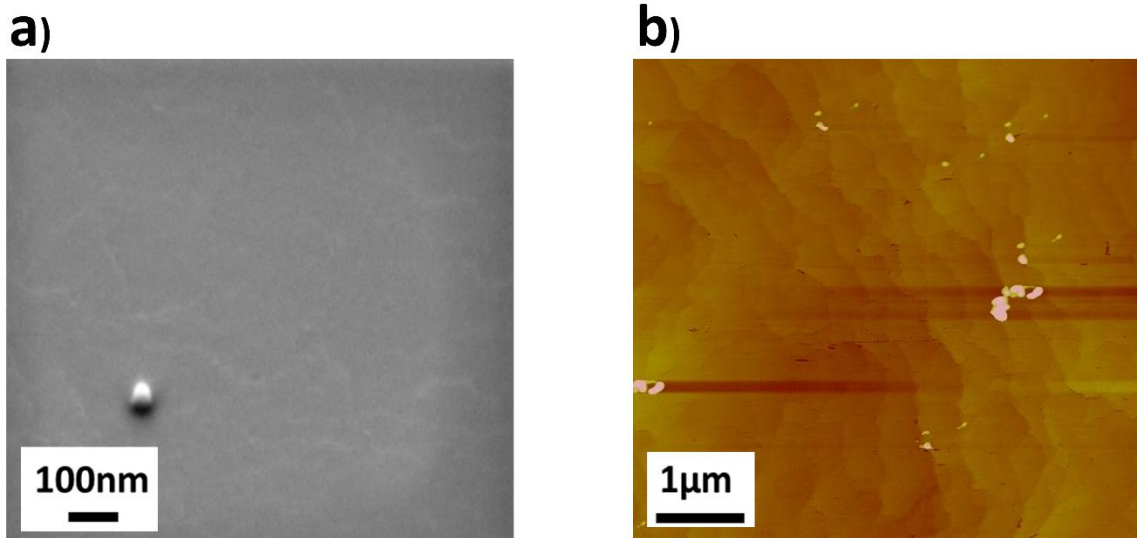


Fig. 4.37. (a) SEM and (b) AFM micrographs of the graphene grown on Ge(110).

As discussed in section 4.2, graphene-induced faceting of Ge(001) is likely to be initiated when long hydrocarbon polymers attach to the surface of Ge(001) along $\langle 010 \rangle$, i.e., along the direction in which the facet ridges will then be formed. The attachment of graphene to the Ge surface may then pin the motion of surface steps, and hence a facet appears there. It is expected that the facets become stabilized energetically during the growth process as a faceted surface provides more area for graphene growth in comparison to a flat surface. On the contrary, a similar faceting may be suppressed on Ge(110). Based on the computed surface energies of Ge faces, one may suppose that faceted structures cannot be stabilized energetically on Ge(110). While the surface energy difference between Ge(001) and Ge(107) is relatively small (0.022 J/m^2), the surface energy of Ge(110) is already very low by itself (1.008 J/m^2), and the energy difference between Ge(110) and Ge(107) becomes 0.066 J/m^2 , three times more than between Ge(001) and Ge(107) [112].

Lastly, graphene was transferred from Ge(110) onto the SiO_2/Si substrates by applying the same method used in section 4.2 in order to check its electrical properties. After the transfer step, the samples were investigated by performing AFM and Raman analysis. AFM results

indicated that the transferred graphene is free from any types of cracks and holes (Fig. 4.38a). However, wrinkles that arise due to the opposite polarity of the thermal expansion coefficients of graphene and underlying Ge can be observed. Raman spectrum is shown in Fig. 4.38b. A defect or D mode which is attributable to the transfer process can be seen, indicating that further optimization of the transfer step is required.

Furthermore, the electrical properties of graphene were determined from Hall measurements. Results showed that graphene exhibits superior electrical mobility $\mu \approx 2700\text{cm}^2/\text{Vs}$ and lower sheet resistance $R_s \approx 800\Omega/\text{sq}$ as compared to graphene transferred from Ge(001).

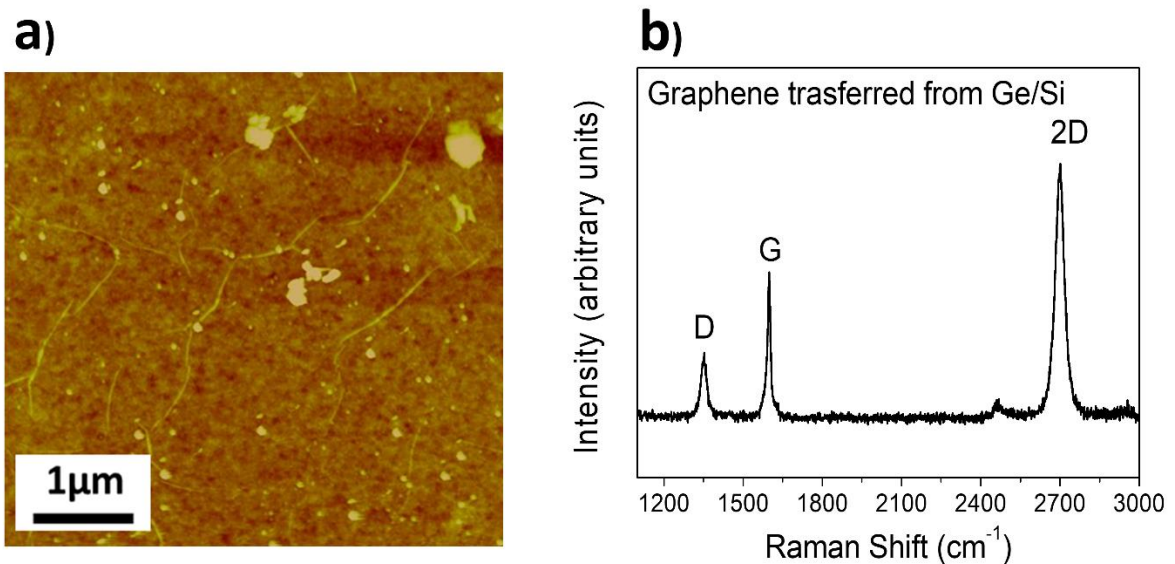


Fig. 4.38. Graphene transferred from Ge onto SiO₂/Si (a) AFM image and (b) Raman spectrum.

Summary

In this PhD work, the growth of graphene on 200mm Ge/Si(110) wafers was performed by the CVD method. Uniform monolayer graphene can be grown over large areas, as verified by Raman spectroscopy. The low density of defects indicated the high quality of the obtained graphene. Indeed, Hall measurements showed that graphene exhibits high

electrical mobility ($\mu \approx 2700\text{cm}^2/\text{Vs}$) and low sheet resistance ($R_s \approx 800\Omega/\text{sq}$). From SEM and AFM investigations, it was found that Ge(110) layer underneath the grown graphene remains flat, whereas Ge(001) is composed of (107) facets. The graphene-induced pinning of Ge steps is responsible for the formation of (107) facets. The non-faceted morphology of Ge(110) underneath the graphene could be attributed to lower surface energies of Ge(110) than that of Ge(001) and (107).

4.4. Oxidation behavior of graphene/Ge(001) versus graphene/Ge(110)

After determining the properties of as-deposited graphene/Ge(001) and Ge(110) systems, the next step was to investigate their interfacial properties. For this purpose, the graphene/Ge samples were kept in the air for more than 7 months, and their interfaces were carefully monitored with the help of various characterization techniques.

Influence of atmospheric oxygen on the properties of graphene/Ge Systems

Firstly, the surface morphology of the as-deposited graphene/Ge systems was investigated by SEM; results are shown in Fig. 4.39. As seen, Ge(001) underneath graphene reconstructs into hills and valleys (Fig. 4.39a).

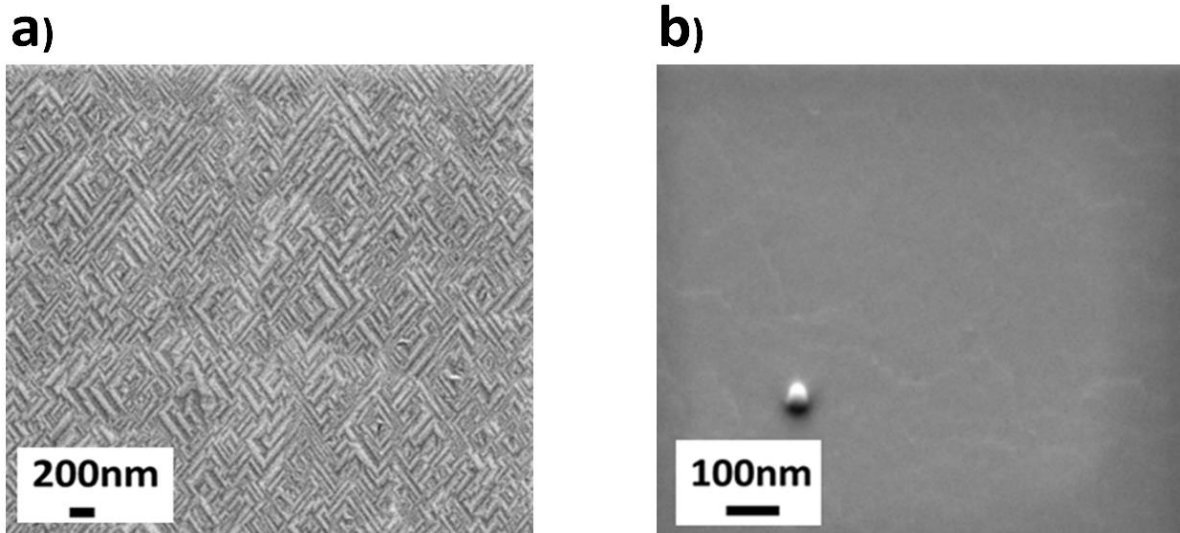


Fig.4.39. SEM images of the as-deposited graphene on (a) Ge(001) and (b) Ge(110) [adopted from Ref. 113b].

This is attributed to the growth of graphene [100,104,111,113a]. Compared to Ge(001), the morphology of Ge(110) underneath graphene is composed of steps or terraces, as can be seen in Fig. 4.39b [51].

Furthermore, XPS was performed to check the chemical status of the as-deposited graphene/Ge systems. In Figs. 4.40a and b, the C1s spectra of the as-deposited graphene/Ge(001) and Ge(110) are denoted by black lines. Additionally, the fitted C1s spectra are provided in the insets of Figs. 4.40a and b. One can notice a graphene peak at $\sim 284.5\text{eV}$, which agrees with the previous reports [100,106,108,113c]. Besides, several other peaks, such as sp^3 (C–H), C–O, C=O, O–C=O, can also be observed at binding energies of $\sim 285.0\text{eV}$, $\sim 286.0\text{eV}$, $\sim 287.0\text{eV}$, and $\sim 289.0\text{eV}$, respectively. These peaks are attributed to adventitious contaminations (insets in Figs. 4.40a and b) [114]. In XPS O1s spectra, the peaks corresponding to adventitious contaminations C=O ($\sim 532.0\text{eV}$), C–O ($\sim 533.5\text{eV}$), and O–C=O ($\sim 535.5\text{eV}$) were also recorded (Figs. 4.40c and d, black lines). In Ge2p spectra, on the other hand, only one characteristic peak was observed at $\sim 1217.5\text{eV}$, which is attributed to elemental Ge [115,116], as shown in Figs. 4.40e and f (black lines). As no peaks related to Ge oxides in Ge2p spectra were detected, the interface between graphene and Ge was oxygen-free.

After initial investigations of the as-deposited systems, these samples were stored in the open air for more than 7 months to examine the impacts of atmospheric oxygen on the graphene/Ge interface. Therefore, the XPS core level C1s, O1s, and Ge2p spectra were carefully monitored on a daily basis. In Fig. 4.40, only selected XPS spectra are shown for simplicity reasons. The evolution of C1s spectra showed that although graphene peak (sp^2) remained the main component, the intensity of the peaks corresponding to adventitious carbon (at binding energy between 285 and 289eV) increased with time (Figs. 4.40a and b).

A similar trend was also noted in O1s spectra, where the peaks related to the adventitious contaminations gained intensity with time. Besides, a small O1s peak at $\sim 531.1\text{eV}$ was measured in O1s spectra after 18 hours of ambient exposure, as shown by the magenta line (Fig. 4.40c). The deconvolution of O1s spectrum using the Gauss-Lorentzian line shape demonstrated the presence of four peaks GeO (+2), C=O, C–O, and O–C=O at binding energies of $\sim 531.1\text{eV}$, $\sim 531.9\text{eV}$, $\sim 533.2\text{eV}$, and $\sim 535.0\text{eV}$, respectively (inset in Fig. 4.40c). It was noticed that the corresponding Ge2p spectrum in Fig. 4.40e (magenta line) also contained Ge–O bonds. The peak fitting analysis of the Ge2p spectrum (inset in Fig. 4.40e) indicates the presence of elemental Ge ($\sim 1217.5\text{eV}$) and GeO ($\sim 1219.5\text{eV}$). The existence of the Ge–O peak shows that Ge(001) substrate underneath graphene started to oxidize during only a short time exposition to air (i.e., 18 hours). In addition to GeO and elemental Ge peaks, a GeO₂ (+4) peak was also recorded on day 2 (Fig. 4.40e, orange line), indicating the further oxidation of Ge. With the passage of time, the combined intensity of the GeO and GeO₂ peaks increased, with GeO₂ gradually taking over. At last, the GeO almost converted into GeO₂ after 7 months.

In compare to graphene/Ge(001), the graphene/Ge(110) sample showed different behavior upon air exposure. It was found that graphene/Ge(110) interface remained oxygen-free until day 12 as no signals related to Ge oxides (GeO and GeO₂) were recorded in XPS O1s and Ge2p spectra (Figs. 4.40d and f). However, a small peak at the binding energy of $\sim 531.1\text{eV}$ appeared in the O1s spectrum on day 12 (Fig. 4.40d, purple line). The fitted O1s spectrum is comprised of GeO ($\sim 531.1\text{eV}$), C=O ($\sim 532.0\text{eV}$), C–O ($\sim 533.2\text{eV}$), and O–C=O ($\sim 535.0\text{eV}$) peaks, as shown in the inset of Fig. 4.40d. The corresponding Ge2p spectrum also contained two peaks related to elemental Ge ($\sim 1217.5\text{eV}$) and GeO ($\sim 1219.5\text{eV}$) (inset in Fig. 4.40f). The GeO signal underneath the grown graphene layer indicated the minor

oxidation of Ge (110). Upon further exposure (i.e., on day 15), a GeO₂ signal in addition to GeO and Ge peaks was recorded (Fig. 4.40f, green line).

It was observed that the intensity of the XPS peaks corresponding to Ge oxides (GeO and GeO₂) increased upon further air exposure. However, unlike the air-exposed graphene/Ge(001) system, GeO did not convert into GeO₂ after 7 months. The comparison of the air-exposed graphene/Ge(001) and graphene/Ge(110) shows that the oxidation of Ge(001) starts only after 18 hours of air exposure. On the other hand, Ge(110) layer underneath graphene remained oxygen-free for several days (at least 12 days). This means that the oxidation of Ge(110) was slower than that of Ge(001). This is in agreement with the literature reports where graphene/Ge(110) systems showed more resistance against oxidation in comparison with graphene-covered Ge(001) and Ge(111) layers [114,116]. Furthermore, it was also observed that the spectra measured after 7 and 8 months acquired almost similar intensity. Hence, further XPS experiments were not performed, but one should not neglect the further oxidation of graphene-covered Ge.

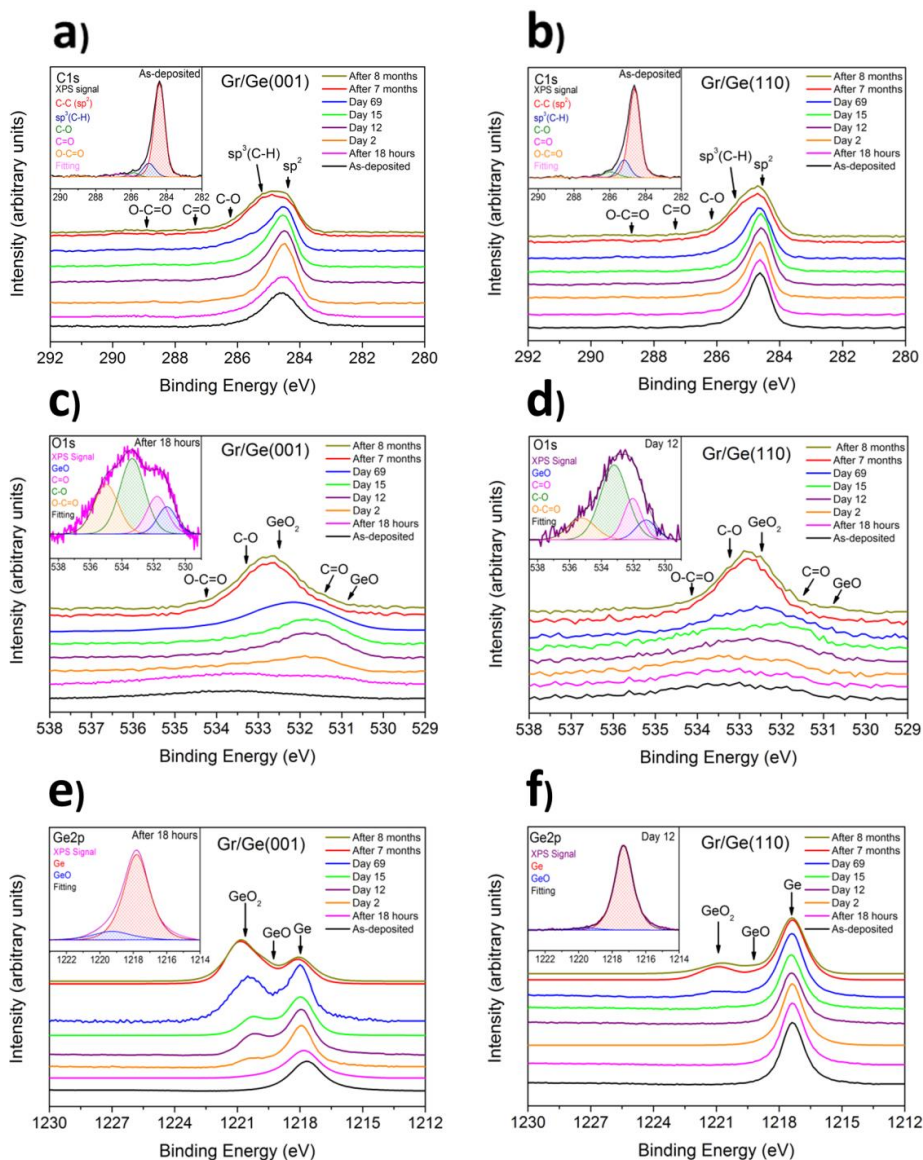


Fig. 4.40. XPS spectra of graphene/Ge(001) (a) C1s, the inset shows the spectra of as-deposited graphene (c) O1s and (e) Ge2p spectra, the insets show the spectra taken after 18 hours. XPS spectra of graphene/Ge(110) (b) C1s, the inset shows the spectra of the as-deposited graphene (d) O1s and (f) Ge2p, the insets show the spectra taken after 12 days. Black lines show the spectra of the as-deposited graphene/Ge systems; the spectra were taken as a function of time are indicated by magenta lines (after 18 hours), orange lines (day 2), purple lines (day 12), green lines (day 15), blue lines (day 69), red lines (after 7 months), and dark yellow lines (after 8 months) [adopted from Ref. 113b].

In the next step, the thickness of oxide films present at the interface between graphene and Ge was determined on the basis of the intensity ratio of the substrate (I_s) and the oxide (I_o) peaks for Ge2p core levels. The following formula was used in order to calculate the overall thickness of the oxide (t_{ox}) [115b]:

$$t_{ox} = \lambda \cos\theta \ln\left(\frac{I_o I_s^\infty}{I_s I_o^\infty} + 1\right) \quad 4.2$$

where λ is the attenuation depth. The value of λ is 0.9nm for Ge2p [115b]. The angle between the surface normal and the emission directions is denoted by θ . In these experiments, the value of θ was 45°. Further, the intensity of oxide-free Ge samples and the intensity of infinitely thick oxide are denoted by I_s^∞ and I_o^∞ , respectively. This formula assumes that the oxide films grow via a layer-by-layer growth mode.

In Fig. 4.41, one can see that at day 0, the surface of Ge films underneath the as-deposited graphene is free from oxide. But the interface between graphene and Ge started to oxidize slowly upon air exposure. Fig. 4.41 indicates that Ge(001) oxidizes much faster as compared to Ge(110). After 18 hours, the thickness of oxide on Ge(001) exceeds 0.3nm. The oxide on Ge(110), on the other hand, appears after the incubation time τ of nearly a week and needs about a year to reach the thickness of 0.3nm. With time, mature oxidation proceeds linearly for both samples, as shown in Fig. 4.41a, demonstrating the reaction-limited growth. In contrast, the initial growth may follow the square root dependence (Fig. 4.41b), indicating the diffusion-limited growth.

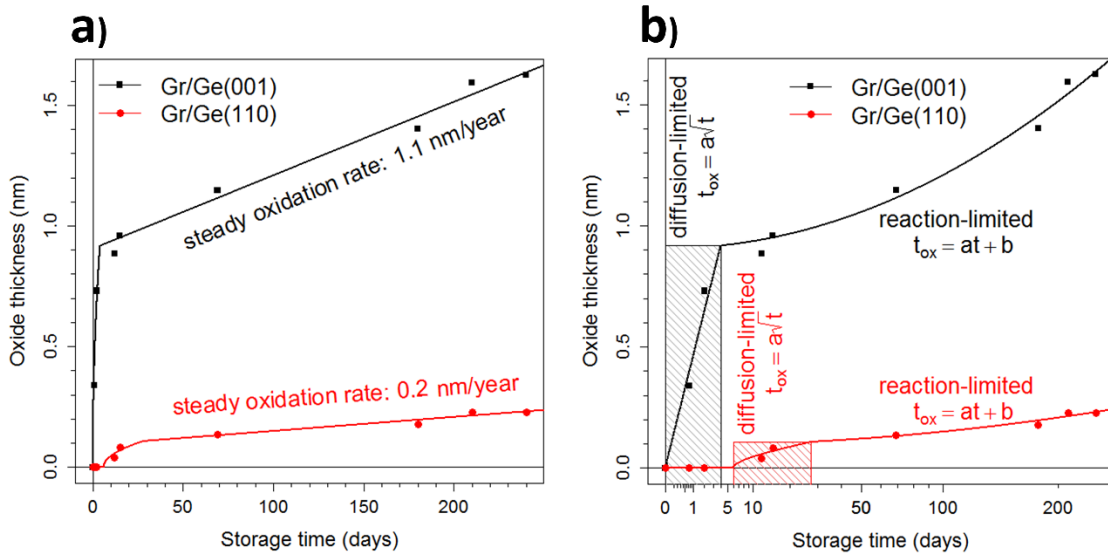


Fig. 4.41. Oxide thickness t_{ox} as a function of storage time. Equation 4.2 was used to calculate t_{ox} from the measured XPS peak intensities. The solid lines represent the least mean square fit. (a) Linear time scale. (b) Square-root time scale; the regions of approximate square root and linear growth are indicated as diffusion-limited and reaction-limited regions [adopted from Ref. 113b].

After seven months of air exposure, SEM analysis was repeated to investigate the impact of atmospheric oxygen on the morphology of the graphene/Ge systems. It can be seen in Fig. 4.42a that the typical faceted surface of graphene-covered Ge(001) substrate was distorted. Like Ge(001), the surface morphology of the Ge(110) below the graphene film was also distorted (Fig. 4.42b). A comparison of the SEM images of the air-exposed (Fig. 4.42) and the as-deposited graphene/Ge sample (Fig. 4.39) shows that the prolonged exposure to air has indeed impacted the morphology of the systems. These observations agree with a recent literature work where authors observed the blurry and distorted surface morphology of graphene-covered Ge(001) and attributed it to Ge oxidation [117].

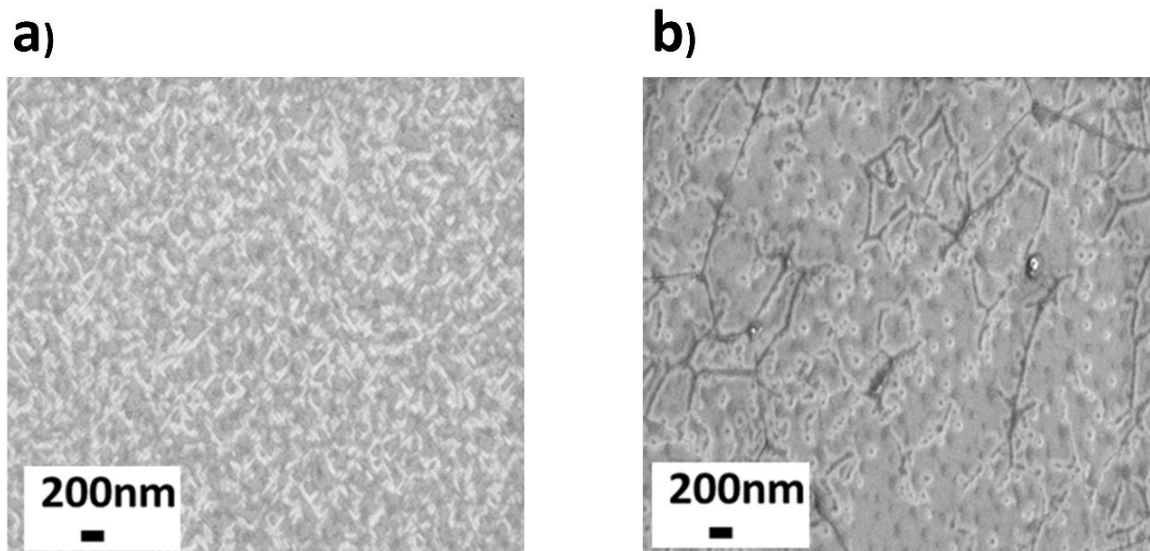


Fig. 4.42. SEM images of air-exposed (a) graphene/Ge(001) and (b) graphene/Ge(110) [adopted from Ref. 113b].

The impacts of interfacial oxygen on the properties of graphene/Ge systems were checked by Raman spectroscopy. Micro-Raman mappings have been conducted over $10 \times 10 \mu\text{m}^2$ areas; results are provided in Fig. 4.43. It has been reported that by noting the shifts in the positions of the Raman 2D and G bands, one can evaluate the level of doping and strain in graphene [102]. In this PhD work, the strain and doping levels in graphene study were therefore estimated from the shifts in Raman bands (2D and G bands) positions by applying the vector decomposition method. The plots of the 2D versus the G bands peak positions for the as-deposited graphene on Ge(001) are represented by black data points in Fig. 4.43a. It can be seen that the as-deposited graphene is under compressive strain, and its value is about $(-0.03 \pm 0.02)\%$, while the doping level is $(1.4 \pm 0.2)10^{13}\text{cm}^{-2}$. In the case of the as-deposited graphene/Ge(110), the doping seems to be negligible $(0.1 \pm 0.1)10^{13}\text{cm}^{-2}$. However, the strain in graphene on Ge(110) is extremely compressive $(-0.19 \pm 0.05)\%$ in comparison with that of graphene grown on Ge(001), as shown in Fig. 4.43b (black data points). Besides, a small offset to the left of the strain axis can be observed and is indicated

by black arrows (Fig. 4.43b). This could be due to the substrate-induced screening effect [118,119].

Furthermore, it was observed that the strain in graphene reduced from $(-0.19 \pm 0.05)\%$ to $(-0.08 \pm 0.03)\%$ after exposing the graphene/Ge(110) system to the air for seven months, as can be seen in Fig. 4.43b (black vs. red data points). Similarly, a small reduction in the strain from $(-0.03 \pm 0.02)\%$ to $(+0.01 \pm 0.02)\%$ was recorded for the air-exposed graphene/Ge(001) system (Fig. 4.43a, black vs. red data points). In addition to strain, one can notice that the doping level has also decreased by about a quarter or by $0.4 \times 10^{13}\text{cm}^{-2}$, as shown in Fig. 4.43a.

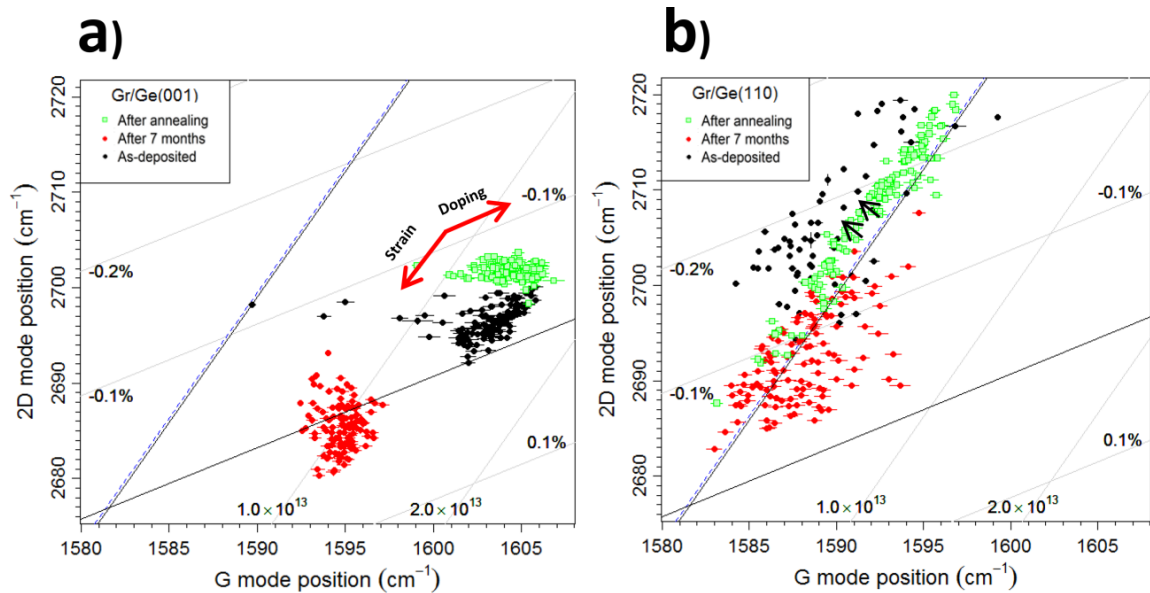


Fig. 4.43. 2D/G plots of (a) graphene/Ge(001) and (b) graphene/Ge(110). Black, red, and green points denote data from samples: as-deposited, stored for 7 months in ambient air, and annealed [adopted from Ref. 113b].

Reversibility of graphene/germanium systems

Finally, the reversibility of the oxidation process was checked. For that reason, both the air-exposed graphene/Ge(001) and Ge(110) systems were annealed at 850°C for 4 hours in vacuum ($5.8 \times 10^{-7}\text{mbar}$). After annealing, the samples were again examined by Raman

spectroscopy, XPS, and SEM. Raman analysis showed that the strain in graphene deposited on Ge(001) and Ge(110) was $(-0.06 \pm 0.01)\%$ and $(-0.18 \pm 0.04)\%$ (green data points in Figs. 4.43a and b). By comparing the 2D/G maps of the annealed and as-deposited graphene/Ge samples (Figs. 4.43a and b, green vs. black data points), one can see that the strain and doping levels are almost the same, indicating that the initial state of the graphene/Ge systems has been restored. Besides, the Raman point spectra of as-deposited, air-exposed, and annealed graphene/Ge(001) and (110) samples are given in Fig. 4.44. As seen, the Raman 2D, G, and D bands are red-shifted due to air exposure. However, these Raman bands have restored their original position (as-deposited) after annealing.

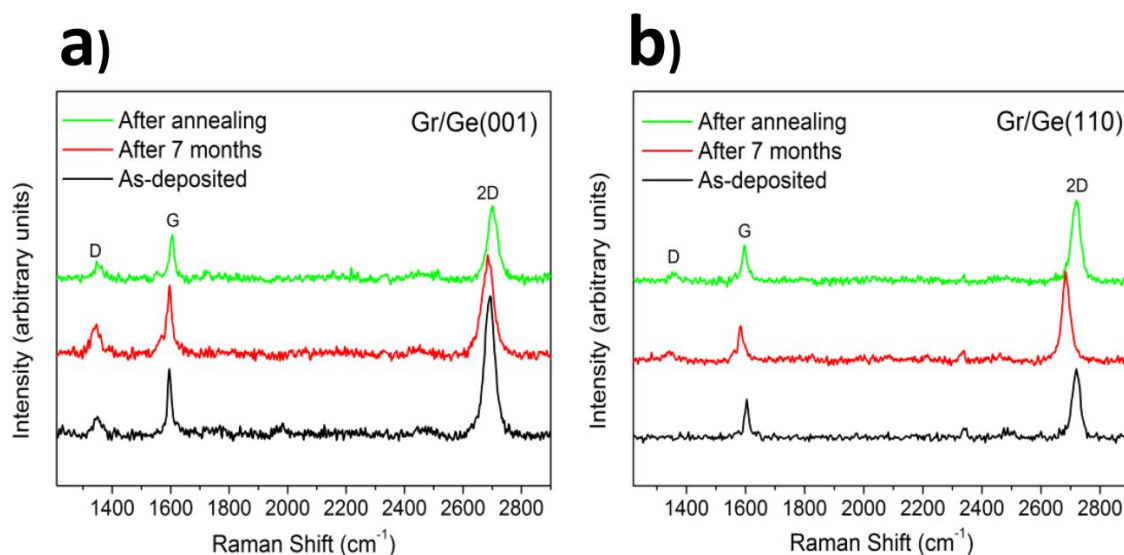


Fig. 4.44. Raman spectra of graphene on (a) Ge(001) and (b) Ge(110). The spectra collected after graphene deposition, 7 months, and annealing are indicated by the black, red, and green colors, respectively [adopted from Ref. 113b].

XPS was performed in order to further check the influence of annealing. In Fig. 4.45, the Ge2p and O1s spectra of the annealed (top rows), the air-exposed (middle rows), and the as-deposited (bottom rows) graphene/Ge systems are depicted. The presence of a single Ge peak at $\sim 1217.5\text{eV}$ in Ge2p spectra demonstrated that annealing had removed the (+2) GeO

and (+4) GeO_2 (Figs. 4.45a and b, top rows). The absence of Ge oxides (GeO and GeO_2) clearly indicates that high temperature annealing has removed oxygen from both graphene/Ge systems. In addition to $\text{Ge}2p$ spectra, no oxide signals were recorded in $\text{O}1s$ spectra (Figs. 4.45c and d, top rows) and hence further confirmed the removal of oxygen. Regarding $\text{C}1s$ spectra (not shown here), only graphene peak was measured after annealing, while the features corresponding to adventitious carbon were not detected.

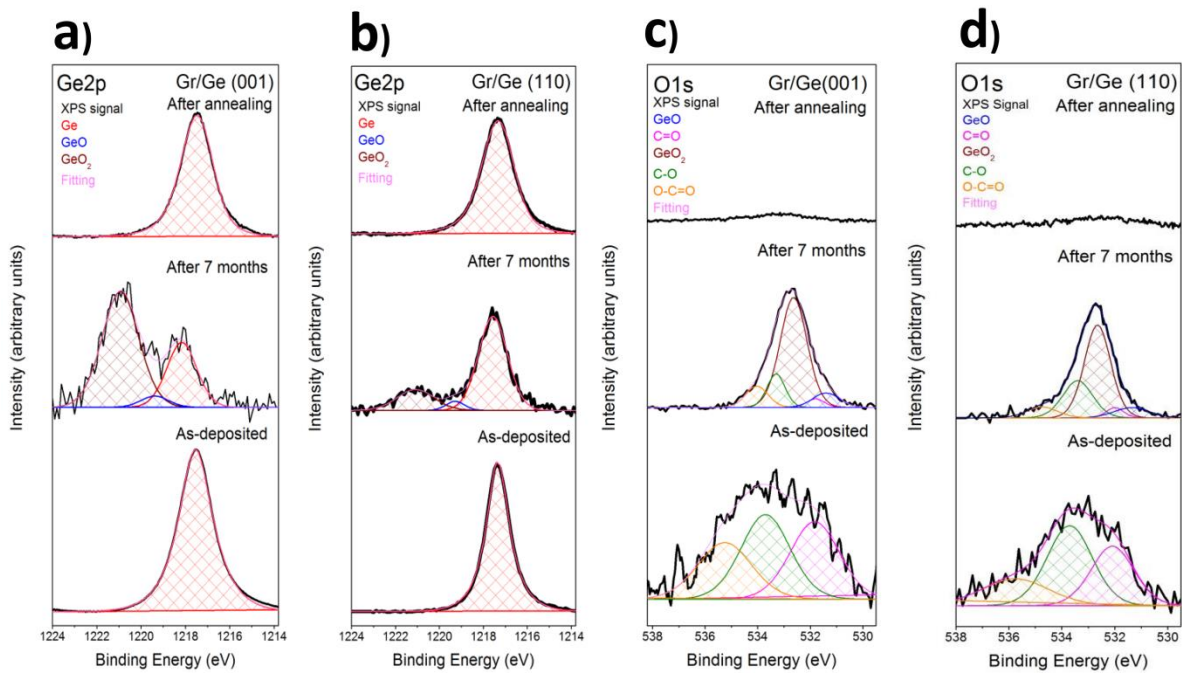


Fig. 4.45. XPS study: $\text{Ge}2p$ spectra of (a) $\text{Ge}(001)$ and (b) $\text{Ge}(110)$, $\text{O}1s$ spectra of (c) $\text{Ge}(001)$ and (d) $\text{Ge}(110)$. The spectra collected after annealing the systems (top rows), after being exposed to air (middle rows) and in the as-deposited state (bottom rows) [adopted from Ref. 113b].

In the last step, the effect of the annealing on the morphology of both graphene/Ge systems was also examined. The SEM image shown in Fig. 4.46a indicates the faceted surface of $\text{Ge}(001)$ underneath the graphene film. As explained in a literature work, the growth of graphene is the cause of the faceted surface of $\text{Ge}(001)$ [104]; hence, it is another indication that graphene/ $\text{Ge}(001)$ has restored its as-deposited (i.e., initial) state. Similar to annealed

graphene/Ge(001) system, the morphology of the graphene/Ge(110) system has also been recovered, as shown in Fig. 4.46b. However, some additional features in the form of grain boundaries are now visible, which need further investigation.

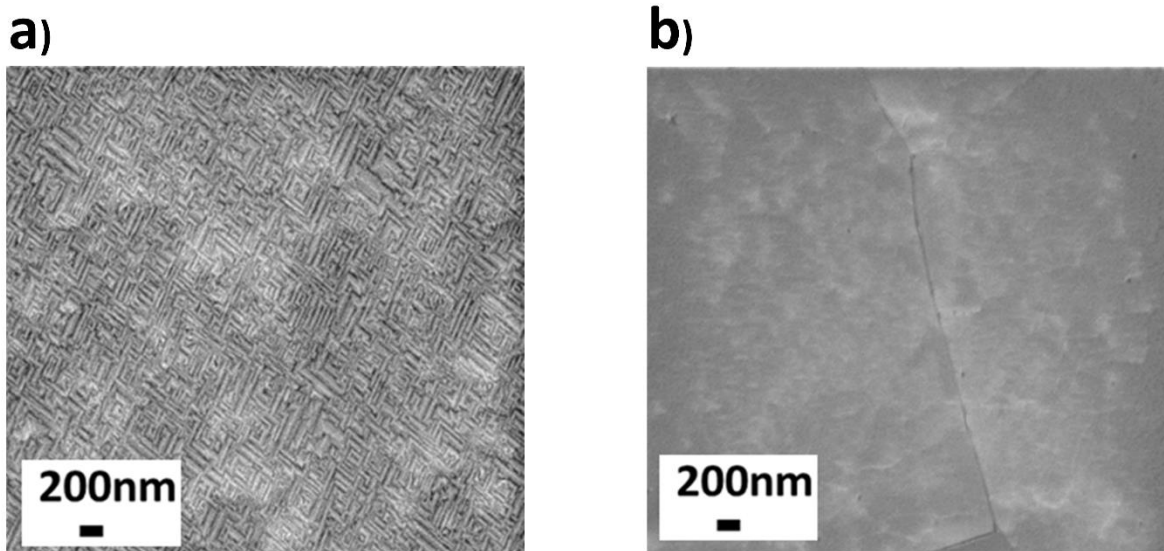


Fig. 4.46. SEM images were taken after annealing the graphene/Ge (a) (001) and (b) (110) [adopted from Ref. 113b].

Discussion

Based on all observations and results obtained during this study, some possible explanations and speculations can be provided for the oxidation of Ge(001) and Ge(110) layers underneath the graphene. It has been reported that graphene coating can provide an effective barrier against oxidation; therefore, it is used to protect various metals, such as Cu [120–124], Ni, Co, Fe, and Pt [125], from oxidation. According to literature reports, the barrier efficiency of graphene depends on several factors, such as the sizes of graphene grains or the number of defects [114,116,123,126–129], the interactions between substrate and graphene [114,125], and the layer thickness of graphene [123,130]. It is known that graphene films grown by the CVD method are not perfect as they contain many defects in the form of Stone–Thrower–Wales defects, single and di-vacancies, nano-pores, wrinkles,

cracks, and grain boundaries [10]. As a pristine graphene film is impermeable to even small atoms like He and H [131,132], therefore, these structural defects are considered to be the possible pathways for oxygen to reach the underlying substrates. It has already been reported that the oxidation of graphene-covered Ge substrates occurs through point defects in graphene [116]. Jacobberger et al. have mentioned that different levels of Ge oxidation may indicate that the oxidation of Ge occurs via both grain boundaries and point defects in graphene [114]. However, the authors also described that it is not easy to determine the exact type of the atomic-scale defects at which Ge preferentially oxidizes. Likewise, some other literature works reported that the graphene grain boundary defects are responsible for Ge oxidation [106,111,117]. Based on the observations of this PhD work, it is assumed that the possible mechanism behind the oxidation of Ge(001) and Ge(110) below graphene could be the penetration of oxidizing species through grain boundary and the defects induced by grain boundaries. However, faster oxidation of graphene-covered Ge(001) may indicate that the diffusion of oxygen on this orientation is more efficient than on Ge(110). In other words, graphene film grown on Ge(001) contains many grain boundaries and/or other defects through which oxygen can penetrate below the graphene and causes the faster oxidation of underlying Ge(001). This assumption directly correlates with the Raman analysis. According to which, graphene grown on Ge(110) has a lower number of defects ($ID/IG \approx 0.05$) as compared to the ones grown on Ge(001) ($ID/IG \approx 0.3$), where the ID/IG ratio represents the intensity ratio of D and G peaks, respectively. As the coalescence of differently oriented graphene domains is the cause of grain boundary defects, hence it is assumed that graphene films consisting of smaller grains will have more grain boundaries. In order to prove this assumption, the graphene grain sizes were calculated from the ID to IG intensity ratios by using the following formula [114]:

$$L_{\text{grain}} = 2.4 \times 10^{-10} \lambda^4 \left(\frac{I_D}{I_G} \right)^{-1} \quad 4.3$$

In this formula, λ (nm) represents the wavelength of the laser used ($\lambda = 532\text{nm}$), and I_D/I_G indicates the intensity ratio of the Raman D and G bands. These calculations showed that graphene grain size L_{grain} (nm) was larger ($\sim 400\text{nm}$) for the films deposited on the Ge(110) substrate, whereas it was smaller ($\sim 80\text{nm}$) on Ge(001). It has been reported that the larger grains indeed provide an efficient diffusion barrier than smaller grains [123].

In this PhD work, the immediate oxidation of Ge(001) upon a short-term (18 hours) air exposure is a clear indication that the grain boundaries in the as-deposited graphene on this orientation are already permeable to the oxidation species. In Fig. 4.41, the measured time sequence of oxide thickness shows that the growth of oxide is initially controlled by diffusion of the oxidizing species (Fig. 4.41b), originating from a random walk. In a diffusion-controlled mechanism, the thickness of oxide is proportional to the square root of time [133]. Thus, it can be assumed that after passing through graphene at some fixed, the oxidizing species reach the graphene/Ge interface [113b]. These species, then, diffuse along with the interface and/or diffuse across the oxide to the unoxidized substrate, where they readily react and become immobilized [113b].

The diffusion-controlled growth changes into steady oxidation (typical for reaction-controlled mechanisms) after keeping the Ge(001) sample in the air for about a week. The variations between the initial and mature growth kinetics are not unusual [134]. However, it is informative that reaction-limited growth follows diffusion-limited growth. Specifically, the steady growth rate may suggest that when a surface is covered by graphene, the flow of the oxidants gets jammed at the entry points or defective graphene sites [113b]. But it is the slowest process that always limits the overall rate. The growth rate is limited by the

diffusion of the injected oxidants, and it even slows down over time. Hence, the observation that the entry point began to limit the rate means that the maximal oxidant flux supported by the oxidant source must have decreased, or the chemistry of injected species have changed to such that they diffuse faster [113b]. The graphene's permeability for oxidants may reduce over time, if some important entry points get blocked, for instance, by organic molecules. Alternatively, the molecules might have agglomerated into clusters that separate the interface from the air and act as in-diffusion sources of oxygen [113b]. At this point, the in-diffusion rate relies on (i) the permeability of graphene grain boundaries (ii) and on the concentration of the oxidants in the cluster. Additionally, the oxidizing species may also be different from the ones delivered directly from the air. The clusters may dissociate the oxygen-containing molecules so that the transport of oxygen through the oxide may speed up in comparison with the initial phase [113b].

Up to now, the different density of grain boundaries in graphene grown on Ge(001) and Ge(110) is assumed to be the reason for the different oxidation rates of these substrates. Besides, one should also take into account the hypothesis that the oxidation process is also influenced by the strength of the interaction between graphene and the substrate. For example, the stronger interaction between graphene and Ge(110) may be the cause of its slower oxidation, whereas faster oxidation of Ge(001) and Ge(111) [114] would be attributed to a weaker interaction between graphene and Ge(001) [106]. It has already been shown that graphene prevents the oxidation of strongly interacting metals more efficiently than those that interact weakly with graphene [125]. The authors also explained that the graphene decouples from weakly interacting metals upon air exposure due to the intercalation of oxygen. This allows oxygen to access the whole metal surface, speeding up the oxidation process [125]. Lateral oxidation is suppressed when the oxidizing species do

not readily diffuse under the graphene film or when the metal gets easily oxidized [125]. Based on the hypothesis of graphene-substrate interaction, it can be assumed that another reason for the faster oxidation of Ge(001) could be its weaker interaction with the top graphene layer compared to that of Ge(110).

Summary

In this PhD study, the oxidation behaviors of graphene-covered Ge(001) and Ge(110) substrates were investigated using various characterization methods. XPS results showed that the Ge(110) oxidation began after an incubation period of almost two weeks, and it acquired linear kinetics within a few days or weeks. Unlike Ge(110), the oxidation of Ge(001) started during 18 hours of exposition to air. It was found that the initial oxidation on both Ge(001) and Ge(110) films underneath graphene is limited by diffusion. In the reaction-limited region (linear regime), the rate of Ge(001) oxidation was five times higher in comparison to that of Ge(110). After seven months of air exposure, the oxide thickness was measured to be seven times higher on Ge(001) than on Ge(110). These differences were due to different areal density of graphene grain boundaries by which the oxidizing species reach the underlying Ge substrate and oxidize it. Raman analysis showed that the long-term exposure to air impacted the properties of graphene as strain in graphene reduced from $(-0.19 \pm 0.05)\%$ to $(-0.08 \pm 0.03)\%$ on Ge (110) and from $(-0.03 \pm 0.02)\%$ to $(+0.01 \pm 0.02)\%$ on Ge(001). It was also observed that the long-time ambient exposure also distorted the morphology of both the systems, as determined by SEM.

The reversibility of the oxidation process was also checked in this PhD work by annealing the graphene/Ge systems in vacuum for four hours. After annealing, no oxide signal in O1s and Ge2p XPS spectra could be measured, indicating the removal of oxides from the graphene/Ge systems. From Raman and SEM studies, it has been found that the removal of

interfacial oxygen has restored the graphene/Ge to their initial as-deposited states. The findings of this study indicate though exposition to air causes the oxidation of graphene-covered Ge(001) and Ge(110), the oxidation of Ge is a reversible process.

PART IV

CONCLUSIONS & OUTLOOK

CHAPTER 5

5. CONCLUSIONS & OUTLOOK

Recalling the main objective of this thesis, the idea was to obtain large-area and high-quality graphene. In this PhD study, 8-inch sized substrates like epitaxial Ge on Si and polycrystalline Ni on Si were employed to grow graphene by the CVD method. This work focuses on the investigations of various nucleation and growth mechanisms, substrate/graphene interfaces, and effects of different substrate orientations on graphene properties. The properties of the obtained graphene films were then examined using various microscopic and macroscopic characterization techniques. The main conclusions extracted from this work could be summarized as the following:

5.1. Conclusions

- On polycrystalline Ni, larger Ni(111) grains or flat surface morphology of Ni is the main requirement for controlling graphene's thickness uniformity. Hence, a systematic study based on different surface pretreatments of Ni has been performed in order to prepare its surface before the growth of graphene. It was found that annealing the Ni films in hydrogen ambient prior to graphene growth resulted in larger Ni(111) grains up to 6 microns that caused the growth of thinner graphene. In contrast, thicker graphene films were obtained when Ni films were annealed in vacuum and are attributed to smaller Ni grains (up to 3 microns). Hence, this study concludes that the annealing of Ni in hydrogen ambient before graphene growth is an essential step towards the growth of thinner graphene.

- With the assistance of Ni, graphene growth between Ni bars and underneath Ni directly on silicon dioxide was also attempted. For this purpose, two different types of Ni-structured wafers were used. It was found that the formation of graphene-like features, the limited lateral extension of graphene, and the de-wetting of Ni structures make the graphene growth on silicon dioxide a challenge. Hence, further optimization of the process is needed.
- In this PhD work, graphene was also grown on two differently oriented (001) and (110) Ge substrates. Both Ge orientations favored the growth of large-area graphene (8-inch), but the characteristics of grown layers were different. For example, graphene on Ge(110) exhibited a low density of defects ($I_D/I_G = 0.05$), higher mobility values, and is exceptionally strained in comparison to graphene grown on Ge(001). Besides, Ge(110) underneath graphene has a non-faceted surface morphology, whereas the surface of Ge(001) is composed of hills and valley structures. The explanations for the possible mechanisms responsible for the faceted and non-faceted morphology were also provided. Based on the findings of this study, it is concluded that different characteristics of the grown graphene layers could be due to the different surface morphology of the underlying Ge orientation.
- The oxidation behavior of the graphene/Ge (001) and Ge(110) systems was also investigated and compared in this study. It was found that the oxidation rate of graphene-covered Ge(001) substrates is higher than that of graphene-covered Ge(110) layers. These differences could be due to different grain boundary defects in graphene as they allow the oxide species to reach Ge. Also, the negative impacts of interfacial oxygen on the properties of graphene were observed. Both the graphene/Ge systems were thus annealed in order to check the reversibility of the

oxidation process. Results showed the absence of oxide signals in both systems, and therefore they regained their original properties. Based on these findings, it can be concluded that, indeed, exposition to air causes the oxidation of both graphene/Ge(001) and Ge(110) systems. Still, the stability of Ge(110) against oxidation diffusion was higher. In addition, the systems restored their original properties after annealing at higher temperatures.

5.2. Perspectives

Further work towards high-quality graphene growth could be grouped as follows:

- a) CVD processes are strongly affected by various growth parameters, such as temperature, the concentration of precursors, precursors to hydrogen ratio, pressure, etc. Also, using different hydrocarbon sources (CH_4 vs. C_2H_4 vs. C_2H_2) or the application of plasma might significantly modify the growth conditions and, therefore, graphene properties. One of the advantages of using plasma is that graphene could possibly be grown at low temperatures. Therefore, one can see that many possibilities are there to improve the quality of graphene by optimizing various process conditions. Hence, we expect to improve and further develop the graphene growth directly on silicon dioxide, which was only briefly touched on in this work. DFT calculations are also planned in order to understand the growth mechanisms better.
- b) The use of techniques, such as ARPES, STM, LEEM, and LEED, as well as further electrical measurements, would be of interest to investigate the surface morphology, electronic structure, domains, surface transport properties, and quality of the graphene layers. As seen in this work, the graphene/substrate interface quality is very important as it can impact the properties of the graphene layer.

Hence, it would be interesting to investigate the effects of the interfaces between graphene and substrate in more detail.

SCIENTIFIC VISIBILITY

Publications in Peer-reviewed Journals

- **Fatima Akhtar**, Jaroslaw Dabrowski, Marco Lisker, Peter Zaumseil, Sebastian Schulze, Alex Jouvray, Piotr Caban, Andreas Mai, Christian Wenger, Mindaugas Lukosius, TSF 2019, 30, 137565.
- **Fatima Akhtar**, Jaroslaw Dabrowski, Marco Lisker, Yuji Yamamoto, Andreas Mai, Christian Wenger, Mindaugas Lukosius, ACS Appl. Mater. Interfaces 2020, 12, 2, 3188–3197.
- Mindaugas Lukosius, Jarek Marek Dabrowski, Julia Kitzmann, Oksana Fursenko, **Fatima Akhtar**, Marco Lisker, Gunther Lippert, Sebastian Schulze, Yuji Yamamoto, Markus Andreas Schubert, Hans-Micheal Krause, Andre Wolff, Andreas Mai, Thomas Schroeder, Grzegorz Lupina. ACS Appl. Mater. Interfaces 2016, 8, 33786–33793.
- G. Reza Yazdi, **Fatima Akhtar**, Ivan G. Ivanov, Susann Schmidt, Ivan Shtepliuk, Alexei Zakharov, Tihomir Iakimov, Rositsa Yakimova, Applied Surface Science 2019, 486, 239–248.
- R. Lukose, M. Lisker, **F. Akhtar**, M. Fraschke, T. Grabolla, A. Mai, and M. Lukosius, Scientific Reports 2021, volume 11, 13111.

Presentations at conferences

- Investigations of Ni substrates for the growth of graphene, IWAN, 2016.
- Towards graphene synthesis: A comparative study of Nickel/SiO₂/Si annealing in vacuum and hydrogen, DFG, 2017.

- Study the effect of different ambient conditions on the annealing of polycrystalline Nickel/SiO₂/Si and the growth of graphene, ANM, 2018.
- Modification of the 8-inch Ni/SiO₂/Si morphology for graphene growth by chemical vapor deposition, Graphene week 2018.
- Study the interfaces of graphene-covered Ge(001) and Ge(110), Graphene week, 2019.

LITERATURE

1. A. K. Geim and K. S. Novoselov, The rise of graphene, *Nature materials* **6**, 183–191 (2007).
2. K.S. Novoselov, A. K. Geim, S. V. Morozov, D. Jiang, Y. Zhang, S. V. Dubonos, I. V. Grigorieva, A. A. Firsov, Electric field effect in atomically thin carbon films, *Science* **306**, 666–669 (2004).
3. M. P. Levendorf, C. Ruiz-Vargas, S. Garg, J. Park, Transfer-free batch fabrication of single-layer Graphene Transistors, *Nano Lett.* **9**, 4479–4483 (2009).
4. Y.-M. Lin, K. A. Jenkins, A. Valdes-Garcia, J. P. Small, D. B. Farmer, P. Avouris, Operation of graphene transistors at gigahertz frequencies, *Nano Lett.* **9**, 422–426 (2009).
5. K.S. Kim, Y. Zhao, H. Jang, S. Y. Lee, J. M. Kim, K. S. Kim, J-H. Ahn, P. Kim, J-Y. Choi, and B. H. Hong, Large-scale pattern growth of graphene films for stretchable transparent electrodes, *Nature* **457**, 706–710 (2009).
6. K.S. Novoselov, V. I. Falko, L. Colombo, P. R. Gellert, M. G. Schwab, and K. Kim, A roadmap for graphene, *Nature* **490**, 192–200 (2012).
7. Y.-M Lin, A. Valdes-Garcia, S.-J. Han, D. B. Farmer, I. Meric, Y. Sun, Y. Wu, C. Dimitrakopoulos, A. Grill, P. Avouris, K. A. Jenkins, Wafer-scale graphene Integrated circuit, *Science* **332**, 1294–1297 (2011).
8. F. Bonaccorso, Z. Sun, T. Hasan, and A. C. Ferrari, Graphene photonics and optoelectronics, *Nat. Photonics* **4**, 611–622 (2010).

9. F. Schedin, A. K. Geim, S. V. Morozov, E. W. Hill, P. Blake, M. I. Katsnelson, and K. S. Novoselov, Detection of individual gas molecules adsorbed on graphene, *Nat. Mater.* **6**, 652–655 (2007).
10. F. Banhart, J. Kotakoski, and A. V. Krasheninnikov, Structural defects in graphene, *ACS Nano* **5**, 26–41 (2011).
11. Handbook of Carbon, Graphite, Diamonds and Fullerenes by Hugh O. Pierson, 1st Edition, Noyes publications.
12. A. Maffucci, and G. Miano, Electrical properties of graphene for interconnect applications, *Appl. Sci.* **4**, 305–317 (2014).
13. Introduction to Graphene-Based Nanomaterials: From electronic structure to quantum transport by Luis EF Foa Torres, Stephan Roche, Jean-Christophe Charlier, Cambridge university press.
14. A. H. Castro Neto, F. Guinea, N. M. R. Peres, K. S. Novoselov, and A. K. Geim, The electronic properties of graphene, *Rev. Mod. Phys.* **81**, 109–162 (2009).
15. L. P. Biro, P. Nemes-Incze, and P. Lambin, Graphene: nanoscale processing and recent applications, *Nanoscale* **4**, 1824–1839 (2012).
16. J.-C. Charlier, P. C. Eklund J. Zhu, A. C. Ferrari, Electron and phonon properties of graphene: Their relationship with carbon nanotubes, *Topics in Applied Physics*, **111**, 673–709.
17. Nobel Academy, Appendix, some properties of graphene, The Royal Swedish Academy of Sciences (5th October 2010).
18. S. Bharech and R. Kumar, A Review on the Properties and Applications of Graphene, *Journal of Material Science and Mechanical Engineering (JMSME)* **2**, 70–73 (2015).

19. R. R. Nair, P. Blake, A. N. Grigorenko, K.S. Novoselov, T. J. Booth, T. Stauber, N. M. R. Peres, A. K. Geim, Fine structure constant defines visual transparency of Graphene, *Science* **320**, 1308 (2008).
20. K. I. Bolotin, K. J. Sikes, Z. Jiang, M. Klima, G. Fudenberg, J. Hone, P. Kim, H. L. Stormer, Ultrahigh electron mobility in suspended graphene," *Solid State Commun.* **146**, 351–55 (2008). (b) K. I. Bolotin, K. J. Sikes, J. Hone, H. L. Stormer, and P. Kim, Temperature-dependent transport in suspended graphene, *Physical Rev. Lett.* **101**, 096802 (2008).
21. A. C. Ferrari et al., Science and technology roadmap for graphene, related two-dimensional crystals, and hybrid systems, *Nanoscale* **7**, 4598–4810 (2015).
22. R. Munoz and C. Gómez-Aleixandre, C. Review of CVD synthesis of graphene, *Chem. Vap. Depos.* **19**, 297–322 (2013).
23. A. Yakubu, G. D. Sani, Z. Abbas, Graphene synthesis by chemical vapor deposition: A review on growth mechanism and techniques, *IJERT.* **8**, 2019.
24. J. Coraux, A. T. N. Diaye, M. Engler, C. Busse, D. Wall, N. Buckanie, F.-J. M. Zu. Heringdorf, R. V. Gaste, B. Poelsema and T. Michely, Growth of graphene on Ir(111), *New J. Phys.* **11**, 039801 (2009).
25. P. W. Sutter, J.-I. Flege and E. A. Sutter, Epitaxial graphene on ruthenium, *Nature Materials* **7**, 406 (2008).
26. O. Nakagoe, N. Takagi, Y. Matsumoto, Thermal decomposition of acetylene on Pt (1 1) studied by scanning tunneling microscopy, *Surface Science* **514**, 414–419, (2002).
27. L. Zhang, Z. Shi, Y. Wang, R. Yang, D. Shi, and G. Zhang, Catalyst-free growth of nanographene films on various substrates, *Nano Res.* **4**, 315–321 (2011).

28. J. Chen, Y. Guo, L. Jiang, Z. Xu, L. Huang, Y. Xue, D. Geng, B. Wu, W. Hu, G. Yu, Y. Liu, Near-equilibrium chemical vapor deposition of high-quality single-crystal graphene directly on various dielectric substrates, *Adv. Mater.* **26**, 1348–1353 (2014).
29. J. Chen, Y. Wen, Y. Guo, B. Wu, L. Huang, Y. Xue, D. Geng, D. Wang, G. Yu, and Y. Liu, Oxygen-aided synthesis of polycrystalline graphene on silicon dioxide substrates, *J. Am. Chem. Soc.* **133**, 17548 (2011).
30. C. Mattevi, H. Kim, and M. Chhowalla, A review of chemical vapor deposition on copper, *J. Mater. Chem.* **21**, 3324–3334, (2011).
31. X. Li, W. Cai, L. Colombo, and R. S. Ruoff, Evolution of Graphene Growth on Ni and Cu by Carbon Isotope Labeling, *Nano Lett.* **9**, 4268–4272 (2009).
32. H.-J. Shin, S.-M. Yoon, W. M. Choi, S. Park, D. Lee, I. Y. Song, Y. S. Woo, and J.-Y. Choi, Influence of Cu crystallographic orientation on electron transport in graphene, *Appl. Phys. Lett.* **102**, 163102–163102 (2013).
33. (a) B. R. Didar, H. Khosravian, and P. B. Balbuena, Temperature effect on the nucleation of graphene on Cu (111), *RSC Adv.* **8**, 27825–27831 (2018). (b) T. Chaniera, T L. Henrard, From carbon atom to graphene on Cu(111): an ab-initio study, *Eur. Phys. J. B* **88** (2015).
34. C. Jeon, H.-N. Hwang, W.-G. Lee, Y. G. Jung, K. S. Kim, C.-Y. Park, and C.-C. Hwang, Rotated domains in chemical vapor deposition-grown monolayer graphene on Cu (111): an angle-resolved photoemission study, *Nanoscale* **5**, 8210 (2013).
35. P. Y. Huang, C. S. Ruiz-Vargas, A. M. van der Zande, W. S. Whitney, M. P. Levendof, J. W. Kevek, S. Garg, J. S. Alden, C. J. Hustedt, Y. Zhu, J. Park, P. L. McEuen, and D. A.

- Muller, Grains and grain boundaries in single-layer graphene atomic patchwork quilts. *Nature* **469**, 389–392 (2011).
36. Q. Yu, Q. L. A. Jauregui, W. Wu, R. Colby, J. Tian, Z. Su, H. Cao, Z. Liu, D. Pandey, D. Wei, T. F. Chung, P. Peng, N. P. Guisinger, E. A. Stach, J. Bao, S.-Sh. Pei, and Yong P. Chen, Control and characterization of individual grains and grain boundaries in graphene grown by chemical vapor deposition, *Nat. Mater.* **10**, 443–449 (2011).
37. A. W. Tsen, L. Brown, M. P. Levendorf, F. Ghahari, P. Y. Huang, R. W. Havener, C. S. Ruiz-Vargas, D. A. Muller, P. Kim, J. Park, Tailoring electrical transport across grain boundaries in polycrystalline graphene, *Science* **336**, 1143–1146 (2012).
38. Y. Ogawa, K. Komatsu, K. Kawahara, M. Tsuji, K. Tsukagoshi, and H. Ago, Structure and transport properties of the interface between CVD-grown graphene domains, *Nanoscale* **6**, 7288–7294 (2014).
39. G. Bertoni, L. Calmels, A. Altibelli, and V. Serin, First-principles calculation of the electronic structure and EELS spectra at the graphene/Ni (111) interface, *Physical Review B* **71**, 075402 (2004).
40. A. Dahal and M. Batzill, Graphene–nickel interfaces: a review, *Nanoscale* **6**, 2548–2562 (2014).
41. Y. Gamo, A. Nagashima, M. Wakabayashi, M. Terai, and C. Oshima, Atomic structure of monolayer graphite formed on Ni(111), *Surface Science* **374**, 61–64 (1997).
42. J. Lahiri, T. S. Miller, A. J. Ross, L. Adamska, I. I. Oleynik, and M. Batzill, Graphene growth and stability at nickel surfaces. *New J. Phys.*, **13**, 025001 (2011).
43. Y. Zhang, L. Gomez, F. N. Ishikawa, A. Madaria, K. Ryu, C. Wang, A. Badmaev, and C. Zhou, Comparison of graphene growth on single-crystalline and polycrystalline Ni by chemical vapor deposition, *J. Phys. Chem. Lett.* **1**, 3101–3107 (2010).

44. A. Reina, S. Thiele, X. Jia, S. Bhaviripudi, M. S. Dresselhaus, J.A. Schaefer, and J. Kong, Growth of large-area single- and bi-layer graphene by controlled carbon precipitation on polycrystalline Ni surfaces, *Nano Res.* **2**, 509–516 (2009).
45. Q. Yu, J. Lian, S. Siriponglert, H. Li, Y. P. Chen, and S.-S. Pei, Graphene segregated on Ni surfaces and transferred to insulators, *Appl. Phys. Lett.* **93**, 113103 (2008).
46. R. I. Scace and G. A. Slack, Solubility of carbon in silicon and germanium, *J. Chem. Phys.* **30**, 1551 (1959).
47. https://physics.uwo.ca/~lgonchar/courses/p9826/Lecture2_SurfaceStructure.pdf.
48. P. Ponath, A. B. Posadas, and A. A. Demkov, Ge(001) surface cleaning methods for device integration, *Appl. Phys. Rev.* **4**, 021308 (2017).
49. T. Ichikawa, In situ STM observations of ordering behaviors on Ge(1 1 0) surfaces and atomic geometry of the Ge{17 15 1} face, *Surf. Sci.* **560**, 213–225 (2004).
50. C. H. Mullet, S. Chiang, Reconstructions and phase transition of clean Ge(1 1 0) *Surf. Sci.* **621**, 184–190 (2014).
51. J.-H. Lee, E. K. Lee, W.-J. Joo, Y. Jang, B.-S. Kim, J. Y. Lim, S.-H. Choi, S. J. Ahn, J. R. Ahn, M.-H. Park, C.-W. Yang, B. L. Choi, S.-W. Hwang, D. Whang, Wafer-scale growth of single-crystal monolayer graphene on reusable hydrogen-terminated germanium, *Science* **344**, 286–289 (2014).
52. G. Lupina, M. Lukosius, G. Lippert, J. Dabrowski, J. Kitzmann, M. Lisker, P. Kulse, A. Kruger, O. Fursenko, I. Costina, A. Trusch, Y. Yamamoto, A. Wolff, T. Schroeder, and A. Mai, Graphene synthesis and processing on Ge substrates, *ECS Journal of Solid State Science and Technology* **6**, M55-M59 (2017).
53. Handbook of chemical vapor deposition (CVD) principles, technology, and applications by Hugh O. Pierson, Second Edition, Noyes publications.

54. Raman Spectroscopy in Graphene Related Systems by Ado Jorio, Riichiro Saito, Gene Dresselhaus, and Mildred S. Dresselhaus , First Edition, Wiley-VCH.
55. A. C. Ferrari, D. M. Basko, Raman spectroscopy as a versatile tool for studying the properties of graphene, *Nat. Nanotechnol.* **8**, 235–246 (2013).
56. A. C. Ferrari, J. C. Meyer, V. Scardaci, C. Casiraghi, M. Lazzeri, F. Mauri, S. Piscanec, D. Jiang, K. S. Novoselov, S. Roth, A. K. Geim, Raman Spectrum of Graphene and Graphene Layers, *Phys. Rev. Lett.* **97** 187401 (2006).
57. Y. Hao, Y. Wang L. Wang, Z. Ni, Z. Wang, R. Wang, C. K. Koo. Zexiang, S. J. T. L. Thong, Probing layer number and stacking order of few-layer graphene by raman spectroscopy, *small* **6**, 195–200 (2010).
58. R. Beams, L. G. Cancado, and L. Novotny, Raman characterization of defects and dopants in graphene, *J. Phys.: Condens. Matter.* **27**, 083002 (2015).
59. C. Casiraghi, and S. Pisana, Raman fingerprint of charged impurities in graphene, *Appl. Phys. Lett.* **91**, 233108 (2007).
60. T. Yu, Z. Ni, C. Du, Y. You, Y. Wang, and Z. Shen., Raman mapping investigation of graphene on transparent flexible substrate: The strain effect *J. Phys. Chem. C* **112**, 12602 (2008).
61. L. Malard, M.A. Pimenta, G. Dresselhaus, M. S. Dresselhaus, Raman spectroscopy in graphene, *Physics Reports* **473**, 51–87 (2009).
62. Surface analysis methods in material science (springer series in surface science 23) by D. J. O Connor, B.A Sexton, and Roger St.C. Smart, 1st edition, Springer.
63. Surface Analysis: The Principal Techniques by John C. Vickerman, Rod Wilson, Buddy Ratner, David Castner, and Hans Joerg, Second edition, John Wiley & Sons.

64. S. Liu and Y. Wang, A review of the application of Atomic Force Microscopy (AFM) in food science and technology, *Adv Food Nutr Res.* **62**, 201–240 (2011).
65. Encyclopedia of materials characterization: surfaces, interfaces, thin films, by C. Richard Brundle, Charles A. Evans, Jr. Shaun Wilson, Butterworth-Heinemann.
66. https://www.jeol.co.jp/en/applications/pdf/sm/sem_atoz_all.pdf.
67. Elements of X-ray Diffraction by B. D. Cullity, second edition, Reading, Mass.: Addison-Wesley.
68. D. Stojakovic, Electron backscatter diffraction in materials characterization, *Processing and Application of Ceramics* **6**, 1–13 (2012).
69. https://en.wikipedia.org/wiki/Reactive-ion_etching.
70. <https://www.horiba.com/us/en/scientific/products/ellipsometers/ellipsometry-academy/ellipsometry-tutorial/spectroscopic-ellipsometry-principles/>.
71. F. Akhtar, J. Dabrowski, M. Lisker, P. Zaumseil, S. Schulze, A. Jouvray, P. Caban, A. Mai, C. Wenger, M. Lukosius, *Thin Solid Films* **30**, 137565 (2019).
72. (a) S. Thiele, A. Reina, P. Healey, J. Kedzierski, P. Wyatt, P.-L. Hsu, C. Keast, J. Schaefer, J. Kong, Engineering polycrystalline Ni films to improve thickness uniformity of the chemical-vapor-deposition-grown graphene films, *nanotechnology* **21**, 015601 (2010). (b) T. Wagner and D. Müller, Grain growth in magnetron-sputtered nickel films, *Z. Met.* **93**, 401–405 (2002).
73. C. V. Thompson and R. Carel, Stress and grain growth in thin films, *J. Mech. Phys. Solids* **44**, 657–673 (1996).
74. P. B. Barna, and M. Adamik. Fundamental structure forming phenomena of polycrystalline films and the structure zone models, *Thin Solid Films* **317**, 27–33 (1998).

75. (a) L. N. Brewer and J. R. Michael, Risks of “cleaning” electron backscatter diffraction data, *Microsc. Today* **18**, 10–15 (2010). (b) <https://imagej.net/Downloads>.
76. R. A. Oriani. The physical and metallurgical aspects of hydrogen in metals, ICCF4, Fourth International Conference on Cold Fusion, Electric Power Research Institute, Lahaina, Maui, 1993 (3412 Hillview Ave., Palo Alto, CA, Oriani, R.A.).
77. K. J. Kim, Y. J. Yun, S. Ji, J.-H. Lee, D. H. Ha, Formation of (111)-oriented nickel nanocrystals by thermal annealing of nickel thin films, *J. Nanosci. Nanotechnol.* **9**, 4786–4791 (2009).
78. J. Cizek, O. Melikhova, M. Vlcek, F. Lukac, M. Vlach, I. Prochazka, W. Anwand, G. Brauer, A. Mücklich, S. Wagner, H. Uchida, A. Pundt. Hydrogen-induced microstructural changes of Pd films, *Int. J. Hydrog. Energy* **38**, 12115–12125 (2013).
79. (a) A. Reina, X. Jia, J. Ho, D. Nezich, H. Son, V. Bulovic, M. S. Dresselhaus, and J. Kong. Large area, few-layer graphene films on arbitrary substrates by chemical vapor deposition, *Nano Lett.* **9**, 30–35 (2009). (b) S. Garaj, W. Hubbard, and J. A. Golovchenko, Graphene synthesis by ion implantation, *Appl. Phys. Lett.* **97**, 183103 (2010). (c) R. S. Weathrup, B. C. Bayer, R. Blume, C. Ducati, C. Baehtz, R. Schlögl, and S. Hofmann, In situ characterization of alloy catalysts for low temperature graphene growth, *Nano Lett.* **11**, 4154–4160 (2011).
80. J. Kozlova, A. Nilisk, H. Alles, V. Sammelselg. Discontinuity and misorientation of graphene grown on nickel foil: effect of the substrate crystallographic orientation, *Carbon* **94**, 160–173 (2015).
81. J. Sun, J. J. B. Hannon, R. M. Tromp, P. Johari, A. A. Bol, V. B. Shenoy, and K. Pohl. Spatially-resolved structure and electronic properties of graphene on polycrystalline Ni, *ACS Nano* **4**, 7073–7077 (2010).

82. Y. Zhang, T. Gao, S. Xie, B. Dai, L. Fu, Y. Chen, M. Liu, and Z. Liu, Different growth behaviors of ambient pressure chemical vapor deposition graphene on Ni(111) and Ni films: a scanning tunneling microscopy study, *Nano Res.* **5**, 402–411 (2012).
83. G. K. Hemani, W. G. Vandenberghe, B. Brennan, Y. J. Chabal, A. V. Walker, R. M. Wallace, M. Quevedo-Lopez, and M. V. Fischetti, Interfacial graphene growth in the Ni/SiO₂ system using pulsed laser deposition, *Appl. Phys. Lett.* **103**, 134102 (2013).
84. S. Kumara, N. McEvoy, T. Lutz, G. Keeley, N. Whiteside, W. Blau, and G. S. Duesberg, Low temperature graphene growth, *ECS Trans.* **19**, 175–181 (2009).
85. D. Q. McNerny, B. Viswanath, D. Copic, F. R Laye, C. Prohoda, A. C. Brieland-Shoultz, E. S. Polsen, N. T. Dee, V. S. Veerasamy, and A. J. Hart, Direct fabrication of graphene on SiO₂ enabled by thin film stress engineering, *Sci. Rep.* **4**, 5049 (2014).
86. L. Baraton, Z. B. He, C. S. Lee, J.-L. Maurice, C. S. Cojocar, A.-F. Gourgues-Lorenzon, Y. H. Lee, and D. Pribat, Synthesis of few-layered graphene by ion implantation of carbon in nickel thin films, *Nanotechnology* **22**, 085601 (2011).
87. L. Baraton, Z. B. He, C. S. Lee, C. S. Cojocar, M. Chatelet, J.-L. Maurice, Y. H. Lee, and D. Pribat, On the mechanisms of precipitation of graphene on nickel thin films, *EPL* **96**, 46003 (2011).
88. Z. Liahngzhong, P. Chenghuang, XPS studies of oxidation behavior of nickel and thermal stability of the surface oxides, *Acta Metallurgica Sinica (English edition) series B*, **2**, 133–137 (1989).
89. I. H. Son, H. J. Song, S. Kwon, A. Bachmatiuk, S. J. Lee, A. Benayad, J. H. Park, J.-Y. Choi, H. Chang, and M. H. Rummeli, CO₂ enhanced chemical vapor deposition growth of few-layer graphene over NiO_x, *ACS Nano* **8**, 9224–9232 (2014).

90. N. Liu, N. L. Fu, B. Dai, K. Yan, X. Liu, R. Zhao, Y. Zhang, and Z. Liu, Universal segregation growth approach to wafer-size graphene from non-noble metals, *Nano Lett.* **11**, 297–303 (2011).
91. D. Kang, W.-J. Kim, J. A. Lim, and Y.-W. Song, Direct growth and patterning of multilayer graphene onto a targeted substrate without an external carbon source, *ACS Appl. Mater. Interfaces* **4**, 3663–3666 (2012).
92. (a) W. Zhao, S. M. Kozlov, O. Hofert, K. Gotterbarm, M. P. A. Lorenz, F. Vines, C. Papp, A. Gorling, and H.-P. Steinruck, Graphene on Ni(111): coexistence of different surface structures, *J. Phys. Chem. Lett.* **2**, 759–764 (2011). (b) C. Africh, C. Cepek, L. L. Patera, G. Zamborlini, P. Genoni, T. O. Mendes, A. Sala, A. Locatelli, and G. Comelli, Switchable graphene-substrate coupling through formation/dissolution of an intercalated Ni-carbide layer, *Sci. Rep.* **6**, 19734 (2016).
93. A. Delamoreanu, C. Rabot, C. Vallee, A. Zenasni, Wafer-scale catalytic growth of graphene on nickel by solid carbon source, *Carbon* **66**, 48–56 (2014).
94. G. Gutierrez, F. L. Normand, D. Muller, F. Aweke, C. Speisser, F. Antoni, Y. L. Gall, C. S. Lee, C. S. Cojocaru, Multi-layer graphene obtained by high temperature carbon implantation into nickel films, *Carbon* **66**, 1–10 (2014).
95. Z. Peng, Z. Yan, Z. Sun, J. M. Tour, Direct growth of bilayer graphene on SiO₂ substrates by carbon diffusion through nickel, *ACS Nano* **10**, 8241–8247 (2011).
96. Y. Yamamoto, Y. P. Zaumseil, T. Arguirov, M. Kittler, B. Tillack. Low threading dislocation density Ge deposited on Si(001) using RPCVD, *Solid state Electron.* **60**, 2–6 (2011).
97. M. Lukosius, G. Lippert, J. Dabrowski, J. Kitzmann, M. Lisker, P. Kulse, A. Krüger, O. Fursenko, I. Costina, A. Trusch, Y. Yamamoto, A. Wolff, A. Mai, T. Schroeder, G.

- Lupina, Graphene synthesis and processing on Ge substrates. *ECS Trans.* **75(8)**, 533–540 (2016).
98. Y. H. Sun, J. H. Park, S. Kwon, S. Park, M. H. Rummeli, A. Bachmatiuk, H. J. Song, J. Ku, J. W. Choi, J.-m. Choi, S.-G. Doo, and H. Chang, Silicon carbide-free graphene growth on silicon for lithium-ion battery with high volumetric energy density. *Nat. Commun.* **6**, 7393 (2015).
99. M. Lukosius, J. Dabrowski, J. Kitzmann, O. Fursenko, F. Akhtar, M. Lisker, G. Lippert, S. Schulze, Y. Yamamoto, M. A. Schubert, H. M. Krause, A. Wolff, A. Mai, T. Schroeder, and G. Lupina, Metal-free CVD graphene synthesis on 200 mm Ge/Si(001) substrates, *ACS Appl. Mater. Interfaces* **8**, 33786–33793 (2016).
100. I. Pasternak, P. Dabrowski, P. Ciepielewski, V. Kolkovsky, Z. Klusek, J. M. Baranowska, and W. Strupinski, Large-area high quality graphene on Ge(001)/Si(001) substrates, *Nanoscale* **8**, 11242–11247 (2016).
101. C. Neumann, S. Reichardt, P. Venezuela, M. Drogeler, L. Banszerus, M. Schmitz, K. Watanabe, T. Taniguchi, F. Mauri, B. Beschoten, S. V. Rotkin & C. Stampfer, Raman spectroscopy as probe of Nanometer-scale strain variations in graphene, *Nat. Commun.* **6**, 8429 (2015).
102. J. E. Lee, G. Ahn, J. Shim, Y. S. Lee, and S. Ryu, Optical separation of mechanical strain from charge doping in graphene, *Nat. Commun.* **3**, 1024 (2012).
103. J. Dabrowski, G. Lippert, J. Avila, J. Baringhaus, I. Colambo, Yu S. Dedkov, F. Herziger, G. Lupina, J. Maultzsch, T. Schaffus, T. Schroeder, M. Kot, C. Tegenkamp, D. Vignaud, and M.-C. Asensio, Understanding the growth mechanism of graphene on Ge/Si(001) surfaces, *Sci, Rep.* **6**, 31639 (2016).

104. K. M. McElhinny, R. M. Jacobberger, A. J. Zaugg, M. S. Arnold, P. G. Evans, Graphene-induced Ge(001) surface faceting, *Surf. Sci.* **647**, 90–95 (2016).
105. G. Lippert, J. Dabrowski, T. Schroeder, M. A. Schubert, Y. Yamamoto, F. Herziger, J. Maultzsch, J. Baringhaus, C. Tegenkamp, M. C. Asensio, J. Avila, G. Lupina, Graphene grown on Ge(0 0 1) from atomic source, *Carbon* **75**, 104–112 (2014).
106. B. Kiraly, R. M. Jacobberger, A. J. Mannix, G. P. Campbell, M. J. Bedzyk, M. S. Arnold, M. C. Hersam, and N. P. Guisinger, Electronic and mechanical properties of graphene-germanium interfaces by chemical vapor deposition, *Nano Lett.* **15**, 7414–7420 (2015).
107. G. Wang, M. Zhang, Y. Zhu, G. Ding, D. Jiang, Q. Guo, S. Liu, X. Xie, P. K. Chu, Z. Di, and X. Wang, Direct growth of graphene film on germanium substrates. *Sci. Rep.* **3**, 2465 (2013).
108. A. M. Scaparro, V. Miseikis, C. Coletti, A. Notargiacomo, M. Pea, M. De Seta, and L. Di Gaspare, Investigation the CVD Synthesis of Graphene on Ge(100): Toward Layer-by Layer Growth, *ACS Appl. Mater. Interfaces* **8**, 33083–33090 (2016).
109. J. Dai, D. Wang, M. Zhang, T. Niu, A. Li, M. Ye, S. Qiao, G. Ding, X. Xie, Y. Wang, P. K. Chu, Q. Yuan, Z. Di, X. Wang, F. Ding, and B. I. Yakobson, How graphene islands are unidirectionally aligned on Ge(110) surface, *NanoLett.* **16**, 3160–3165 (2016).
110. I. Pasternak, M. Wesolowski, I. Jozwik, M. Lukosius, G. Lupina, P. Dabrowski, J. M. Baranowski, and W. Strupinski, Graphene growth on Ge(100)/Si(100) substrates by CVD method, *Sci. Rep.* **6**, 21773 (2016).
111. M. Lukosius, J. Dabrowski, J. Kitzmann, O. Fursenko, F. Akhtar, M. Lisker, G. Lippert, S. Schulze, Y. Yamamoto, M. A. Schubert, H. M. Krause, A. Wolff, A. Mai, T.

- Schroeder, and G. Lupina, Metal-free CVD graphene synthesis on 200 mm Ge/Si(001) substrates, *ACS Appl. Mater. Interfaces* **8**, 33786–33793 (2016).
112. (a) Jülich Supercomputing Centre, JUWELS: Modular Tier-0/1 Supercomputer at the Jülich Supercomputing Centre, *J. Large Scale Res. Facil.* **5**, A171 (2019). (b) J. Dabrowski, F. Akhtar, M. Lukosius.
113. (a) P. Dabrowski, M. Rogala, I. Pasternak, J. Baranowski, W. Strupinski, M. Kopciuszynski, R. Zdyb, M. Jaloehowski, I. Lutsyk, and Z. Klusek, The study of the Interactions between Graphene and Ge(001)/Si(001). *Nano Res.* **10**, 3648–3661 (2017). (b) F. Akhtar, J. Dabrowski, M. Lisker, Y. Yamamoto, A. Mai, C. Wenger, M. Lukosius, *ACS Appl. Mater. Interfaces* **12**, 3188 (2020). (c) L. D. Gaspare, A. M. Scaparro, M. Fanfoni, L. Fazi, A. Sgarlata, A. Notargiacomo, V. Miseikis, C. Coletti, and M. D. Seta, Early stages of CVD graphene Synthesis on Ge (001) Substrate, *Carbon* **134**, 183–188 (2018).
114. R. M. Jacobberger, M. J. Dodd, M. Zamiri, A. J. Way, M. S. Arnold, and M. G. Lagally, Passivation of Germanium by Graphene for Stable Graphene/Germanium Heterostructure Devices, *ACS Appl. Nano Mater.* **2**, 4313–4322 (2019).
115. (a) K. Prabhakaran and T. Ogino. Oxidation of Ge(100) and Ge(111) Surfaces: An UPS and XPS study. *Surf. Sci.* **325**, 263–271 (1995). (b) D. Bodlaki, H. Yamamoto, D.H. Waldeck, E. Borguet. Ambient stability of chemically passivated germanium interfaces, *Surf. Sci.* **543**, 63–74 (2003).
116. R. R. Delgado, R. M. Jacobberger, S. S. Roy, V. S. Mangu, M. S. Arnold, F. Cavallo, and M. G. Lagally, Passivation of Germanium by Graphene, *ACS Appl. Mater. Interfaces* **9**, 17629–17636 (2017).

117. P. Dabrowski, M. Rogala, I. Pasternak, P. Krukowski, J. M. Baranowski, W. Strupinski, I. Lutsyk, D. A. Kowalczyk, S. Pawlowski, Z. Klusek, Early oxidation stages of germanium substrate in the Graphene/Ge(001) system, *Carbon* **149**, 290–296 (2019).
118. F. Forster, A. Molina-Sanchez, S. Engels, A. Epping, K. Watanabe, T. Taniguchi, L. Wirtz, and C. Stampfer, Dielectric screening of the kohn anomaly of graphene on hexagonal boron nitride, *Phys. Rev. B* **88**, 085419 (2013).
119. L. Banszerus, H. Janssen, M. Otto, A. Epping, T. Taniguchi, K. Watanabe, B. Beschoten, D. Neumaier, and C. Stampfer, Identifying suitable substrates for high-quality graphene-based heterostructures, *2D Mater.* **4**, 025030 (2017).
120. J. Kwak, Y. Jo, S.-D. Park, N. Y. Kim, S.-Y. Kim, H.-J. Shin, Z. Lee, S. Y. Kim, and S.-Y. Kwon, Oxidation behavior of graphene coated copper at intrinsic graphene defects of different origins, *Nat. Commun.* **8**, 1549 (2017).
121. M. Schriver, W. Regan, W. J. Gannett, A. M. Zaniewski, M. F. Crommie, and A. Zettl, Graphene as a long-term metal oxidation barrier: worse than nothing, *ACS Nano* **7**, 5763–5768 (2013).
122. R. Blume, P. R. Kidambi, B. C. Bayer, R. S. Weatherup, Z.-J. Wang, G. Weinberg, M.-G. Willinger, M. Greiner, S. Hofmann, A. Knop-Gericke, and R. Schlögl, The influence of intercalated oxygen on the properties of graphene on polycrystalline Cu under various environmental conditions, *Phys. Chem.* **16**, 25989–26003 (2014).
123. S. S. Roy and M. S. Arnold, Improving graphene diffusion barriers via stacking multiple layers and grain size engineering, *Adv. Funct. Mater.* **23**, 3638 (2013).

124. F. Zhou, Z. Li, G. J. Shenoy, L. Li, and H. Liu, Enhanced room-temperature corrosion of copper in the presence of graphene, *ACS Nano* **7**, 6939–6947 (2013).
125. R. S. Weatherup, L. D’Arsie, A. Cabrero-Vilatela, S. Caneva, R. Blume, J. Robertson, R. Schloegl, and S. Hofmann, Long-term passivation of strongly interacting metals with single layer graphene, *J. Am. Chem. Soc.* **137**, 14358–14366 (2015).
126. Y.-P. Hsieh, M. Hofmann, K.-W. Chang, J. G. Jhu, Y.-Y. Li, K. Y. Chen, C. C. Yang, W.-S. Chang and L.-C. Chen, Complete corrosion inhibition through graphene defect passivation, *ACS Nano* **8**, 443–448 (2014).
127. J. Lei, Y. Hu, Z. Liu, G. J. Cheng, and K. Zhao, Defects mediated corrosion in graphene coating layer, *ACS Appl. Mater. Interfaces* **9**, 11902–11908 (2017).
128. S. Oh, Y. Jung, and J. Kim, Effects of defect density on ultrathin graphene-based metal diffusion barriers, *J. Vac. Sci. Technol. A* **33**, 061510 (2015).
129. D. L. Duong, G. H. Han, S. M. Lee, F. Gunes, E. S. Kim, S. T. Kim, H. Kim, Q. H. Ta, K. P. So, S. J. Yoon, S. J. Chae, Y. W. Jo, M. H. Park, S. H. Chae, S. C. Lim, J. Y. Choi, and Y. H. Lee, Probing graphene grain boundaries with optical microscopy, *Nature* **490**, 235–239 (2012).
130. M. Topsakal, H. Sahin, and S. Ciraci, Graphene coatings: An efficient protection from oxidation, *Phys. Rev. B* **85**, 155445 (2012).
131. O. Leenaerts, B. Partoens, and F. M. Peeters, Graphene: A perfect Nanoballoon, *Appl. Phys. Lett.* **93**, 193107 (2008).
132. J. S. Bunch, S. S. Verbridge, J. S. Alden, A. M. van der Zande, J. M. Parpia, H. G. Craighead, and P. L. McEuen, Impermeable atomic membranes from graphene sheets, *Nano Lett.* **8**, 2458–2462 (2008).

133. B. E. Deal and A. S. Grove, General relationship for the thermal oxidation of silicon, *J. Appl. Phys.* **36**, 3770 (1965).
134. H. Z. Massoud, J. D. Plummer, and E. A. Irene, thermal oxidation of silicon in dry oxygen growth-Rate enhancement in the thin regime, *J. Electrochem. Soc.* **132**, 2685 (1985).